# The origin of the precession-scale cycles in the ~2.45 Ga Joffre Member, Brockman iron formation, Western Australia

**S.B.Hoogendoorn**

Department of Earth Sciences, University of Utrecht, Utrecht 3584 CS, Netherlands.
Contact details of corresponding author. Tel: + 31 06 397 824 30. E-mail:
s.b.hoogendoorn@students.uu.nl

---

Master thesis in Earth Sciences
Sander Hoogendoorn
First supervisor: prof. dr. Paul Mason, Utrecht University
Second supervisor: drs. Margriet Lantink, Utrecht University

# Content

## Abstract

It was recently shown that astronomical climate forcing through quasi-periodic variations of the eccentricity of Earth's orbit played a dominant role in the deposition of Neoarchean and Paleoproterozoic banded iron formations (BIFs). The presence of eccentricity points at the climatic precession cycle as main astronomical driver. Therefore, it is crucial to study geochemical alternations on the precession scale in order to understand the climatic and depositional processes. Here we investigated regular precession-scale variations previously described as Knox cyclothems from two selected drill-core intervals of the ~2.5 Ga Joffre Member BIF (Brockman Iron Fm, NW Australia) by using stable isotope analyses of the organic matter and bulk carbonate content along with detailed mineralogical facies descriptions and high-resolution XRF analyses. Our results revealed systematic variations of the weight percentages of the carbonate and organic carbon and the stable isotope signatures of the carbonates and organic carbon over the Knox cyclothem. The carbonate facies are characterized by a higher weight percentage of organic carbon and carbonate and a heavier stable isotope signature with respect to the oxide and chert facies. We interpreted these results as evidence for original fluctuations in the organic matter during the deposition of BIF. These fluctuations directly controlled the intensity of subsequent diagenetic sedimentary reworking via dissimilatory iron reduction. In the presence of abundant Fe(III)-oxyhydroxides, organic matter was near quantitatively oxidized and partly incorporated into siderite. In the absence of abundant Fe(III)-oxyhydroxides, DIR quantitatively reduced the Fe(III), which triggered the precipitation of a large amount of carbonates. The fluctuations of the organic carbon in the BIF sediment were presumably regulated through changes in bioproductivity in the water column, which varied systematically through the episodic input of terrestrial material and associated bio-limiting nutrients. The input of terrestrial material into the oceans was on its turn regulated by a climate-sensitive (monsoonal) system that operated on the precession scale. Therefore, we have demonstrated that climate directly influenced BIF deposition. This reinforces the idea of BIFs as archives for climate variability on the early Earth.


***Keywords:*** *Banded Iron Formation, dissimilatory iron reduction, precession cyclicity, Joffre Member*

# 1 Introduction

Banded iron formations (BIFs) are silica (40-60% $SiO_2$) and iron rich (15-40% Fe) sedimentary rocks that were deposited in the Precambrian oceans (Bekker et al., 2014; Klein et al., 2005; Konhauser et al., 2017). The origin of the banding in BIFs has long been controversial, although astronomical climate forcing recently regained an interest as dominant mechanism behind BIF deposition after long-period eccentricity cyclicity was recognized in the weathering profile of the 2.48 Ga Kuruman Iron Formation in South Africa (Lantink et al., 2019; Schuurmans et al., 2019 – MSc thesis). These findings were complemented by the discovery of eccentricity cyclicity in the carbonate isotope record of the 2.48 Ga Dales Gorge Iron Formation in Western Australia (Vaz, 2020 – MSc thesis). However, eccentricity itself has a negligible effect on insolation but acts as an amplitude modulator for the climatic precession cycle. Therefore, alternations on the precession-scale are expected to be present in BIF. Studying these alterations is critical for obtaining new information on the climatic and depositional processes associated with astronomical forcing. These short-period precession-cycles (i.e. the Knox cyclothem) were recently recognized in the Joffre Gorge of the Joffre Member from Western Australia (Lantink et al., 2020a – in prep) and were further investigated through high-resolution XRF core scanning (Lantink et al., 2020b – in prep). The precession-scale fluctuations of some redox-sensitive elements (e.g. S and Fe) in the Joffre member were investigated with reactive transport modelling, which hinted at the importance of organic carbon as electron donor during early diagenetic redox cycling in the BIF precursor sediment. Specifically, an increase of initial organic carbon along the Knox cyclothem would coincide with an increase in the intensity of diagenetic reworking of the BIF sediment (Lantink et al., 2020b – in prep). However, direct evidence that supports this interpretation is still missing and it is not clear why the organic carbon in the BIF precursor sediment would vary in the first place. Accordingly, the purpose of this study is of twofold: Firstly, can we use geochemical analyses and petrographic observations to investigate if and why the organic carbon concentration varied on the precession-scale in the BIF precursor sediment and how this influenced subsequent diagenetic redox cycling. And secondly, can we combine these potential fluctuations of organic carbon with other redox-sensitive elements in a conceptual model that aims to explain the link between BIF deposition and climate.

To do this, we selected two drill-core intervals from the Joffre Member BIF of the Brockman formation, Western Australia. We chose these core intervals for the rhythmic reoccurrence of a ~5-15 cm Precession-scale succession of mineralogical distinct bands similar to those described in (Lantink et al., 2020 – in prep). The difference between the intervals was that one comprised a *classic* iron-rich section of the Joffre Member, whereas the other covered a *shaly* carbonate-rich section. We first investigated the intervals with optical microscopy to specify dominant mineralogical and textural features that were related to the diagenetic and/or metamorphic reworking of the sediment. This was succeeded by high-resolution analyses of the Wt% $C_{org}$, $\delta^{13}C_{org}$, Wt% N, $\delta^{15}N_{total}$, $\delta^{13}C_{carb}$, $^{18}O_{carb}$ and Wt% Carbonate along the core length of both intervals. These electron donors and/or redox-sensitive geochemical proxies are typically used in modern environments to constrain early diagenetic remineralization of organic carbon (Hoof et al., 1993; Reichart et al., 1997; Reichart et al., 1998), which makes them useful in mass-balancing to recalculate the pre-diagenetic Wt% $C_{org}$ in the BIF sediment. Finally, we combined our results with ICP-OES data and high-resolution XRF data of the Joffre member (provided by Lantink et al., 2020b – in prep) as baseline for a renewed BIF depositional model. This study will therefore build on the earlier work of (Lantink et al., 2019) to re-evaluate the link between climate and precession-scale cyclicity in BIFs.

# 2 Background

## 2.1 What are Iron Formations?

Banded iron formations (BIFs) provide an unique insight into the dynamics of the Early Earth and as such have had a central role in constraining the redox-state of the Archean and Paleoproterozoic oceans (Konhauser et al., 2017), developing our understanding on the Precambrian biosphere (Bryce et al., 2018), and expanding our knowledge on the oxygenation of the early atmosphere (Sessions et al., 2009). BIFs are named after their conspicuous centimeter-scale banding, which is traditionally referred to as *mesobanding*. In contrast, meter-scale bands are called *macrobanding* and smaller micrometer-scale to nanometer-scale bands are termed *microbands* (Trendall, 1970). The stratigraphic settings in which BIF deposition took place was highly variable but must have been below the wave base because of the preservation of laterally extensive banding (Konhauser et al., 2017). Furthermore, BIFs are characterized by negative or near zero εNd values (-1 to +4), a low $Al_2O_3$ content (<1%), and minor amounts of trace elements such as Ti, Zr, Th, Hf, and Sc (<20 ppm). This implies that minor detrital input affected BIFs (Jacobsen and Pimentel-Klose, 1988; Bekker et al., 2014). The occurrence of negative $\delta^{30}$Si isotope signatures in BIF chert further suggest that some of the BIF precursor minerals precipitated directly from the ocean water column (Heck et al., 2011; Steinhoefel et al., 2009; Steinhoefel et al., 2010).

The banding in BIFs is composed of fine-grained ($\mu$m's) minerals, which typically show a distinctive macro-, meso-, and micro-scale layering of chert, carbonate, iron oxide, and silicate mineral facies (James, 1954). The chert mineral facies are characterized by microgranular quartz, whereas the carbonate mineral facies are defined by predominantly siderite and ankerite with lesser amounts of dolomite and calcite. The iron oxide facies consist of magnetite ($Fe_3O_4$) and hematite ($Fe_2O_3$), both of which are occasionally associated with goethite ($FeO[OH]$) and limonite ($FeO[OH] \cdot nH_2O$). Finally, the silicate mineral facies contain the largest mineral variety, which is a direct consequence of diagenesis and metamorphism (Miyano & Beukes, 1984). BIFs that were exposed to low-grade prehnite-pumpellyite to greenschist facies metamorphism are characterized by stilpnomelane, minnesotaite, greenalite, riebeckite, Fe-chlorite (e.g. ripidolite, chamosite), and ferrianite. In contrast, BIFs exposed to amphibolite facies metamorphism are dominated by a variety of Fe-rich amphiboles (e.g. Cummingstone & actinolite), pyroxene, garnet, and fayalite (Konhauser et al., 2017). Organic matter is a minor constituent of BIFs (<0.5 wt%) and occurs as a kerogen pigmentation on carbonates (Beukes et al., 1990).

BIFs can be subdivided into two distinct groups, although it may be more practical to think of these groups as end-members in a continuous spectrum (Bekker et al., 2014). The Algoma-type BIFs are relatively thin (0.1–10 m) and laterally restricted to a few kilometers. They are incorporated in Archean greenstone belts and closely associated with submarine volcanic rocks. Examples of the Algoma-types BIFs are found in the North China craton in China (Li et al., 2015), the Abitibi Greenstone belt in Canada (Taner & Chemam, 2015), and the Isua Greenstone belt in Greenland (Whitehouse & Fedo, 2007).

The other end of the spectrum covers the Superior type BIFs, which are thicker (1 – 1000 m) and laterally more extensive (over 100 km) when compared to the Algoma-type BIFs. Superior-type BIFs are not necessarily associated with abundant volcanic rocks, although some may be interlayered with volcaniclastic material (e.g. lutiles in the Hamersley province) (Haugaard et al., 2016; Trendall et al., 2004). Superior-type BIFs can be found near the margins of Archean and Proterozoic shields, where they typically make up a significant part of the folded and metamorphosed strata. This implies that they formed in clastic starved basins bordering ancient

continents (Cook, 1976). Examples of the Superior-type BIFs are well-represented in the Transvaal Supergroup of South Africa (Steinhoefel et al., 2010), the Minas group of Brasil (Rosière & Chemale Jr, 2017), the Animikie group of Canada (Lepot et al., 2017a), and the Hamersley group of Western Australia (Haugaard et al., 2016).

## 2.2 How did iron formations form?

Most studies that try to decipher how BIFs formed propose the oxidation of aqueous Fe(II) to the less-soluble Fe(III) as a baseline (Dauphas et al., 2004; Wu et al., 2011). Such insoluble Fe(III) would continue to hydrate to a Si-Fe gel and/or to microcrystalline ferrihydrite, both of which could readily scavenge REEY and P from the water column during particle settling. This effectively transferred these elements towards the sediment pile (Li et al., 2013; Wu et al., 2012). After this initial stage of particle settling, the Fe-Si gel/ferrihydrite dehydrated in a series of diagenetic and metamorphic reactions, which altered the original mineralogy and modified the primary isotopes signatures. Evidence for such reactions can for example be seen in the homogenization of oxygen isotope for many secondary BIF minerals (e.g. magnetite and chert) (Konhauser et al., 2017). So according to the classical BIF deposition model, the secondary nature of many BIF minerals does not advocate equilibrium conditions with seawater.

Three different mechanisms have been proposed to explain the oxidation of Fe(II) in the Archean and Proterozoic oceans. These mechanisms are: (1) abiological photo-oxidation through the absorption of radiation by ferrous iron in in the 200-400 nanometer wavelength spectrum (Cairns-Smith, 1978). However, it was recently shown that the rate of abiological photo-oxidation was several orders of magnitude too low to explain the estimated the deposition of Superior-type BIFs (Konhauser et al., 2007). A secondary pathway (2) that could have generated a considerable amount Fe(III) is the indirect biological oxidation of Fe(II) by free oxygen, which could have been present above a redoxcline near the ocean surface as a waste product of cyanobacteria (Cloud, 1965). The ability of Fe(II) to act as an electron donor was likely important, since high levels of Fe(II) were likely toxic to cyanobacteria (Konhauser et al., 2017). Finally, a third oxidation pathway (3) that could have been utilized is the direct biological oxidation of ferrous iron in the Archean and Paleoproterozoic oceans. This direct oxidization could have been achieved by anoxygenic photoferrotrophy, a metabolic pathway in which Fe(II) directly acts as an electron donor for carbon fixation (Nisbet & Fowler, 1999; Widdel et al., 1993). The waste product of this metabolic pathway would not be oxygen, but a highly amorphous and hydrous Fe(III) phase that would sink to the sediment pile.

So according to the conventional model, iron oxidation was an essential mechanism for incorporating iron into BIFs. Therefore, it makes sense to expect a dominance of Fe(III) minerals in BIFs. However, this does not seem to be the case. BIFs also contain ferrous iron minerals such as siderite and mixed valence minerals like magnetite. Taken together, this results in an average valence state of $Fe^{+2.4}$, which means that 60% of all the iron in BIF minerals is ferrous (Klein et al., 1992). There are several ways to explain this ambiguity. Firstly, the Fe(III) flux may have been accompanied by a flux of Fe(II)-minerals and mixed valence minerals that co-precipitated from the water column. This would mean that the pre-diagenetic sediment already had an average valence state of $Fe^{+2.4}$ to begin with. The recognition of nano-crystalline greenalite $[(Fe^{2+}, Fe^{3+})_{2-3}Si_2O_5OH_4]$ dispersed through chert mesobands in BIF and thermodynamic modelling of greenalite precipitation support this idea (Tosca et al., 2019; Rasmussen et al., 2014; Stefurak et al., 2015; Tosca et al., 2016). Alternatively, the precursor minerals of stilpnomelane (i.e. Fe-rich clays and/or ash particles) could have interacted with Fe(II) in the water column,

thereby facilitating a Fe(II) flux towards the sediment, which is supported by the petrographic recognition of stilpnomelane as an *early* BIF mineral (Konhauser et al., 2017). Finally, siderite ($FeCO_3$) with negative $\delta^{13}C_{carb}$ signatures (> -5‰) could have precipitated directly from an isotopically stratified ocean, thereby facilitating a Fe(II) flux toward the sediment (Kaufman et al., 1990). This is supported by direct siderite precipitation from a stratified water column in modern anoxic environments (Koeksoy et al., 2016; Ozawa et al., 2017; Kuntz et al., 2015) and REY patterns of siderite in BIFs that mimic the REY patterns of seawater (Oonk et al., 2017).

Another way to explain the average BIF redox state of $Fe^{+2.4}$ is through the reduction of Fe(III) minerals during diagenesis and/or subsequent metamorphism. The released Fe(II) produced during these reactions could either have generated local supersaturation in the pore waters regarding Fe(II) minerals, hence explaining the precipitation of siderite, or the generated Fe(II) could have interacted with hematite to form mixed valence minerals, hence explaining the formation of magnetite and Fe-silicates (e.g. stilpnomelane). There are two important pathways that could explain the Fe(III) reduction in the sediment. Firstly, abiological processes such as metamorphism could have reduced Fe(III) species at elevated temperatures, an idea supported by micro-scale tracings of Fe and Si isotopes and in-situ oxygen isotopes (Steinhoefel et al., 2009; Li et al., 2013a). Secondly, biogenic processes could have reduced the Fe(III) during early diagenesis, with the most noteworthy candidate being dissimilatory iron reduction (DIR), a metabolic pathway that reduces iron at the expense of organic carbon. There is convincing but indirect evidence that DIR occurred during diagenesis. For example, the low carbon content (<0.1 Wt%) and the occurrence of highly negative $\delta^{13}C_{carb}$ values (> -10‰) in BIF suggests that DIR was an important process during the diagenetic reworking of the original BIF sediment (Craddock and Dauphas, 2011; Percak-Dennett et al., 2011; Zhang et al., 2001). The interpretation of DIR is further supported by combined analyses of $\delta^{13}C_{carb}$, $\delta^{18}O_{carb}$, and $\delta^{56}Fe_{carb}$ isotopes (Heimann et al., 2010; Johnson et al., 2008) and the disequilibrium of BIF carbonates and Archean seawater in terms of initial $^{87}Sr/^{86}Sr$ ratios, the latter which supports an interpretation of Sr exchange between minerals during sedimentary reworking (Johnson et al., 2013). Finally, the metabolic pathway of DIR has been demonstrated to be of major importance for the formation of both siderite and magnetite during diagenetic experiments (Halama et al., 2016; Reddy et al., 2016; Posth et al., 2013; Schad et al., 2019). Some workers even propose a model that combines biogenic and abiogenic Fe(III) reduction processes, in which case nano-sized magnetite formed through early microbial activity, after which diagenetic and metamorphic reactions resulted in a further abiotic magnetite growth (Li et al., 2013b).

## 2.3 Banding in BIFs

The rhythmic reoccurrence of the banding of the Dales Gorge Member in the Hamersley province of Western Australia was first recognized by (Trendall, 1970a), who observed that the cyclicity in the banding occurred on four different scales, which are in descending order: the *macrobanding*, the *Knox/Calamina cyclothem*, the *mesobanding*, and the *microbanding*. Note that the Knox and Calamina cyclothems are an intermediate between macrobanding and mesobanding and occur on a 5–15 cm scale. The microbanding showed a regular spacing, which in modern rocks is restricted to diurnal and yearly deposition cycles. Therefore, (Trendall, 1970a) interpreted the microbands as evidence for annual seasonal variations in the basin chemistry. This interpretation was later supported by detailed petrological work (Li, Y., 2014). Interestingly, (Trendall, 1972a) counted the internal microbands within chert mesobands and argued for a ~23.3-year cyclicity in (some) of the chert mesobands of the Dales Gorge member. He tentatively suggested that this ~23.3-year cycle was related to

a double sunspot cyclicity (i.e. the Hale cycle). Therefore, it was (Trendall, 1972a) who was the first to propose that an astronomical forcing influenced BIF deposition. A slightly different interpretation was proposed by (Zahnle and Walker, 1986), who argued that the 23.3-year cycle reflected the precession of the lunar nodes, in which case the deposition of the mesobands was regulated by tidal forcing. Finally, in his presidential letter to the Geological survey of Australia (Trendall, 1972b) took his astronomical forcing hypothesis a step further by speculating that the macrobanding and the Knox/Calamina cyclothem were related to Milankovitch cyclicity. This hypothesis was recently re-evaluated by (Lantink et al., 2019), who argued that the regularity and lateral traceability of macrobands in the Kuruman BIF in South Africa were indeed compatible with Milankovitch cyclicity. To further substantiate this idea, zircons from tuff-layers of the Kuruman formation in South Africa were dated by chemical-abrasion isotope-dilution thermal ionization mass spectrometry (CA-ID-TIMS) (Lantink et al., 2019). Importantly, the CA-ID-TIMS provides much more precise zircon ages ($2\sigma < 0.1\%$) compared to traditional methods such as secondary ion mass spectrometry ($2\sigma < 1$-$2\%$) and laser ablation-inductively coupled plasma mass spectrometry ($2\sigma < 2\%$) (Schaltegger et al., 2015). Therefore, the CA-ID-TIMS measurements provided the necessary resolution to test if the Milankovitch cyclicity was indeed present in BIFs. With the use of spectral analyses Lantink et al., (2019) confirmed the existence of meter-scale eccentricity cycles (1.4-1.6 Myr and 405 Kyr) in the weathering pattern of the Kuruman formation. Additional spectral analyses were carried out on the carbonate isotope record of the Kuruman BIF in South Africa (Schuurmans et al., 2019 – MCs project), the REE record of the Dales Gorge Member in Western Australia (Haddouzi et al., 2019 – MCs project) and the carbonate isotope record of the Dales Gorge Member in Western Australia (Vaz et al., 2019 – MCs project), all of which showed evidence for eccentricity cyclicity. This reinforces the idea that eccentricity cyclicity is a common feature in superior-type BIFs. However, eccentricity itself has a negligible effect on insolation and operates mainly as an amplitude modulator of the climatic precession cycle, the latter which directly regulates changes in seasonal contrast. The dominance of eccentricity cyclicity in the Kuruman BIF and the Dales Gorge BIF thus points at climatic precession as main astronomical driver and furthers suggests that precession-scale variations should be visible in the BIF stratigraphy. Indeed, such cycles (~5-15 cm) were recently identified in the high-resolution XRF record of the Joffre BIF in Western Australia (Lantink et al., 2020 – in prep) and now provide the opportunity to directly study the climatic and depositional response to the Milankovitch forcing, making this an especially relevant area of interesting with respect to the origin of the banding in BIFs.

Another explanation for the origin of the mesobands and macrobands was proposed by (Krapež et al., 2003), who based their interpretation on petrographic textures and sedimentary observations. They proposed that the Fe-rich mesobands and macrobands were generated by bottom currents and/or gravity-driven turbidity currents. These currents could have transported the precursor minerals of BIF — which they argued was dominated by Fe-rich clays— from their original deposition site and redeposited them in the deeper parts of a basin. In periods typified by low turbidity activity, silicification of the Fe-rich mud could have resulted in the formation of chert hardgrounds, hence explaining the alternation between Si-rich and Fe-rich bands (Rasmussen et al., 2013). Importantly, the cyclicity within the turbidity current deposits was explained as an interaction between sea-level variations, changes in the tectonic setting of the basin, and sea-floor magmatism. The changes in sea-level could also have been regulated by Milankovitch cycles (Pickard et al., 2004), albeit in a different way than originally proposed by (Trendall, 1970b). Importantly, if the banding of BIF resulted from the redeposition of BIF precursor sediments, it argues against an onsite chemical precipitation of BIF precursor minerals. This is in contrast with the work of (Konhauser et al., 2008), who argued that changes in ocean temperature resulted in the direct deposition of iron-rich and silica-rich bands; in warm periods, microbial

activity would increase, resulting in more substantial Fe(II) oxidation and an increased flux of ferric iron and organic material to the sediment pile, whereas cold periods would be characterized by a decline in microbial activity and a decrease in the flux of ferric iron and organic material towards the sediment pile. Consequently, silica deposition would take over, resulting in the formation of chert layers. This model was recently backed up by experimental work, suggesting that biological activity and/or climate could have had a direct influence on the BIF banding (Schad et al., 2019). It was also proposed that changes in the upwelling of iron could have influenced the cyclicity of the micro banding in BIFs (Wang et al., 2009). In this scenario, no external forcing was needed, and the layering would result from naturally occurring oscillations in the mixing oxygen-rich surface water and oxygen-poor and iron-rich hydrothermal waters. A hydrothermal controlled BIF cyclicity was supported by micro-scale fluctuations of $\delta^{30}Si$ and $\delta^{56}Fe$ isotope signatures (Steinhoefel et al., 2009). Within this model, Fe-rich microbands would correspond to periods of intensive ferrous iron oxidation and limited ferric iron reduction in the sediment pile, potentially caused by a (relatively) reduced flux of organic carbon towards the sediment pile, whereas Si-rich microbands would correspond to periods of less intensive ferrous iron oxidation and a larger flux of organic carbon to the sediment. The latter would quantitatively reduce the ferric iron, resulting in a dominance of Fe(II)-silicates and siderite. Another abiogenic origin for of the banding in BIF was proposed by (Egglseder et al., 2018), who argued that particle mobilization through dissolution-precipitation creep could result in an accumulation of liberated particles in microbands, thereby obscuring primary lamination and destroying original sedimentary textures. The mobilization of particles would be facilitated by metamorphism and metasomatism during a late stage deformation event in the Hamersley basin, suggesting that the banding in BIFs are metamorphic relicts unrelated to hydrothermal fluctuations and/or external forcing. However, it should be noted that dissolution-precipitation creep could simply have emphasized pre-existing textures as well, in which case particle mobilization could be compatible with other BIF deposition models (Egglseder et al., 2018).

# 3 Geological setting

## 3.1 The Hamersley Basin

The Joffre member is part of the ~100.000 km wide Hamersley basin, a late Archean to early Proterozoic terrane located in Western Australia, a few hundred kilometres north of Perth. The basin is underlain by an older granite-greenstone basement which is called the Pilbara block (Trendall, 1983). The sediments and volcanic rocks that make up the stratigraphy of the Hamersley basin are part of the Mount Bruce Supergroup, which can be further subdivided into three subgroups: the Fortescue Group, the Hamersley group, and the Turee Creek Group (Fig 1). The Fortescue group is the stratigraphically lowest unit of the Mount Bruce Supergroup and unconformably overlies the granite basement (Fig 2). The most common lithologies are mafic lavas that are interstratified with felsic and mafic volcaniclastics (Arndt et al., 1991). The Fortescue group is conformably overlain by the Hamersley group (Fig 2), which is about ~2.5 km thick and contains a series of intrusive rocks, BIFs, shales, and dolomites. The Hamersley group itself can be subdivided into several subgroups. It starts with the ~200 m thick Marra Mamba Iron Formation, which contains intervals of both BIF and shale. The stratigraphically higher Wittenoom formation is much thicker (~500 m) and consists of predominantly shales and dolomites. The Wittenoom formation is conformably overlain by the Mount Sylvia BIF and the Mount McRae Shale, both of which are relatively thin (<100 m) shale member with respect to the other subgroups. On top of this is the ~620 m thick Brockman formation, which contains several of the largest and best studied BIFs in the world, including the approximately ~370 m thick Joffre member and the ~140 m thick Dales Gorge member. The Brockman formation is stratigraphically overlain the ~600 m thick Weeli Wolli Formation, the ~600 m thick Woongarra Rhyolite, and finally the ~200 m thick Boolgeeda Iron formation (Trendall, 2002). The Turee Creek Group conformably overlies the Hamersley group and stratigraphically composes the youngest unit of the Mount Bruce supergroup (Fig 2). It varies largely in thickness (median of ~3.9 km) and crops out along the southern margin of the Hamersley basin. The Turee Creek group is characterized by a dominance of epiclastic sediments (Martin et al., 1998).

## 3.2 Metamorphism

The Hamersley basin experienced several stages of deformation, although a penetrative schistosity is generally lacking in the rocks. There is some evidence for local folding and refolding, which suggests that the Hamersley province endured at least two separate deformation events. These deformation events were possibly related to the Glenburgh orogeny (~2000-1960 Ma) and/or the Capricorn orogeny (~1830-1780 Ma) (Smith et al., 1982). Furthermore, there is a metamorphic gradient present in the Hamersley basin; the northern part of the basin was exposed to prehnite-pumpellyite facies metamorphism (~210 degrees Celcius and 2kbar), whereas the southern part experienced higher greenschist facies metamorphism (~335 degrees Celcius and 3.2 kbar) (Trendall et al., 2004). Regional metasomatism and/or meteoric fluid circulation were likely constricted to the late Glenburgh/Capricorn orogeny and could have been enhanced by local structures (e.g. folds and faults). Importantly, these fluids could have leached metals from the Fortescue group and transported them along local structures into the overlying Hamersley group, explaining why some parts of the Brockman BIFs upgraded to the iron ore deposits that now supply a large part of the iron-ore in the world (Powell et al., 1999).

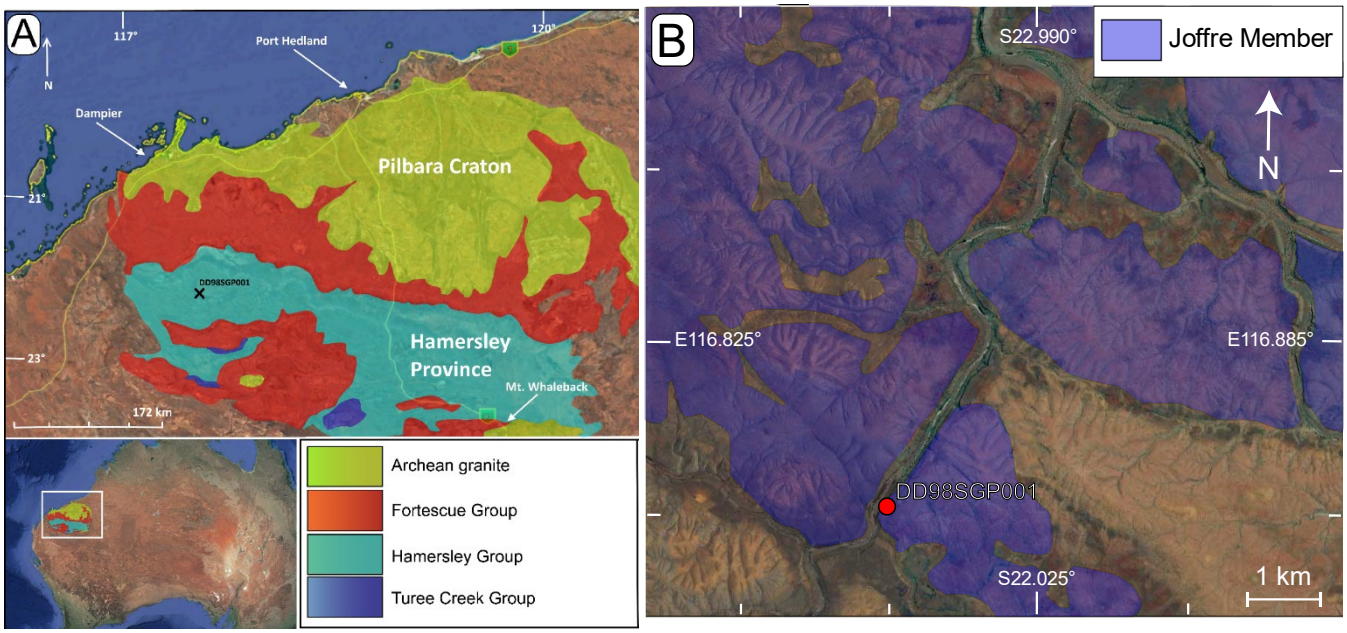


***Fig 1 – A)*** *The location of the Hamersley Basin in Western Australia. Included are the sub-units that make up the Mount Bruce Supergroup, which are in stratigraphically correct order: the Fortescue Group, the Hamersley Group, and the Turee Creek Group. The Mount Bruce Supergroup is underlain by an Archean granite-greenstone belt that crops out mostly north to the Hamersley basin. The location of the drill-core DD98SGP001 (Diamond Drill core 1998 Silver Grass Peak #001) is indicated with a black cross in the north-western part of the Hamersley Group. Figure after (Trendall, 2002).*

***B)*** *A more detailed overview of the location of drill-core DD98SGP001 in the Silver Grass Peak area of the Hamersley Group. The Joffre Member is indicated in blue and crops out locally depending on the regional geomorphology. The drill-core is 450 m long and was drilled at a small angle to the north to capture the dip of the strata. The drill-core also contains the full succession of the Whaleback Shale Member and part of the Dales Gorge Meber. Figure after (Gill, 1999).*

### 3.3 The Brockman Group

The Brockman group itself can be subdivided into four members (Fig 2). Its base is defined by the well-studied Dales Gorge Member, which grades into the Whaleback Shale Member. This is stratigraphically overlain by the ~370 m thick Joffre Member, which finally grades into the Yandicoogina Shale Member. There are two main difference between the shale members and the BIF members: 1) the shale members are on average thinner than the BIF member, and 2) the shale members are dominated by phyllosilicates and carbonates instead of iron-oxides and chert (Trendall et al., 2004). The geological setting of the Brockman group could have been a continental platform and/or passive margin that experienced minimal tectonic activity. The notable lack of terrigenous input, the absence of shorelines, and the occurrence of turbidites, all rule out a shallow marine environment (Morris & Horwitz, 1983). In contrast, a deep marine environment is not compatible with the substantial amounts of carbonate found in the Brockman group (Simonson et al., 1993). Furthermore, it was unlikely that the Brockman group was deposited within an intracratonic basin, since modern analogues show clear evidence for clastic input from rivers and sandstorms (Morris & Horwitz, 1983). This view is supported by positive εNd (1 +/- 0.5) isotopes in BIFs, which were interpreted as a lack of terrestrial input and hence a dominant hydrothermal imprint on the Brockman group, which consequently requires an open marine system (Alibert & McCulloch, 1993; Li et al., 2015). Thin horizons of volcaniclastic material found in the Brockman group were assumed to be of a pyroclastic nature, implying that the Brockman group was spatially and temporarily

related to volcanism. However, the volcanic input was minimal, which taken together with the extensive size of the Brockman BIFs implies that they were of a Superior-type (Haugaard et al., 2016).

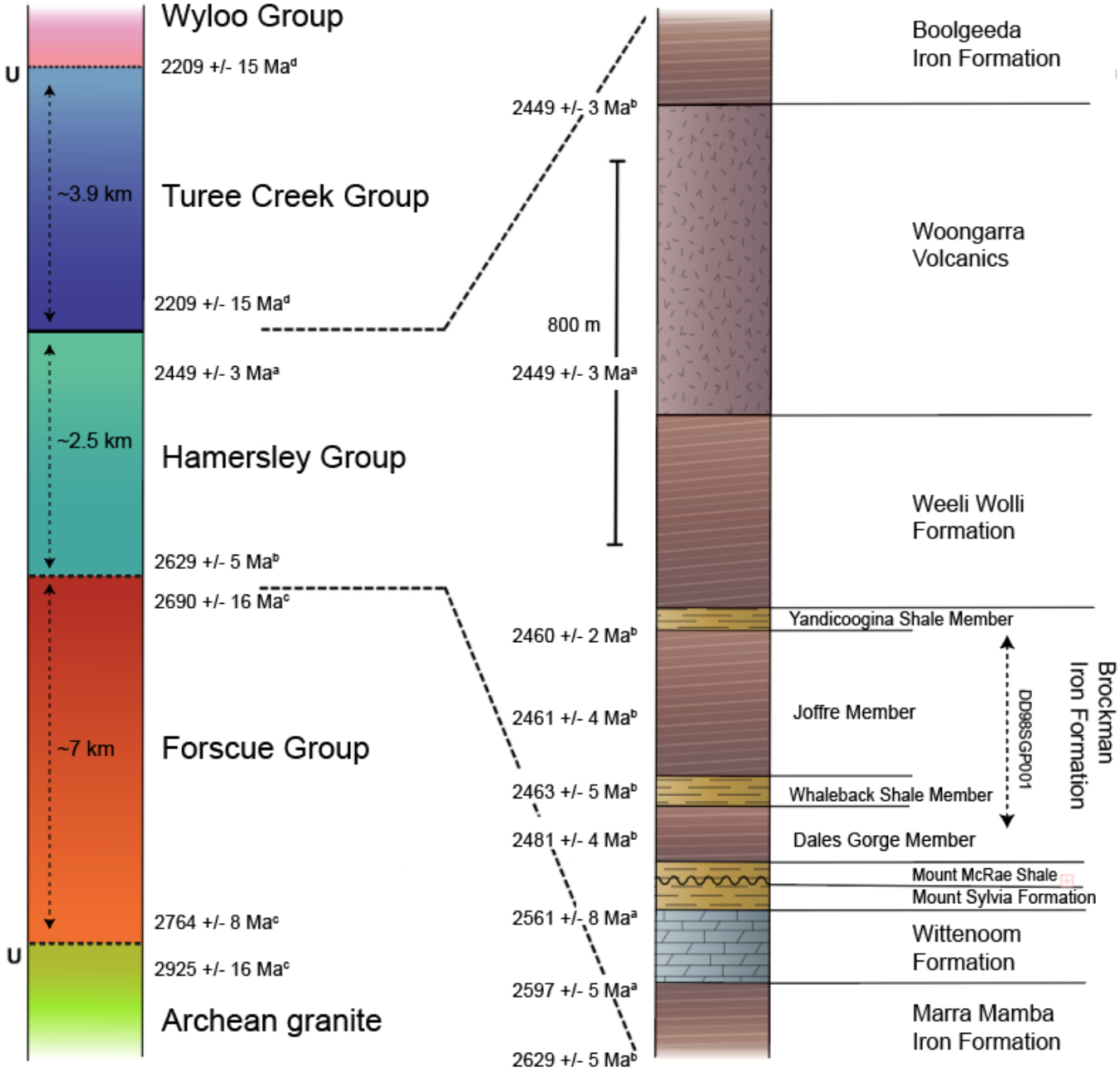


***Fig 2 – Left side:*** *the stratigraphic column of the Mount Bruce Supergroup, which unconformably overlies the Archean granite-greenstone basement and is unconformably overlain by the Wyloo Group (unconformities are indicated by the U on the left side of the column).* ***Right side:*** *the stratigraphic column of the Hamersley Group, with a specific focus on the Brockman Iron Formations. The stratigraphic length that is covered by drill-core DD98SGP001 is indicated with the double-headed arrow. [a]geochronological data provided by (Lindsay & Brasier, 2002). [b]geochronological data provided by (Trendall, 2004). [c]geochrnological data provided by (Arndt et al., 1991). [d]geochronological data provided by (Van Kranendonk et al., 2015).*

### 3.4 The Joffre Member

The Joffre Member and the Dales Gorge Member are similar in terms of their mesobanding and microbanding. However, the regularity of the macrobanding differs substantially between these BIFs. This is mainly in the less pronounced shale intervals from the Joffre member as opposed to the Dales Gorge Member, the latter of which contains 17 BIF and 16 shale bands. Attempts to subdivide the Joffre member were originally centred on thin layers of porcellanites and by changes in a gamma-log (Morris, 1993; Trendall, 1969). However, a more recent classification subdivides the Joffre member into seven separate units (J1-J7) based on lithological differences (Fig 3) (Pickard, 2002). In this classification, each new unit starts with a shale-chert layer, followed by the classical BIF succession (i.e. BIF meso-banding and micro-banding). The Joffre Member also contains characteristic stilpnomelane layers (<1 cm) and bands of siliceous mudrocks/porcellanites (mm's to tens of cm's). Zircons from these layers have been used to date the base of the Joffre member at 2459 +/- 3 Ma and the top of the Joffre member at 2454 +/- 3 Ma. These ages were used to constrain a sedimentation rate for the Joffre member of approximately 15 m/Myr (Pickard, 2002).

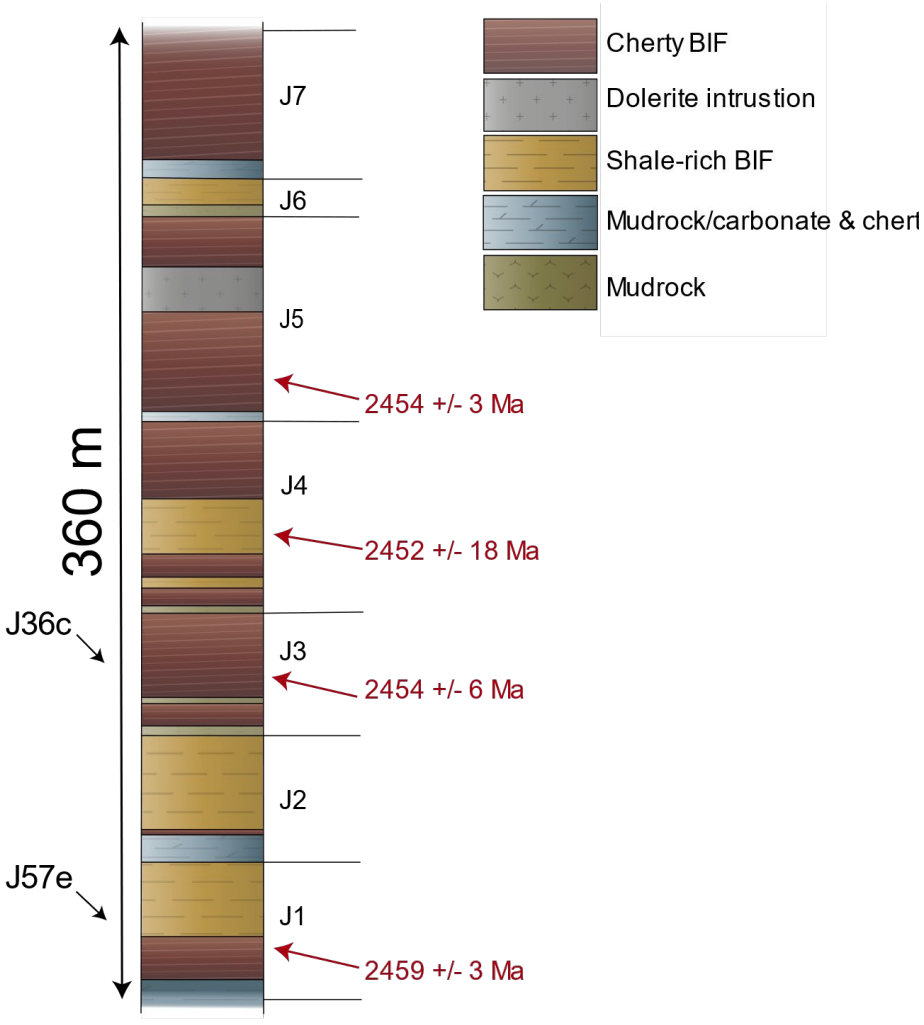


***Fig 3 –*** *The subdivision of the Joffre Member Core based on lithological differences as proposed by (Pickard, 2002). Included are the positions of the intervals that were used in this study, with J36c coming from a Cherty (i.e. classical) BIF and J57e coming from a Shaly BIF. Ages were derived from Pb-Pb dating of zircons founds in small stilpnomelane layers that are characteristic for the Joffre Member (Pickard, 2002).*

# 4 Methodology

## 4.1 Interval description

We received the half-core intervals of the Joffre member from the GSWA core repository in Peth. The core was named DD98SGP001 (Diamond Drill core 1998 Silver Grass Peak #001) and was produced as part of the Rio Tinto project in the Silvergrass Peak area of the Hamersley province, which is located approximately 50 km southeast of Pannawonica and 150 km northwest of Wittenoom. We selected two half-core intervals from the Joffre Member based on their conspicuous Knox cyclothem (~3-10 cm), which we took from tray 36 and tray 57 respectively. Note that tray 36 corresponds to a core depth of 257 m and tray 57 corresponds to a core depth of 343 m (Fig 3). Within tray 36, we selected a ~60 cm interval from the third row, which we accordingly named J36c (with J referring to the Joffre Member, 36 referring to the tray, an c corresponding to the third row). Within tray 57, we selected a ~50 cm interval from the fifth row, which we called J57e (Fig 4). Thin sections were made for both interval J57e and J36c and capture approximately one Knox cyclothem (Fig 5).

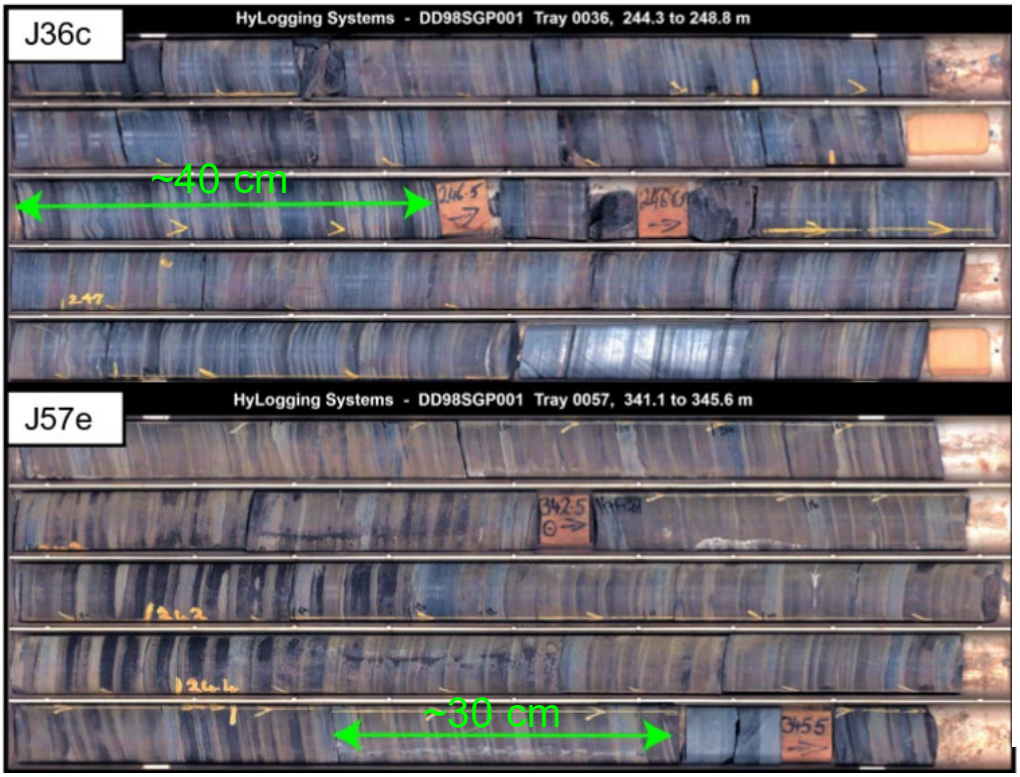


***Fig 4 –*** *The two selected trays of drill-core DD98SGP001 from which the sample intervals were taken. The trays capture one meter of stratigraphy of the Joffre Member and the location of the selected intervals is indicated with a green arrow. We selected the intervals based on their strong Knox cyclothem that fluctuated on a ~5-15 cm scale.*

## 4.2 Crushing

The core interval of J36c and J57e were sawn in horizontal slices with an Accutom 10 precision saw (Fig 5). The spacing between the saw-lines was either 3 or 5 millimetres, although both intervals also contained some thicker slices (up to a cm) due to spatial limitations of the sample holder. Consequently, the thicker slices were split with the MK-170 Wet Cutting Trim Saw. Note that some material loss (~ 1-2 mm) occurred from the saw cuts as a result of the larger saw blade. In total, interval J36c was sawn into 60 slices and interval J57e was sawn into 45 slices. These slices corresponded to the measure points of the subsequent geochemical analyses. We decided against a smaller spacing than 3 mm to obtain enough material for geochemical analyses. All the sample slices

were decontaminated with a Soxhlet extractor at the Geolab of the University of Utrecht, in which methanol and dichloromethane were used as solvents to remove remaining traces of non-primary carbon from the sample surfaces.

Following this, we crushed most of the decontaminated slices of interval J36c according to the *tungsten carbide protocol.* However, during the research it was found that carbide contamination (i.e. carbide derived from the grinding vessel) could offset the original $\delta^{13}C_{org}$ signature of the samples to more negative values. In contrast, the $\delta^{13}C_{carb}$ and Wt% $C_{org}$ remained unaffected by this external contamination (Appendix 2). Since the $\delta^{13}C_{org}$ was of interest as well, a new crushing protocol was developed to crush the few remaining samples of interval J36c and all of the samples from interval J57e. This procedure was denoted as the *Corundum protocol*. Both protocols are briefly described in the following section.

The *tungsten carbide protocol* started by shattering the sample slices with a geological hammer to achieve a first-order size reduction. Special care was taken to 1) prevent mixing of individual slices with externally derived material by working in an enclosed environment and 2) to prevent cross-contamination of the individual samples by upholding a rigorous cleaning routine; the hammer was continuously washed with isopropanol and dried with compressed air. In addition, the slices were shattered on a piece of aluminium foil that was folded to prevent it from tearing and which was renewed for every sample. Slice fragments were transferred to iron cups, either by using the aluminium foil as a funnel or by picking individual pieces with a pincher. The iron cups were inserted in a Herzog HP-MA tungsten carbide grinder to further reduce the grainsize. Importantly, the Herzog cleaned itself with quartz sand, deionized water, and compressed air after crushing a sample, which therefore prevented cross-contamination.

The *corundum protocol* started by shattering the sample slices with a Mäder pressen EP 500-40 manual press with modified corundum tip inside a corundum collecting vessel. During this procedure the samples were kept wet with deionized water to minimalize material loss and to prevent the dispersion of crocidolite fibres (See Appendix 1). This was followed by adding 5 corrundum grinding balls to the collecting vessel and crushing the samples for 10 min at a speed of 250 rmp inside a Fritsch planetary ball mill Pulverisette 5. Importantly, cross-contamination of the sample was prevented by flushing the collecting vessels on a sample-to-sample basis with demi water and by crushing quartz sand for an additional 10 min. Finally, the samples were dried inside an Elbanton A-Hypothermia cabinet for several days.

### 4.3 Analyses of organic carbon and nitrogen

The crushed samples were decalcified prior to the measurements of the Wt% $C_{org}$ and the $\delta^{13}C_{org}$ analyses (Appendix 3), whereas the non-decalcified samples provided the direct starting material for measuring the Wt% $C_{total}$, Wt% $N_{total}$, and $\delta^{15}N_{total}$. During the decalcification procedure the samples were first flushed several times with 1 M HCl to completely remove the carbonate fraction. Following this, the samples were washed with deionized water and dried for 72 hours inside a F6010 Thermolyne furnace. Since BIFs are characterized by very low concentrations of organic matter, relatively large amounts of decalcified material (~30 – 100 mg) were needed for accurate EA-IRMS analyses. The material was weighed with a Sattorius ME5 microscale and transferred to small tin cusps. The cusps were captured between the two ends of a pincher and carefully squeezed into a spherical shape. This spherical shape was needed to promote a thorough combustion in the element analyser and to ensure a smooth sample transport within the automatic sampler. Sample contamination by external organic material was prevented through working in a confined area that was equipped with a HEPA filter. The samples were analysed with a Thermo Scientific™ EA IsoLink™ IRMS System at

the Geolab of the University of Utrecht. For a more thorough understanding surrounding the decalcification procedure, sampling strategy and the procedures surrounding the IRMS, the reader is referred to Appendix 3.

### 4.4 Analyses of the carbonates

The non-decalcified samples also provided the starting point for measuring the $\delta^{13}C_{carb}$ and $\delta^{18}O_{carb}$ signatures of the carbonate fraction. We used two different preparation methods prior to analyses with the Finnigan™ MAT 253 Stable Isotope Ratio Mass Spectrometer. The initial test samples of J36c and J57e were *pepared offline*, whereas the rest of the samples of J57e were prepared for *automated sampling* in a GasBench DI-IRMS. We briefly describe both preperation methods below. For a deeper understanding surrounding the sampling sequence and the operating conditions of the DI-IRMS, the reader is referred to Appendix 3.

For the *offline preparation*, we weighed approximately 60 mg of sample material and transferred it to a separate compartment of a distillation tube. The second compartment was carefully filled with 110% phosphoric acid using a pipette. The distillation tubes were connected to Claisen Adapters and brought to a high vacuum ($10^{-5}$ torr). The samples were subsequently placed in preheated oil at a temperature of ~115 °C and the phosphoric acid was added to the sample material when they had a similar temperature to the oil (after ~15 minutes). By forcing this reaction to occur at elevated temperatures, it was possible to retain the original oxygen isotope signature of the carbonates in the released carbon dioxide. The combined distillation and Claisen were held approximately one hour inside the oil to guarantee a thorough reaction. The carbon dioxide of the reactions was transferred to Vacuum Takeoff Adapters by using a *freeze trap* of liquid nitrogen (-150 °C) on a vacuum line. During this process, cooled ethanol (-80 °C) was placed around the vacuum line to trap water vapour.

For the *GasBench preparation*, we weighed approximately 150-1500 $\mu$m sample material and transferred these into sample vials. The exact amount of sample material depended on the estimated carbonate concentration that was constrained from the decalcification procedure. The sample vials were mounted on a portable sample tray and flushed with helium. The portable sample tray was inserted into the GasBench, which heated the sample vials to approximately 70 °C. Following this, a few droplets of anhydrous phosphoric acid (103%) were automatically added by the GasBench to initiate the dissolution of the carbonates. The reaction lasted for ~28 hours to guarantee that the carbonates were fully dissolved (Appendix 3).

### 4.5 ICP-OES analyses

We selected 9 representative samples from interval J36c and one internationally recognized soil standard (ISE921) for ICP-OES analyse (Fig 5). Approximately ~125 $\mu$m of crushed sample material was weighed with a Mettler Toledo New classic MS analytical balance and transferred to 30 ml Savillex Perfluoroalkoxy alkanes (PFA) destruction vessels. Following this, 2.5 ml of 48% hydrofluoric acid (HF), 1.5 ml of 65% nitric acid ($HNO_3$), and 1 ml of 72% perchloric acid ($HClO_4$) were added to the vessels, which were placed on a hotplate (90 °C) for overnight to promote a thorough sample digestion. The temperature of the hotplate was subsequently raised to 140 °C, which initiated the evaporation of the remaining acids and effectively dried the samples to a gel-like substance. The evaporation processes lasted for about 3-4 hours, after which 25 ml of 6% nitric acid ($HNO_3$) was added to the vessels to keep the dissolved sample in solution and to prevent the reprecipitation of solid phases. The vessels were placed on the hotplate (90 °C) for again overnight and weighed to determine the dilution factor. Following this, approximately 5 ml of sample solution was transferred with a pipette from the PFA destruction vessels to 10 ml Greiner sample tubes, the latter which were analysed with the Avio 500 ICP-OES. The operating conditions and selected spectral omission lines along with an in-depth description of the ICP-OES analyses can be found in Appendix 3.

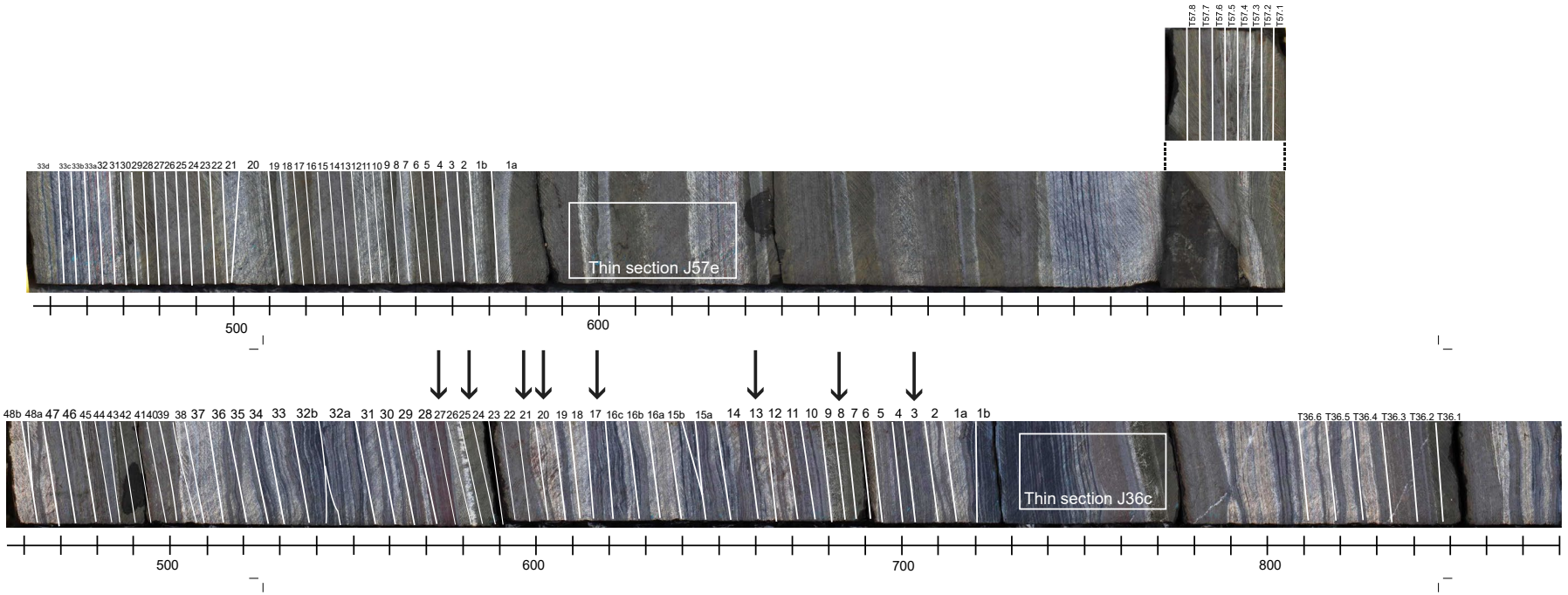


***Fig 5 –*** *The sampling locations for the quarter core intervals of J57e and J36c. Interval j36C was divided into mostly slices of ~5 mm, although we increased this resolution to ~3 mm for the pronounced green and white layers. The thicker slices (>5 mm) are a result of limitations of the sample holder. In contrast, we analysed most of J57e at a constant resolution of ~3 mm. We carried out our test analyses on the right parts of the selected intervals, which for J57e was done on the supplementary quarter core. Arrows in J36c indicate the samples that were selected for ICP-OES analyses. The white squares highlight the parts of the intervals that were selected for thin section analyses. It may appear that sample 1b and 1a are interchanged, but this is not the case.*

# 5 Results

## 5.1 The mineralogical facies of the Knox cyclothem

The Knox cyclothem in interval J57e and interval J36c (representing *shaly BIF*) can be divided into three main mineralogical facies that systematically alternate within both intervals. For interval J57e, these facies are the chert shaly BIF (CSB), the oxide shaly BIF (OSB), and the siderite shaly BIF (SSB). For interval J36c, these facies are the chert classic BIF (CCB), the oxide classic BIF (OCB), and the siderite classic BIF (SCB) (Table 1). The mineralogically distinct facies may be subdivided into different mesobands of varying thickness (Fig 7). Importantly, the conceptual model that is presented at the end of this report will evaluate the deposition of BIF in terms of the mineralogical facies and not the mesobands, although the latter will still be occasionally discussed throughout this study.

| Facies | Description | Corresponding mesobands | Interpretation* |
|---|---|---|---|
| **Shaly CHert BIF (SCB)** | These facies are dominated by chert, with lesser amounts of carbonate, hematite, and magnetite. Riebeckite may sometimes appear as microbands or mesobands, in which case it thickens the SCB and consequently the Knox cyclothem. | - Microbanded chert<br>- Riebeckite mesoband<br>- Silicate mesoband | These facies formed during periods of a relatively low Fe(III) and organic carbon flux in a shallower marine environment with respect to the CCB. The chert represents background precipitation of Si. The silicate mesobands may have formed during shorts periods of enhanced terrigenous input. |
| | | - | |
| **Shaly Oxide BIF (SOB)** | These facies are dominated by hematite, magnetite, and carbonate with a lesser amount of quartz. Euhedral Riebeckite is common. | - Microbanded oxide | These facies formed during periods of a high episodic input of Fe(III) and a moderate flux of organic carbon in a shallower marine environment with respect to the COB. DIR was likely active during the deposition of these facies. |
| **Shaly Siderite BIF (SSB)** | These facies are dominated by (sub)spherical and coarse carbonates and contain a significant amount of stilpnomelane. Fe-oxides and chert/quartz are relatively scarce. | - Silicate carbonate mesoband<br>- Carbonate mesoband | These facies formed during periods of a high episodic input of terrigenous material and a high flux in a shallower marine environment with respect to the CSB. DIR was likely active during |

| | | | | |
|---|---|---|---|---|
| | | | | the deposition of these facies. |
| **Classic Chert BIF (CCB)** | These facies are similar with respect to the SCB apart from the presence of the silicate mesoband. | - | Microbanded chert<br>Riebeckite mesoband | These facies formed during periods of a relatively low Fe(III) and organic carbon flux in a deeper marine environment with respect to the SCB. |
| **Classic Oxide BIF (COB)** | These facies are similar with respect to the SOB apart from the presence of a thin hematite mesoband. | - | Microbanded oxide<br>Hematite mesoband | These facies formed during periods of a high episodic input of Fe(III) and a moderate flux in a deeper marine environment with respect to the SOB. DIR was likely active during the deposition of these facies. Secondary hematite recrystallization set these facies apart from that of the shaly BIF interval. |
| **Classic Siderite BIF (CSB)** | These facies are dominated by (sub)spherical and coarse carbonates and further contain significant amount of quartz and fine stilpnomelane. These facies differ from the SSB mostly in that they contain biotite and pyroclastic debris. | - | Biotite silicate carbonate mesoband<br>Hematite carbonate mesoband | These facies formed during periods of a high episodic input of terrigenous material and a high flux of organic carbon in a deeper marine environment with respect to the SSB. DIR was likely active during the deposition of these facies. Furthermore, the terrigenous input may have been dominated by pyroclastic material. |

***Table 1**: an overview of the six main facies that defined the Knox cyclothem in our intervals and which are further discussed in the conceptual model. Included is a short description of the mineralogy of the facies and an interpretation (indicated by the star) of the depositional environment. The latter is discussed in detail in the discussion.*

## 5.2 Description of the mesoband sequence

The mineralogically distinct facies of interval J57e that represent the *shaly* BIF can be subdivided into a sequence of 5 mesobands (Fig 7). These are in ascending order: 1) a chert dominated mesoband with a distinctive *beige* to *yellowish* colour and a relatively widely spaced internal microbanding (>1 mm). We termed this the *microbanded chert*. 2) a mesoband that is characterized by tightly spaced (> 200 µm) magnetite and hematite laminae with a distinctive *black* colour. We called this the *microbanded oxide*. 3) a *brown* mesoband that lacks internal microbanding and which is dominated by Fe-silicates and carbonate minerals. We named this the *carbonate silicate mesoband.* 4) a thin *white* carbonate mesoband that lacks internal microbanding. We termed this the

*carbonate mesoband.* And finally, 5) a thin *green* mesoband that contains internal microbanding and which is dominated by Fe-silicates. We called this the *silicate mesoband*. The sequence of these mesobands in interval J57e is remarkable constant, although the respective thickness of the mesobands differs systematically throughout the interval, which ultimately results in a different expression of the length of the Knox cyclothems. Specifically, the *beige* microbanded chert shows a large variance in thickness; in the middle of the interval of J57e this mesoband become vanishingly thin. In contrast, at the far ends of the interval, *blue* riebeckite mesobands seem to develop within the *beige* microbanded chert, which consequently results in much thicker expression of the Knox cyclothem, although it should be noted that the riebeckite mesobands by themselves do not define and/or follow the Knox cyclothem. An overview of the mesobands that define the Knox cyclothem of interval J57e is presented in Fig 6.

The mineralogically distinct facies of interval J36c (representing *classic BIF*) can be subdivided into a sequence of 6 mesobands (Fig 7). These are in ascending order: 1) a carbonate and silicate mesoband with a distinctive *brown* colour and an absence of internal microbanding. Importantly, this mesobands contains flakes of biotite, which is why we termed it the *biotite carbonate silicate mesoband*. 2) a thin *white* carbonate mesoband that lacks internal microbanding and contains flakes of hematite. We called this the *hematite carbonate mesoband. 3)* a thin mesoband that is characterized by *red* to *blackish* hematite and which lacks internal microbanding. We called this the *hematite mesoband*. 4) a mesoband that is characterized by tightly spaced magnetite and hematite laminae with a distinctive *black* colour. This mesoband was mineralogically and texturally similar to its equivalent of interval J57e, which is why we also called it the *microbanded oxide.* 5) a chert dominated mesobands with a distinctive *beige* to *yellowish* colour and a clear internal microbanding. This mesoband was mineralogically and texturally similar to its equivalent of interval J57e, which is why we termed it the *microbanded chert* as well. And finally, 6) another *black* microbanded oxide. The sequence of mesobands in interval J36c is remarkable constant and the thickness of the microbanded chert does not fluctuate to the same extent as seen in interval J57e. Consequently, the length of the Knox cyclothem remains relatively constant throughout the interval.

There are several important similarities between the mesobands that define the mineralogical facies in the Knox cylothems of interval J57e and interval J36c. Firstly, the *brown* carbonate silicate mesoband of interval J57e and the *brown* biotite carbonate silicate mesoband of interval J36c are broadly similar in terms of mineralogy and textures. The main difference is that the *brown* biotite carbonate silicate mesoband contains flakes of biotite and a larger contribution of stretched quartz aggregates. Furthermore, the *white* carbonate mesoband of interval J57e and the *white* hematite carbonate mesoband of interval J36c are texturally and mineralogically similar, with the sole exception being the tabular hematite flakes. The contacts between these *white* (hematite) carbonate mesobands and the overlying mesobands may appear wavy and sharp, abruptly cutting off the overlying microbanding. This feature is restricted to the *white* (hematite) carbonate mesobands only and does not occur between other mesobands (Fig 7 for overview transitions between mesobands). Furthermore, interval J57e and interval J36c are identical in terms of their *beige* microbanded chert mesobands, their *black* microbanded oxide mesobands, and their *blue* riebeckite mesobands.

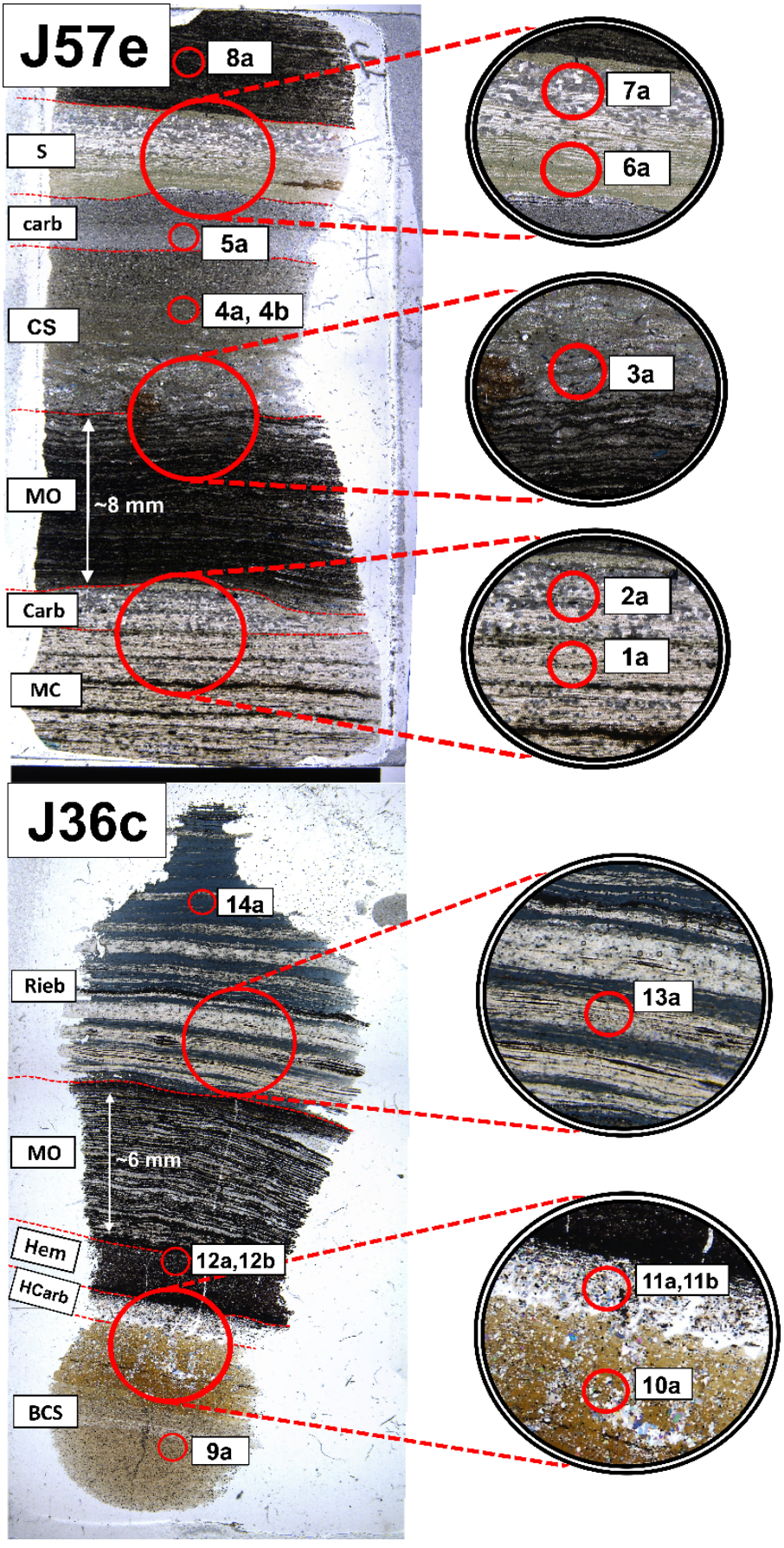


***Fig 6*** *– Overview of the thin-section scans for interval J57e and j36c. Both thin sections capture approximately one Knox cyclothem (i.e. the succession of mineralogically distinct mesobands). The location of the microscopic observations is indicated with small red circles and correspond to the pictures shown in Figure 9 and 10. For J57e: MC is microbanded chert, MO is microbanded oxide, CS is the carbonate silicate mesoband, Carb is the carbonate mesoband, and S is the silicate mesoband. For J36c: BCS is the biotite carbonate silicate mesoband, HCarb is the hematite carbonate mesoband, Hem is hematite mesoband, and Rieb is the riebeckite mesoband.*

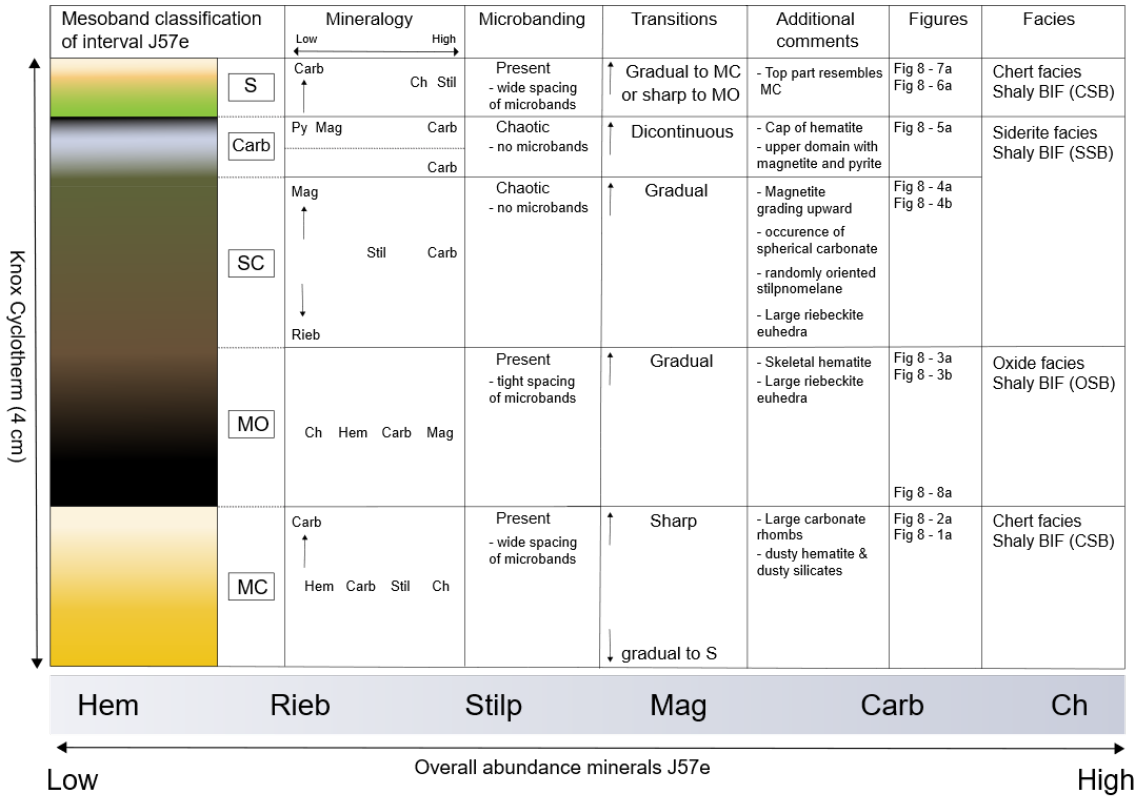


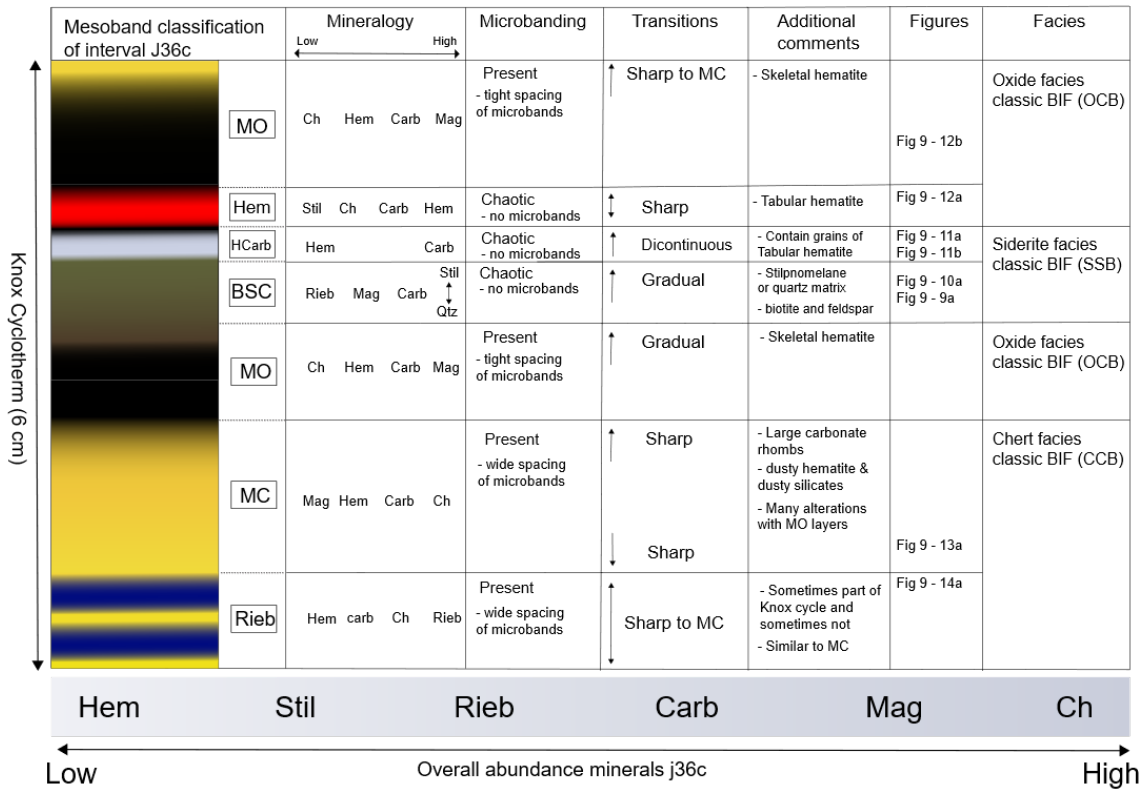


***Fig 7 –*** *Overview of the most important petrographic observations along the Knox cylothem for both intervals. Included are the transitions from one mesoband to another mesoband, the presence of microbanding in the mesobands, and the dominant mineralogy of the individual mesobands. The bar at the bottom of the figures gives an estimate of the overall mineralogy of the intervals and implies that J36c was characterized by a relatively higher oxide content whereas J57e was characterized by a relatively higher carbonate content. The succession of mesobands can be summarized into different facies (see discussion).*

### 5.2.1 Microbanded chert mesobands

The microbanded chert mesobands are present in both interval J36c and J57e. The chert in the microbanded chert is generally fine grained (5-10 µm) and constitutes a mosaic of interlocking subhedral grains. We found different scales of microbands (>1 mm up to 5 µm) in the chert matrix, most of which consist of stilpnomelane needles, microgranular *dusty* hematite/Fe-silicate granules, coarse magnetite euhedra (40-100 µm), and rhombohedral (<200 µm) to microcrystalline (1-5 µm) carbonates. The carbonate mineralogy is dominated by these larger rhombohedral crystals (~100-200 µm), which occasionally line up to form microbands (Fig 8 – 2a). The rhombohedral carbonates can be recognized by their iridescent coloured edges, their coarse and well-developed crystal habits, and the numerous inclusions of chert, stilpnomelane needles, and dusty hematite/Fe-silicate granules in their cores (Fig 8 – 2a, Fig 8 – 7a). Microbands of subhedral microcrystalline carbonate (1-5 µm) are less common in the microbanded chert (Fig 9 – 13a). Occasionally, hematite-coated stilpnomelane spherules (~5 µm) are visible within the interion of chert microbands (Fig 8 – 1a). Analogue to this are some of the stilpnomelane needles (1-5 µm) and Fe-silicate granules (<1 µm), both of which show evidence of hematite coatings. The *greenish* stilpnomelane needles (1-4 µm) line up along – or make a small angle with – the orientation of their corresponding microbands (Fig 8 – 2a). Magnetite is an uncommon phase in the microbanded chert and occurs sporadically as coarse euhedral crystals (~40-100 µm) or thick microbands (~250 µm). Finally, the dusty hematite/Fe-silicate microbands and carbonate rhombohedra are frequently associated with riebeckite and fibrous crocidolite (Fig 8 – 2a). The riebeckite typically grows as rosettes, from which needles and fibres of crocidolite expand outwards. Petrographic relations further show that the riebeckite growth is texturally related to the breakdown of rhombohedra carbonates (Fig 8 – 2a).

### 5.2.2 Microbanded oxide mesobands

Microbanded oxide mesobands are present in both interval J36c and J57e and differ mostly from the microbanded chert in that they are characterized by a lower contribution of quartz, a higher contribution of oxide minerals, and a higher contribution microcrystalline carbonate. Importantly, the quartz is stretched and much finer (> 5 µm) than the mosaic chert found in the microbanded chert (Fig 9 – 12b). Hematite microbands (>100 µm) appears as skeletal aggregates of connected but individually subhedral crystals. The holes and caverns that define this skeletal aggregate are filled with microcrystalline carbonates (1-5 µm) and quartz (Fig 8 – 8a, Fig 9 – 12b). Magnetite microbands consists of massive bands (>200 µm) that constitute a network of connected and interlocked euhedral crystals. These crystals contain numerous inclusions of microcrystalline carbonate and to a lesser extent skeletal hematite and clearly overgrow a matrix of stilpnomelane, carbonate, and quartz (Fig 8 – 8a). Randomly distributed magnetite euhedra overgrow all other phases, including magnetite microbands and riebeckite crystals. The riebeckite in the microbanded oxide appears as diamond and tabular shaped crystals that crosscut some of the magnetite microbands. However, these riebeckite crystals themselves are overgrown by individual magnetite euhedra (Fig 8 – 3a). Finally, a well-crystalized quartz fracture in J36c vertically crosscuts some of the finer magnetite microbands, while leaving some of the massive magnetite microbands undisturbed (Fig 9 – 12b).

### 5.2.3 Carbonate silicate mesobands

The *brown* carbonate silicate mesoband is present only in interval J57e and consists almost exclusively of carbonate and randomly oriented stilpnomelane needles. The carbonate occurs in two flavours: 1) microcrystalline carbonate (5-15 µm) which has typically subspherical habits and a chaotic distribution of birefringence colours (buff pink and pale green). Most of the rounded carbonate clasts contain stilpnomelane needles in their cores and tiny inclusions of dusty hematite and dusty silicates in their interiors (Fig 8 – 4a).

Interestingly, evidence for spherical siderite grains is found in the *brown* carbonate silicate mesoband as well (Fig 8 – 4b). The core of some of these spherical carbonates consists of minute Fe-silicate and/or hematite granules (< 1 µm), although it is not possible to distinguish between these phases for sure. A second type 2) of carbonate appears coarser (>20 µm) and is characterized by a less pronounced birefringence, a subhedral crystal habit, and straight crystal boundaries. Importantly, the interiors of these carbonates contain many randomly oriented stilpnomelane needles and numerous dusty hematite/Fe-silicate inclusions (Fig 8 – 4b). Stylolite-like features are occasionally present in the *brown* carbonate silicate mesobands and appear dark and wavy in plane polarized light. These stylolite-like features are typically enveloped by the second type of carbonate (Fig 8 – 4a). Finally, chert, hematite, and magnetite microbands are all distinctively absent in the mesoband.

### 5.2.4 Carbonate mesobands

The *white* carbonate mesoband (>5mm) is present only in interval J57e and can be subdivided into two domains: 1) a carbonate-rich domain and a 2) carbonate-, magnetite-, and pyrite-rich domain. The carbonate-rich domain is characterized by carbonate rhombohedra (> 100 µm) that are characterized by a homogenous and relatively low-order birefringence in their interiors (i.e. second order pink, blue, green) and a high iridescent birefringence on their edges. The carbonates contain many inclusions of stilpnomelane needles, dusty hematite/Fe-silicates and look like a larger variant of the second type of carbonate present in the *brown* carbonate silicate mesobands. The space in between the large carbonate rhombohedra are filled in with subhedral and microcrystalline carbonate grains, which appear similar to the first carbonate in the *brown* carbonate silicate mesoband. The carbonate-, magnetite- and pyrite-rich domain is characterized by similar carbonates described above, but now with an appreciable amount of magnetite and pyrite as well. This gives the upper domain of the *white* carbonate mesoband a blackish hue. The euhedral magnetite contains small carbonate inclusions, whereas the pyrite is devoid of inclusions (Fig 8 – 5a).

### 5.2.5 Silicate mesobands

The *green* silicate mesoband is present only in interval J57e and is relatively thin (< 5mm), consisting almost exclusively of microbanded stilpnomelane needles and quartz. The stilpnomelane appears greenish and is occasionally associated with tiny euhedral riebeckite crystals (~30 µm), similar to those found in the biotite carbonate silicate mesoband (Fig 8 – 6a). Carbonates, hematite and magnetite are rarely present in the *green* silicate mesoband. The *green* silicate mesoband looks therefore somewhat similar to the *beige* microbanded chert, although it is characterized by a much higher contribution of stilpnomelane and a much smaller contribution of chert.

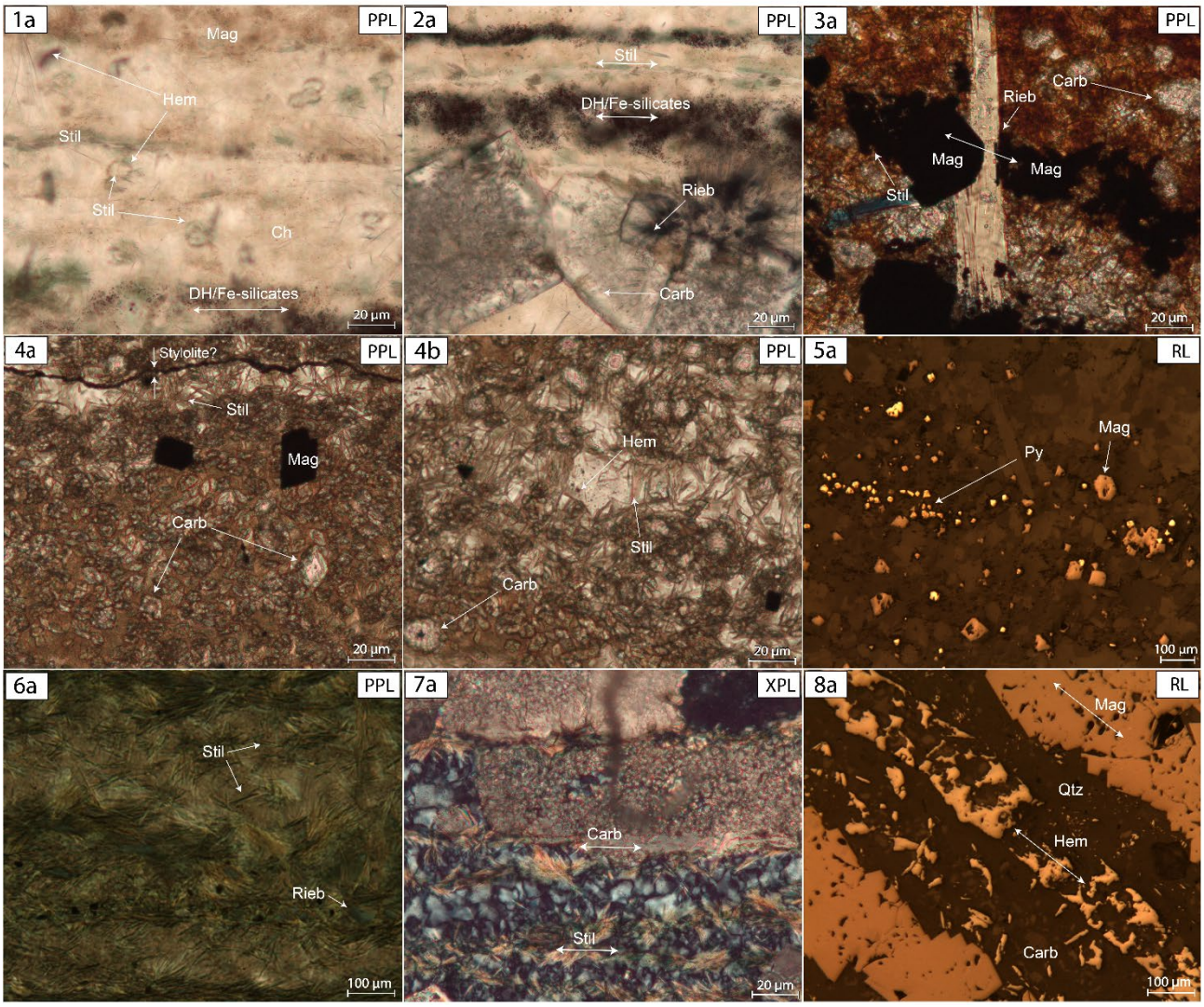


***Fig 8 –*** *Microscopic observations of interval J57e in plane polarized light (PPL), cross polarized light (XPL), and reflected light (RL).* ***1A)*** *chert mesoband with stilpnomelane spherules.* ***2A)*** *Coarse carbonate microbands associated with riebeckite and dusty hematite/Fe-silicate microbands.* ***3A)*** *Overgrow relations between magnetite, carbonate, and riebeckite.* ***4A)*** *Different generations of carbonate associated with a stylolite.* ***4B)*** *Perfect spherical carbonates in close association with coarser carbonates.* ***5A)*** *Magnetite and pyrite that are distributed in a carbonate matrix.* ***6A)*** *Microbanded Stilpnomelane matrix with small amounts of dispersed riebeckite.* ***7a)*** *Coarse carbonate that is associated with stilpnomelane needles and chert.* ***8a)*** *Skeletal aggregate of hematite in close association with carbonate and quartz.*

### 5.2.6 Biotite carbonate silicate mesobands

The *brown* biotite carbonate silicate mesoband is present only in interval J36c but has a comparable matrix of carbonate and stilpnomelane to the *brown* carbonate silicate mesoband of J57e. However, stilpnomelane does not appear as needles and instead comprises a fine-grained matrix that is closely associated with quartz. The quartz has a finer grainsize with respect to the mosaic chert and crystalizes in stretched out laths that follow the orientation of the microbands in other mesobands (Fig 9 – 11a). The quartz grains themselves contain dusty hematite/Fe-silicate granules (~5 µm). Furthermore, thin shards (~5 µm) and clasts (~5 µm) of feldspar and/or quartz are distributed evenly throughout the matrix (Fig 9 – 9a). This is accompanied by small euhedral riebeckites (~10 µm), which typically contain a core of quartz and/or felspar. The riebeckite aligns with but overgrows the stretched quartz aggregates, which makes it notably different from the riebeckite in other

mesobands (Fig 9 – 10a). The riebeckite is closely associated with coarse biotite (> ~40µm). The biotite overgrows the stilpnomelane and quartz matrix and aligns with the stretched quartz aggregates as well (Fig 9 – 10a). Randomly oriented magnetite euhedral are common and overgrow all the other phases (Fig 9 – 9a, Fig 9 – 10a). Finally, carbonates either appear as subhedral microcrystalline crystals or as coarser and well-developed rhombohedra. Therefore, the carbonates are similar to those of the *brown* carbonate silicate mesoband. Interestingly, lenses of microcrystalline carbonate are occasionally enveloped by stretched quartz aggregates, whereas the coarser carbonate rhombohedra overgrow the quartz aggregates and the stilpnomelane matrix. Finally, some of the coarser carbonate rhombohedra still contain a relict subhedral cores of microcrystalline carbonate (Fig 9 – 11 a).

### 5.2.7 Hematite carbonate mesobands

The *white* hematite carbonate mesoband is present only in interval J36c and shows many similarities with the *white* carbonate mesoband of interval J57e. The mesobands consists almost exclusively of carbonates. However, pyrite is notably absent and small amounts of hematite are also present, which sets it apart from the *white* carbonate mesoband. The carbonate is coarse grained (~100 µm) and can be best recognized by its low birefringence and perfect cleavage. Furthermore, the carbonates display clear lope and bulge textures, which is characteristic of recrystallization fronts (Fig 9 – 11b). The carbonates contain many inclusions of dusty hematite/Fe-silicates, although the inclusions do not define microbanding. The hematite occurs as coarse grains (50-100 µm) with a tabular habit that randomly overgrow the carbonate matrix (Fig 9 – 11b).

### 5.2.8 Hematite mesobands

The *red* hematite mesoband is relatively thin (>2 mm) and present only in interval J36c. It consists of a tight network of tabular hematite that overgrows a carbonate, chert and stilpnomelane matrix. Importantly, the carbonates do not fill the caverns and holes that are so characteristic for the skeletal hematite aggregates. Sporadic euhedral magnetite grains (~30 µm) occur within the *red* hematite mesoband, some of which contain relict cores of the tabular hematite (Fig 9 – 12a).

### 5.2.9 Riebeckite mesobands

The *blue* riebeckite mesobands are strikingly similar to the *beige* microbanded chert and occur in both intervals. The mesobands are made up of alternating mircrobands of riebeckite, magnetite, skeletal hematite, dusty hematite, and carbonate. The riebeckite occurs as massive fine-grained (~1 µm) acicular aggregates that overgrow the chert and carbonate matrix (Fig 9 – 14a). The thickness of the riebeckite microbands is laterally variable and in some cases fades out into carbonate microbands. Rosette riebeckite and associated crocidolite are also present in some parts of the chert microbands (Fig 9 – 13a).

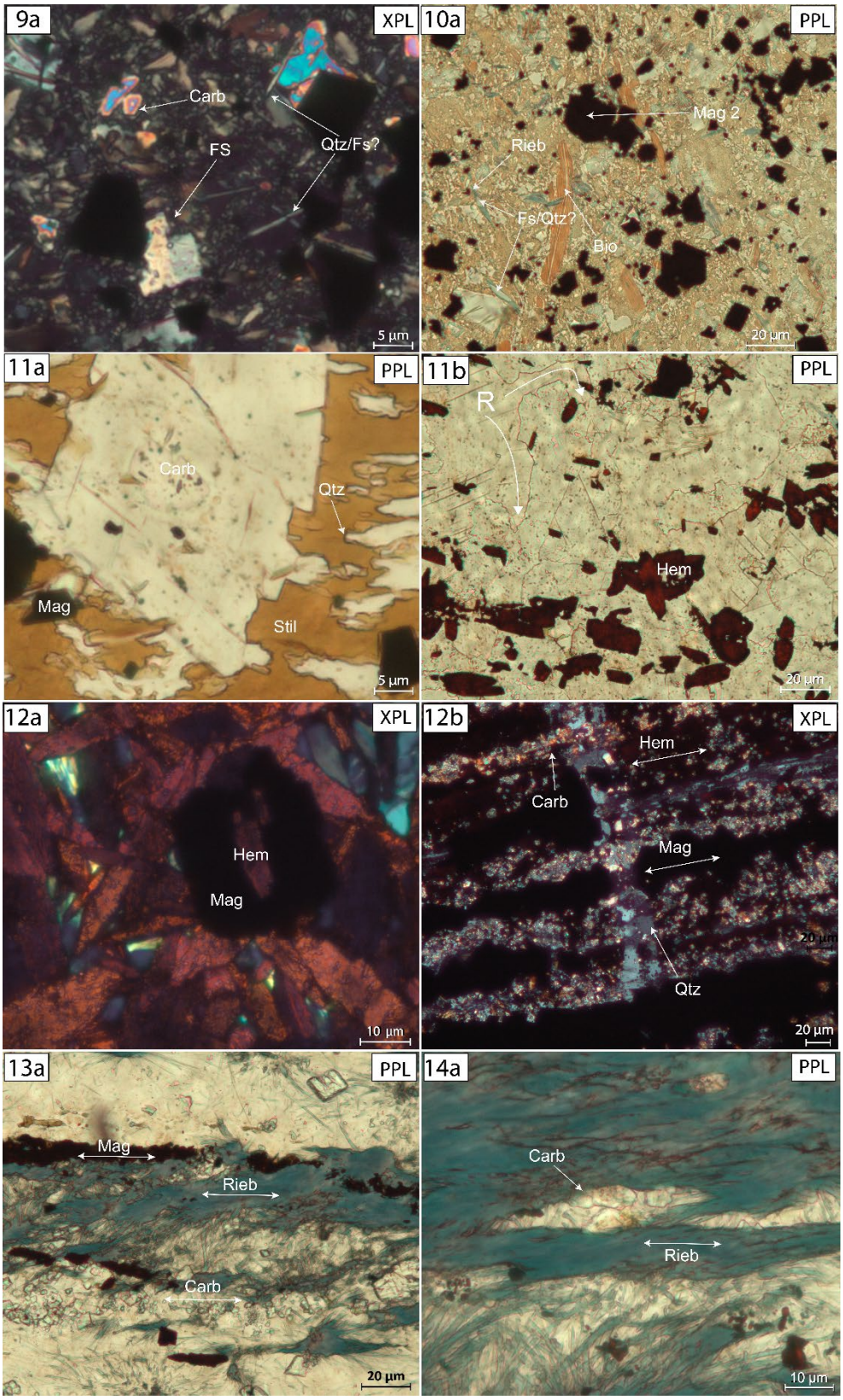


***Fig 9 –*** *Microscopic observations of interval J36c in plane polarized light (PPL), cross polarized light (XPL), and reflected light (RL).* ***9a)*** *Feldspar clasts and quartz/feldspar shards in a quartz matrix.* ***10a)*** *Biotite, riebeckite, and euhedral magnetite in a quartz/carbonate matrix.* ***11a)*** *A coarse carbonate crystal that contains a subspherical carbonate core in a matrix of stilpnomelane and quartz.* ***11b)*** *Coarse carbonate with strong evidence of recrystallization features that is indicated with a R.* ***12a)*** *Relict tabular hematite in the core of a magnetite euhedral.* ***12b)*** *Quartz fracture within the microbanded oxide mesoband.* ***13a)*** *Fibrous riebeckite microband in close relation with microcrysytalline carbonate and magnetite.* ***14a)*** *Fibrous riebeckite overgrowing a chert and carbonate matrix.*

## 5.3 (Major and) trace elements

The ICP-OES data indicates that the carbonate classic BIF facies of interval J36c are enriched in Cr, Cu, P, Ni, Al, Ba, Be, Ce, K, Mg, S, Sc, Sr, Ti, V, and Y relative to the other facies of interval J36c . In some cases, this enrichment can be extreme (e.g. 1700x more P in the *brown* biotite carbonate silicate mesobands as opposed to low background values in the other mesobands). In contrast, the *blue* riebeckite mesoband is slightly enriched in Li and Na and the oxide classic BIF facies is highly enriched in Fe relative to the other facies. The transition metals Co and W should be interpreted with care since they are highly elevated by the contamination of cemented tungsten carbide that was introduced during the sample crushing (see Appendix 4 for quality control). Finally, a few elements remained below the detection limit in all samples (i.e. Cd, Mo and Pb).

## 5.4 Analyses of organic carbon and nitrogen

The Wt% Carbonate and Wt% $C_{org}$ data of both intervals show a consistent pattern along the Knox cyclothem (Fig. 10-12). In interval J36c, the Wt% Carbonate values range between 2 and 46 Wt%, whereas the Wt% $C_{org}$ values range between 0.02 and 0.1 Wt%. The Wt% Carbonate and Wt% $C_{org}$ are systematically enriched in the white hematite carbonate mesobands relative to the rest of the Knox cyclothem (Fig 10 & Fig 12). This enrichment is characterized by an increase of the total carbonate by approximately ~30 Wt% and a doubling of the organic carbon. Such enrichment cannot be explained by pre-existing internal heterogeneity (>0.005 Wt% Corg) or analytical errors (>0.0043 Wt% Corg) and must therefore reflect an original geochemical signature characteristic for interval J36c.

In interval J57e, the Wt% Carbonate values range between 4 and 45 Wt%, whereas the Wt% $C_{org}$ values range between 0.03 and 0.09 Wt%. Although these values are similar with respect to interval J36c, the pattern itself is a little more complicated; The total carbonate displays a strong zigzag pattern, in which the Wt% Carbonate builds up steadily over a Knox cyclothem, reaching a maximum in the *white* carbonate mesoband (~40-50 Wt%), after which it abruptly drops to ~10 Wt% Carbonate in the *beige* microbanded chert. The Wt% $C_{org}$ patterns appears more chaotic compared to the Wt% Carbonate trend, although the Wt% $C_{org}$ is still systematically enriched in the *white* carbonate mesobands and systematically depleted in the *beige* microbanded chert. Therefore, the *white* carbonate mesobands are enriched in both the total Carbonate and Wt% $C_{org}$ with respect to other mesobands. Furthermore, the $\delta^{13}C_{org}$ signatures are most negative in the *white* carbonate mesobands of interval J57e, where they reach values as low as -30‰, whereas the microbanded oxides show the most positive $\delta^{13}C_{org}$ excursions of approximately -27‰. The largest observed $\Delta^{13}C_{org\ chert\text{-}oxide}$ between mesobands is therefore ~3‰, which exceeds both the analytical error and the internal heterogeneity of the EA-IRMS analyses, suggesting that the $\delta^{13}C_{org}$ fluctuations are original geochemical signatures. Supplementary information of the internal heterogeneity, analytical error, and the originality of the geochemical signatures are presented in Appendix 3.

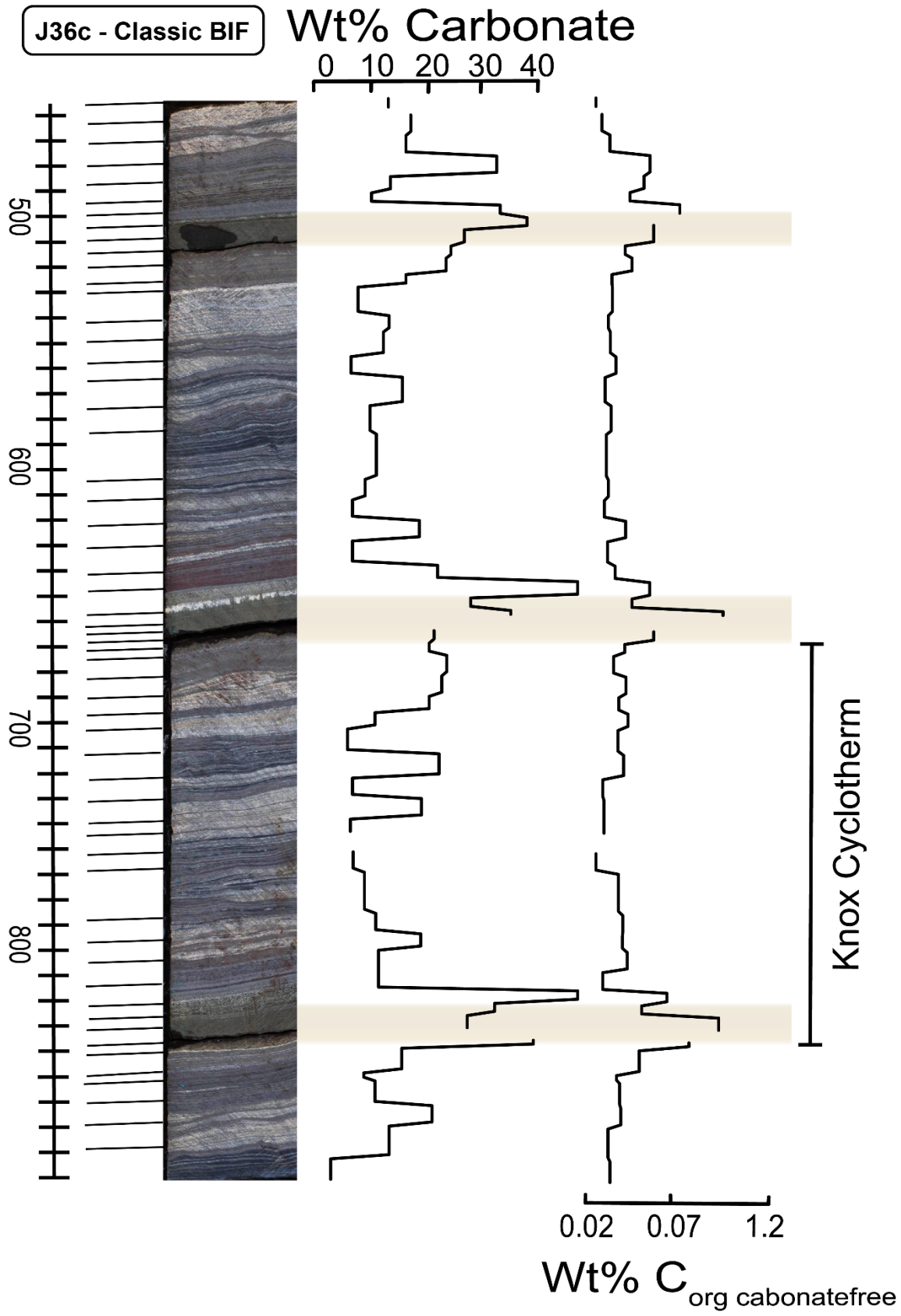


***Fig 10 –*** *The Wt% Carbonate and the Wt% $C_{org\text{-}carbonate\ free}$ plotted against the length of interval J36c. The Wt% $C_{org}$ was plotted on a carbonate free base. The brown highlights coincide with position of the biotite carbonate silicate mesobands. The position of the sample slices is included on the left side of the interval.*

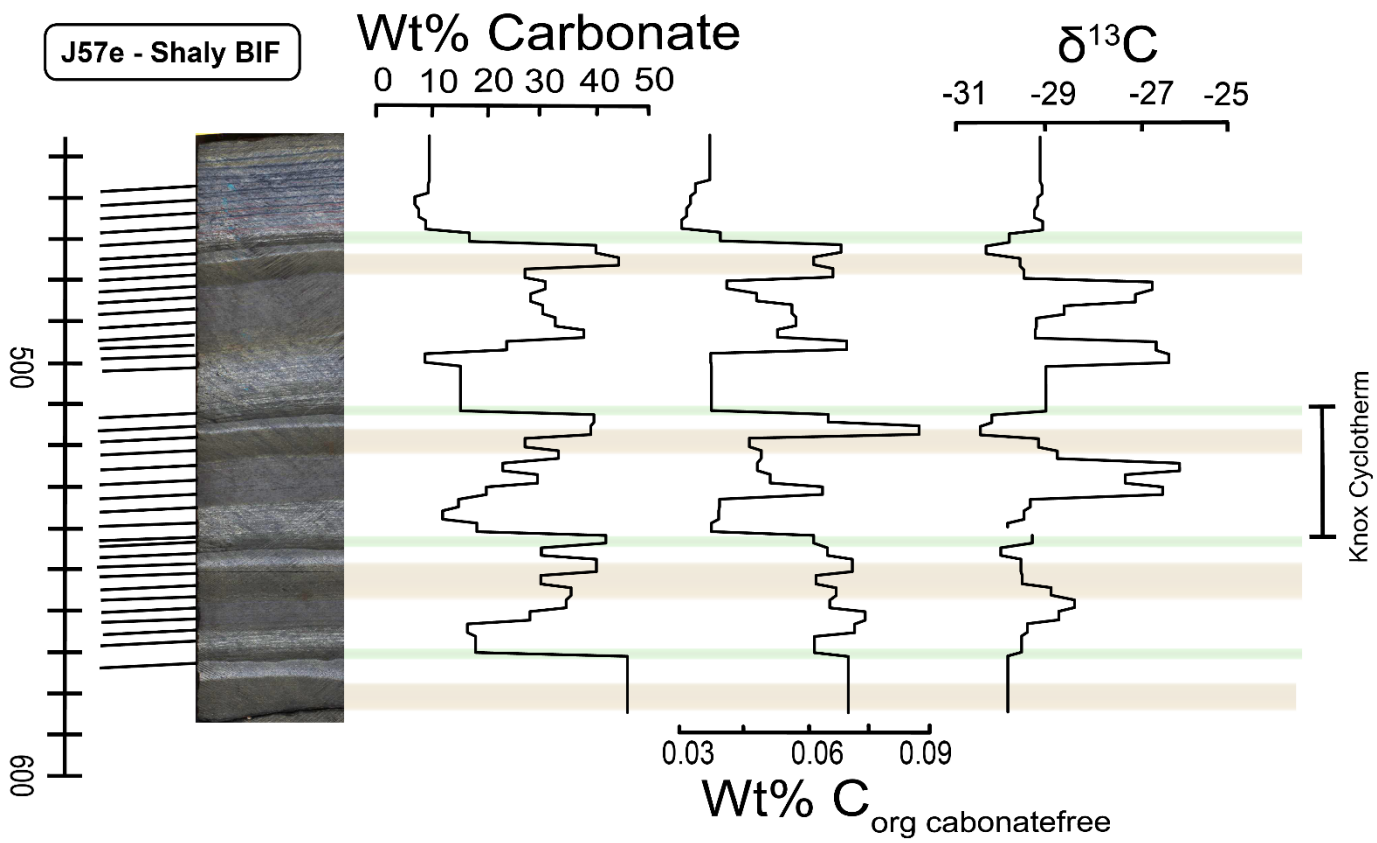


***Fig 11 –*** *The Wt% Carbonate, Wt% $C_{org\text{-}carbonatefree}$ and $\delta^{13}c_{org}$ plotted against the length of interval J57e. The Wt% $C_{org}$ was plotted on a carbonate free base. The brown highlights coincide with position of the carbonate silicate mesobands and the green highlights coincide with the position of the silicate mesobands. The position of the sample slices is included on the left side of the interval.*

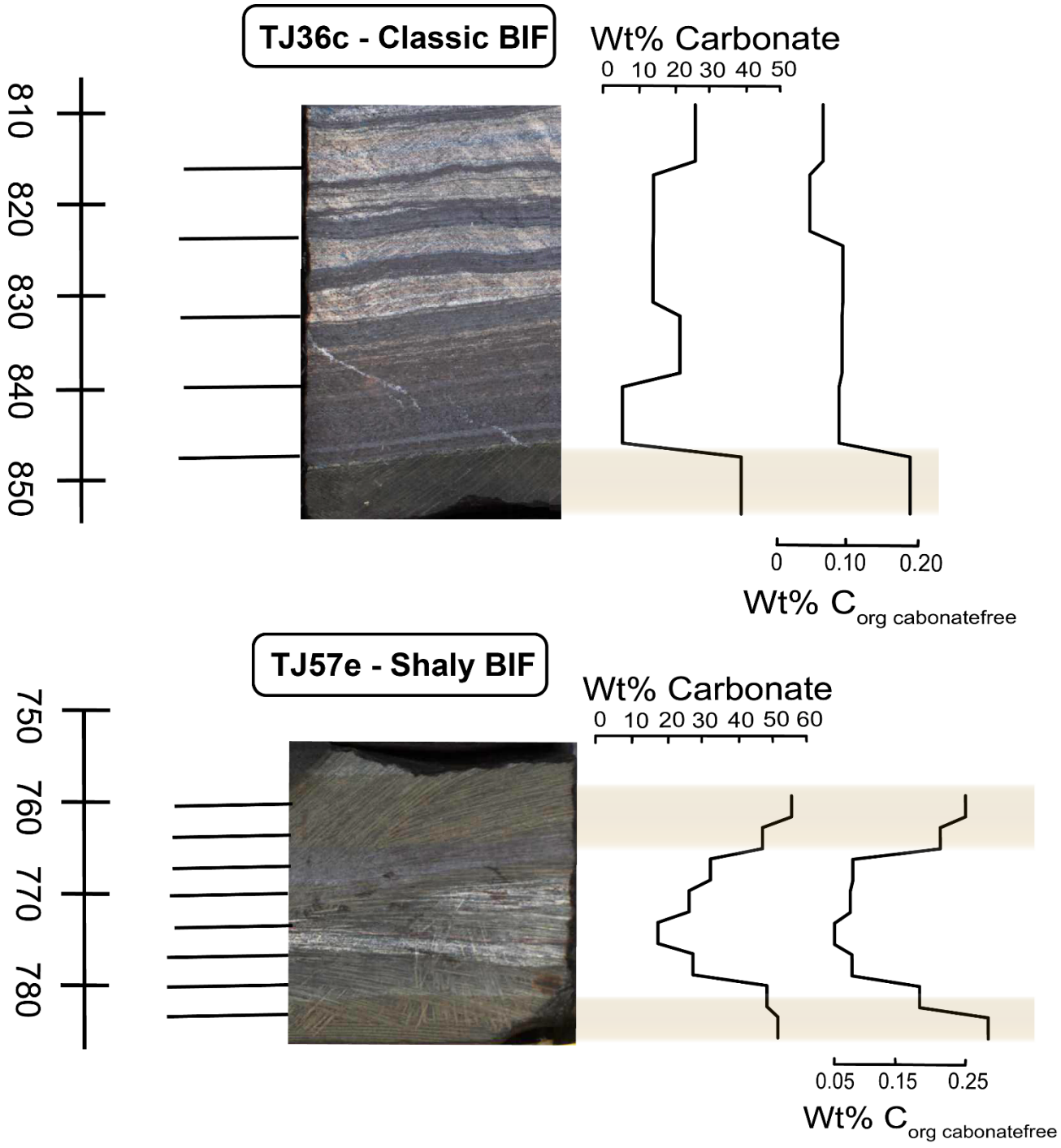


***Fig 12 –*** *The Wt% Carbonate and the Wt% $C_{org\text{-}carbonatefree}$ trends of the test samples. The brown highlights coincide with position of the (biotite) carbonate silicate mesobands. The position of the sample slices is included on the left side of the interval.*

## 5.5 Carbonate isotopes

We were not able to obtain a full stratigraphic record for the $\delta^{13}C_{carb}$ signatures along the length of interval J57e. Therefore, we opted for a sample separation based on the mineralogical distinct facies from which the carbonates were derived. The carbonates derived from the *shaly* chert facies show a wide range for the $\delta^{18}O_{carb}$ and $\delta^{13}C_{carb}$ signatures, with a maximal spread of $\Delta^{13}C_{carb}$ = 1.22‰ and $\Delta^{18}O_{carb}$ = 2.74‰. Furthermore, the average $\delta^{13}C_{carb}$ signature is -7.78‰ and the average $\delta^{18}O_{carb}$ signature is 18.69‰, which makes it the isotopically lightest facies in the Knox cyclothem. In contrast, the carbonates derived from the *shaly* oxide facies show a much more confined spread in $\delta^{18}O_{carb}$ and $\delta^{13}C_{carb}$ signatures, with a maximal $\Delta^{13}C_{carb}$ = 0.55‰ and $\Delta^{18}O_{carb}$ = 0.33‰. Furthermore, the average $\delta^{13}C_{carb}$ signature is -7.32‰ and the average $\delta^{18}O_{carb}$ signature is 20.23‰. Therefore, the *shaly* chert facies and the *shaly* oxide facies have comparable $\delta^{13}C_{carb}$ signatures, but distinctively different $^{18}O_{carb}$ signatures ($\Delta^{18}O_{carb\ –\ oxide\ vs\ chert}$ = 1.5‰). In contrast, the range of the $\delta^{18}O_{carb}$ and $\delta^{13}C_{carb}$ signatures in the *brown* carbonate silicate mesobands display a spread for $\Delta^{13}C_{carb}$ of 1.24 ‰ and a spread for $\Delta^{18}O_{carb}$ of 0.93‰. The average $\delta^{13}C_{carb}$ signature is -6.21‰ and the average $\delta^{18}O_{carb}$ signature is 20.21‰, which sets the *brown* carbonate silicate mesobands apart from both the *shaly* chert facies with respect to the $\delta^{13}C_{carb}$ and $\delta^{18}O_{carb}$ signature ($\Delta^{13}C_{carb}$ =2.02‰ and $\Delta^{18}O_{carb}$ = 1.67‰) and from the *shaly* oxide facies with respect to only the $\delta^{13}C_{carb}$ signature ($\Delta^{13}C_{carb}$ =1.56‰ and $\Delta^{18}O_{carb}$ = 0.17‰). Finally, the *white* carbonate mesobands are isotopically similar to the *brown* carbonate silicate mesobands, with a slightly lower average $\delta^{13}C_{carb}$ signature of -5.76‰ and a $\delta^{18}O_{carb}$ signature of 20.41‰. This makes the *shaly* carbonate mesoband the isotopically heaviest mesoband of the Knox cyclothem in terms of the observed $\delta^{18}O_{carb}$ and $\delta^{13}C_{carb}$ signatures. Therefore, the isotope signatures of the *shaly* carbonate facies are relatively versatile. Finally, the samples derived from carbonate facies show evidence for a weak correlation, in which a decrease in the $\delta^{13}C_{carb}$ signature is accompanied by a decrease in the $\delta^{18}O_{carb}$ signature. Using a weighted mean (York fit, 1969) we find a regression line of $y = 0.87x + 25.4$ with a $R^2$ of 0.60 (Fig 13). The $\delta^{18}O_{carb}$ and $\delta^{13}C_{carb}$ signatures for all of the samples derived from the *shaly* oxide facies and most of the samples derived from the *shaly* chert facies fall outside the range of this linear regression line.

Unfortunately, we were only able to measure a few samples (n=3) for interval J36c. The data show an average $\delta^{13}C_{carb}$ signature of -10.27‰ and a $\delta^{18}O_{carb}$ signature of 18.82‰ for the *classic* chert facies, which in terms of the $\delta^{13}C_{carb}$ signature differs substantially from that of the *shaly* chert facies of interval J57e ($\Delta^{13}C_{carb}$ =2.49‰ and $\Delta^{18}O_{carb}$ = 0.13‰). The single sample of the *classic* oxide facies shows a $\delta^{13}C_{carb}$ signatures of -9.58‰ and a $\delta^{18}O_{carb}$ signature of 19.03‰, which differs substantially from that of the *shaly* oxide facies of interval J57e ($\Delta^{13}C_{carb}$ =2.26‰ and $\Delta^{18}O_{carb}$ = 1.16‰). Consequently, the isotopic difference between the Knox cyclothem of interval J36c and J57e is much larger than the internal isotopic difference of mineralogical facies that define the Knox cyclothem in J57e.

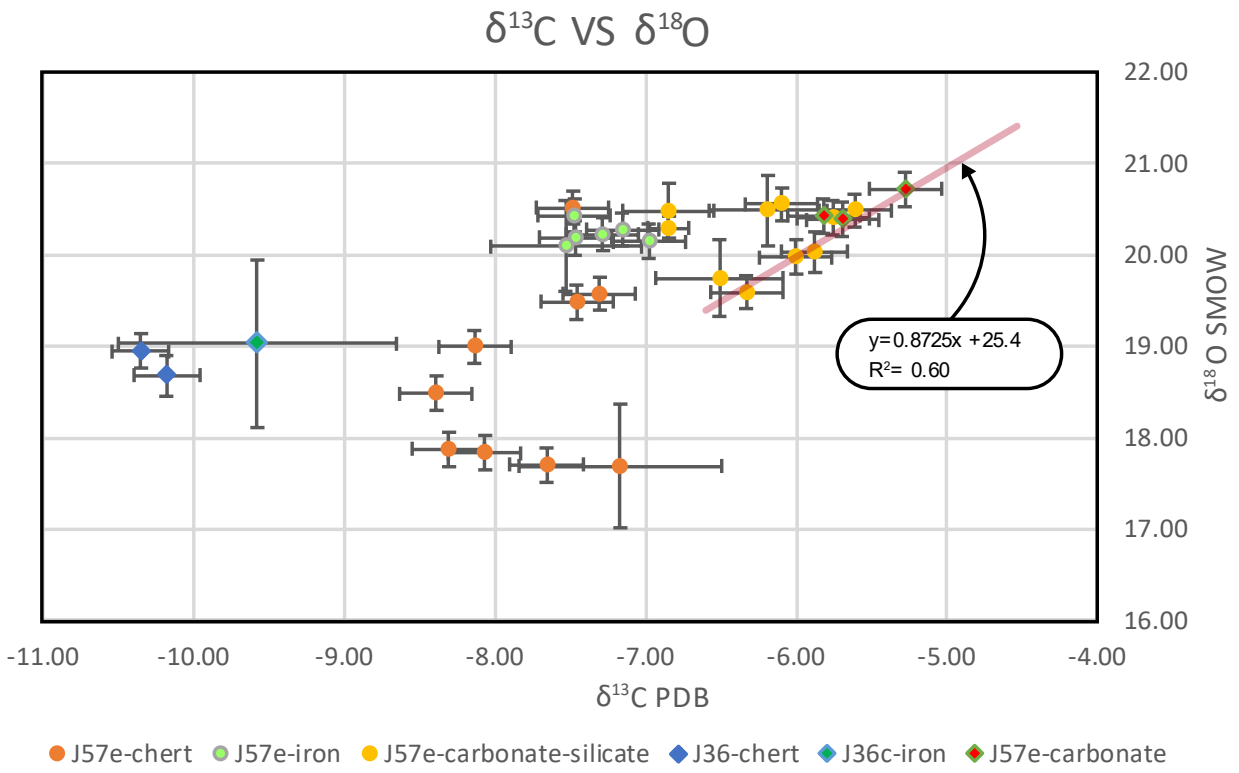


***Fig 13** – The $\delta^{18}O_{carb}$ and $\delta^{13}C_{carb}$ plot for the samples of J57e and J36c. The samples of the microbanded oxide of J57e tend to cluster in a tight group which corresponds to a $\delta^{13}C_{carb}$ signature of ~-7.3‰ and a $\delta^{18}O_{carb}$ signature of ~20.2‰. The samples of the carbonate silicate and carbonate mesobands further show a linear relation which can be expressed by a regression line ($R^2$ = 0.6).*

## 5.6 XRF data

The XRF data was provided at the courtesy of (Lantink et al., 2020 – in prep) and a more thorough description surrounding the methodology and relevant statistics is given in Appendix 5. Cyclostratigraphic analyses of these trends reveal a strong ~60-90 mm cyclicity (>95% confidence) for the elements K, Al, Ti, Mg, and Si (Appendix 6). This is of a similar length as the earlier described Knox Cyclothem, indicating that these elements follow the precession cycle. In interval J36c, the elements Mn, Fe, and Co do not reveal a ~60-90 mm cyclicity, indicating that these elements do no follow the precession cycle. Insoluble high-field strength (HFS) elements (e.g. Ti, Zr) as well as soluble large ion lithophile (LIL) elements (e.g. K and to a lesser extent Sr) and redox-sensitive elements (e.g. P and S) are all systematically enriched in *brown* biotite carbonate silicate mesobands. Furthermore, an increase in the Fe and Co concentrations coincides with the presence of both *black* microbanded oxide and oxide microbands, resulting in a somewhat noisy pattern. Finally, the Mn is interesting in the sense that it seems to partly follow the trend of Fe (e.g. both are depleted in *brown* biotite carbonate mesobands), while it also partly captures the variations in the Wt% Carbonate and the Sr record.

The core interval J57e also shows a strong cyclicity for many elements. Cyclostratigraphic analyses reveal a ~40-60 mm cyclicity (>95% confidence) in Ti, Al, K, Zr, Ca, Sr, and Si, which also reconciles with the earlier described Knox cyclothem and thus the precession cycle (Appendix 6). However, contrary to interval J36c, the elements Co, Fe, Mn and P also appear to follow this ~40-600mm cycle. Furthermore, the *brown* carbonate silicate and *green*

silicate mesobands are typically enriched in most of the HFS elements (e.g. K, Al), although the *green* silicate mesobands retain background values for some specific HFS elements that are clearly enriched in the *brown* carbonate silicate mesobands (e.g. Zr). The *white* carbonate mesobands in J57e are elevated in non-redox sensitive elements such as Sr, Ca, and Mg, but differ from J36c in the absence of a Mn peak. Also interesting is the S record, which is strongly and systematically enriched in the *white* carbonate mesobands in interval J57e as opposed to the *brown* carbonate silicate mesobands in interval J36c. Finally, we observed an interesting pattern in the Fe and Mn records; both show a strong out-of-sync zigzag pattern throughout interval J57e. The Fe concentration abruptly increases at the start of a *black* microbanded oxide, after which it steadily decreases throughout the Knox cyclothem, reaching a minimum value in the *beige* microbanded chert. In contrast, the Mn concentration follows an opposite trend; its concentration gradually increases from the *beige* microbanded chert upward, reaching its maximum value within the *brown* carbonate silicate mesoband. After this the Mn concentration abruptly drops through the *white* carbonate mesoband to reach its minimum value in the *beige* microbanded chert. The Mn-trend strongly resembles the zigzag pattern of the Wt% Carbonate in interval J57e.

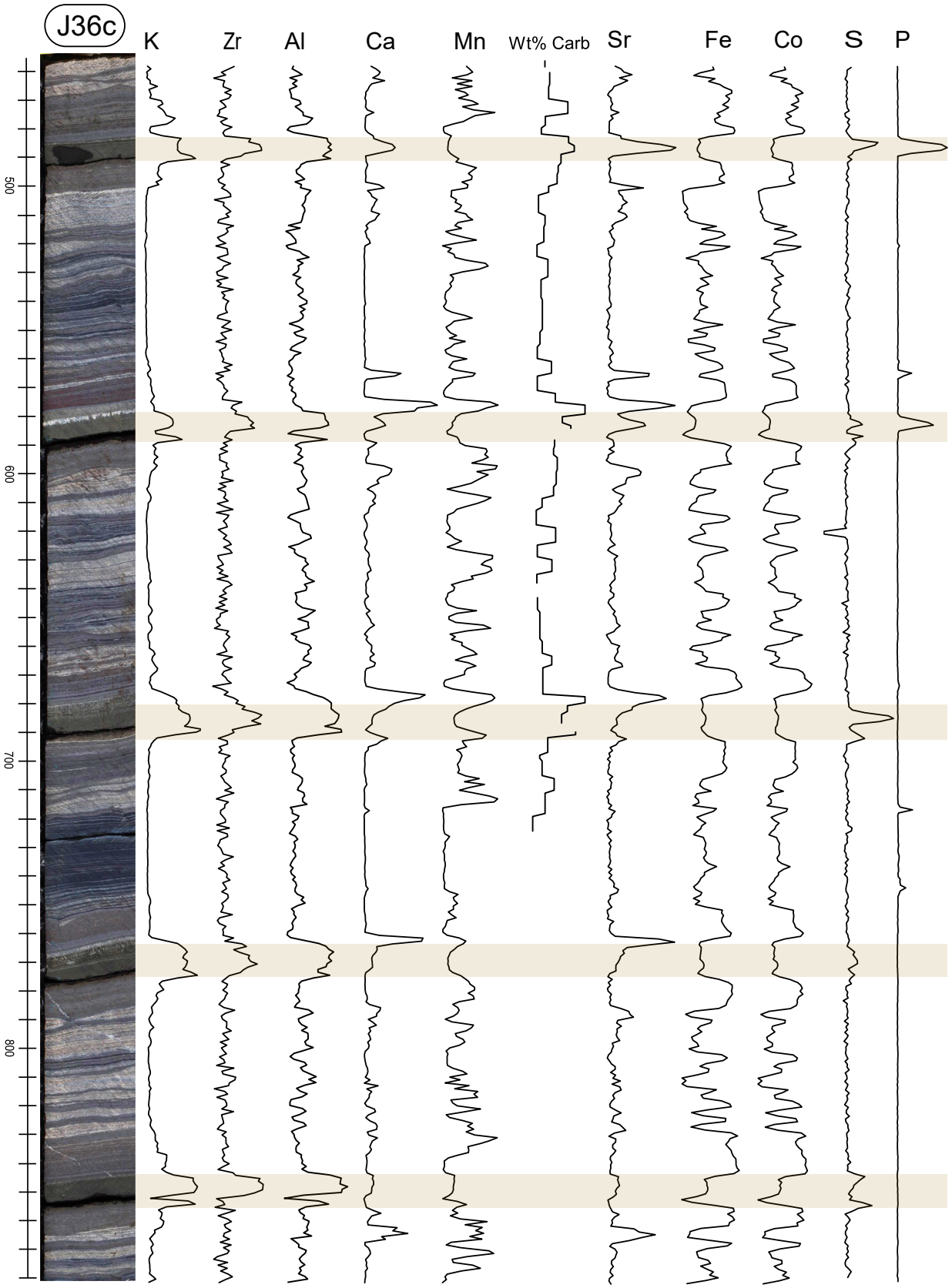


***Fig 14 –*** *The high-resolution XRF records for a variety of elements for interval J36c. Also included is the Wt% Carbonate (this study). Brown highlights coincide with the biotite carbonate silicate mesobands. Data was provided at the courtesy of (Lantink et al., 2020 – in preparation)*

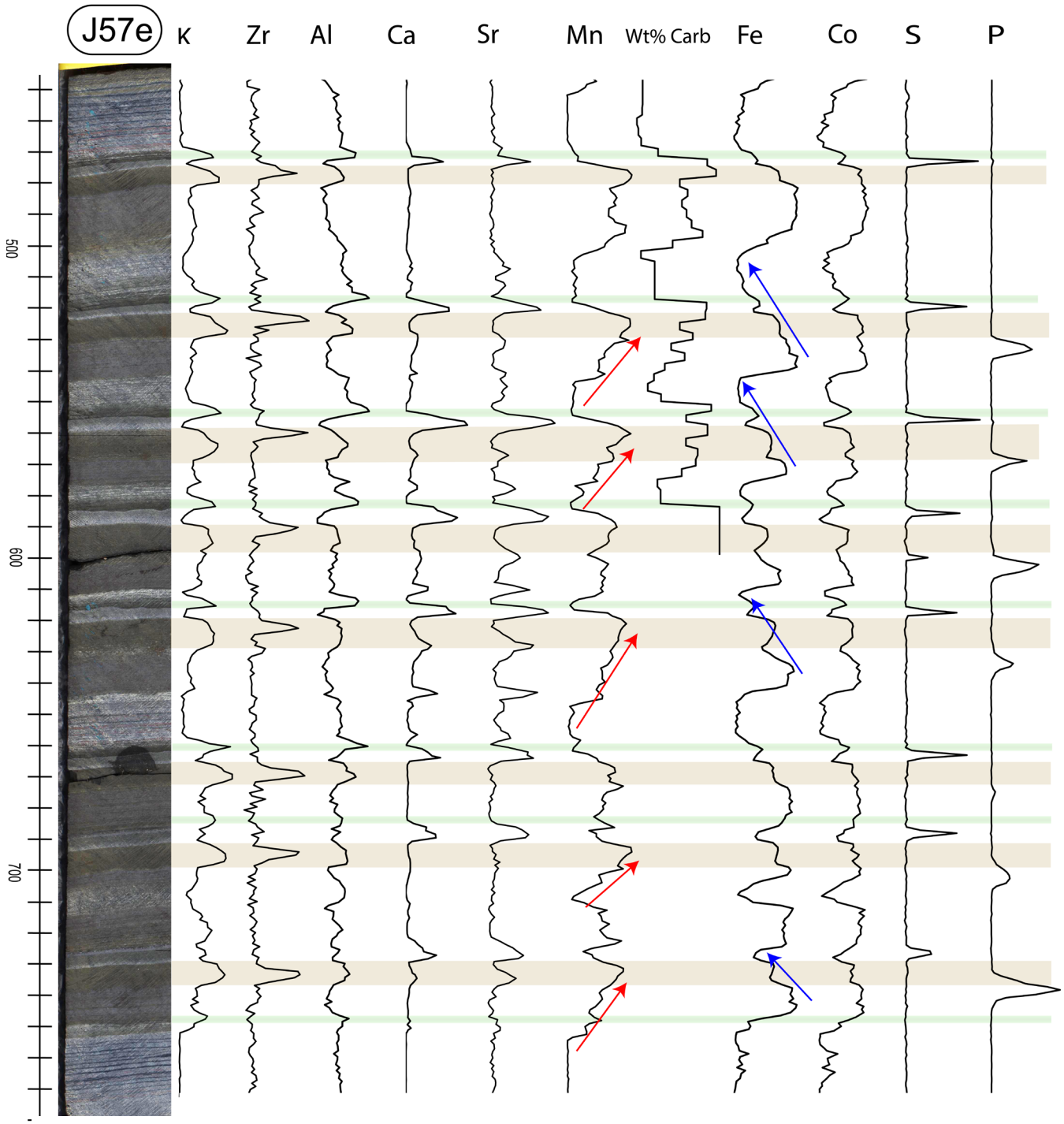


***Fig 15 –*** *The high-resolution XRF records of a variety of elements for interval J57e. Also included is the Wt% Carbonate (this study). Brown highlights coincide with the carbonate silicate mesobands and green highlights coincide with the silicate mesobands. Red arrows are indicative for the Mn trend, which gradually increases from the microbanded chert towards the carbonate silicate mesoband over approximately one Knox cyclothem. Blue arrows are indicative for the Fe trend, which gradually declines from the microbanded oxide towards the microbanded chert. Data was provided at the courtesy of (Lantink et al., 2020 – in preparation).*

Element vs element plots were used to investigate in what mineralogical phases certain elements were residing (all the plots are York fitted). The intervals differ mostly in terms of the Mn vs Fe plots, since J36c (Fig 16 – A) is devoid of any linear relation between these elements, whereas J57e (Fig 15 – B) shows a weak linear relation between Mn vs Fe ($R^2$ =0.50 with poor data spread). Consequently, Fe and Mn are not coupled in J36c and weakly coupled – if at all coupled – in J57e. In contrast, the Ca vs Sr (Fig 16 – C, D) and the K vs Ti (Fig 16 – E, F) display statistically relevant linear correlations that are similar for both intervals ($R^2$ > 0.80 and $R^2$ > 0.60 respectively). The strong linear relation between Ca vs Sr and Ti vs K indicates that these elements were chemically coupled.

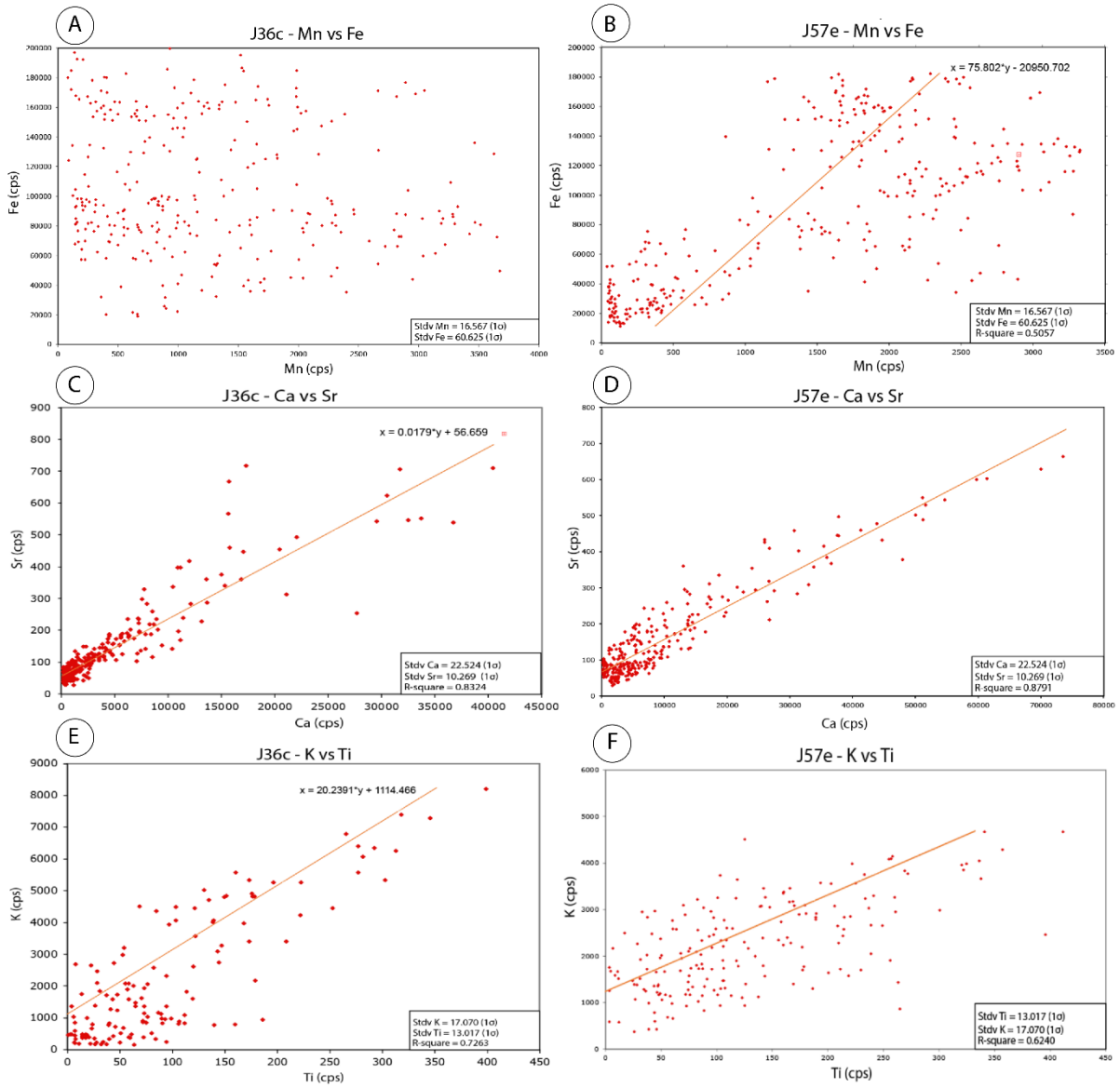


***Fig 16 –*** *Semi quantitative element vs element plots for interval J57e and J36c. Regression lines are York fitted. Standard deviations for the various elements are given in the lower right corner, along with the $R^2$ of the regression lines.* ***A)*** *Mn vs Fe in J36c are not coupled.* ***B)*** *Mn vs Fe in J57e appear weakly coupled, although the data spread is poor.* ***C)*** *Ca vs Sr in J36c are strongly coupled.* ***D)*** *Ca and Sr in J57e are strongly coupled.* ***D)*** *The K vs Ti in J36c are coupled, although the data spread is larger compared to the Ca vs Sr plot.* ***F)*** *The K vs Ti in J57e are coupled and have a wider data spread compared to the Ca vs Sr plot.*

Finally, the Fe/Co was interesting because of its contrasting expression in interval J36c and J57e. The ratio is extremely constant in interval J36c, remaining virtually unaffected by mineralogical distinct BIF facies (Fig 17 – red in A), whereas it strongly varies throughout the Knox Cyclothem in interval J57e (Fig 17 – blue in A). In J57e, the highest Fe/Co are found in the *shaly* oxide BIF facies, while the lowest Fe/Co ratios are found in the *shaly* chert BIF facies. The *shaly* carbonate BIF facies shows intermediate values of the Fe/Co ratio. The elements versus elements plot for Co and Fe for interval J36c shows a strong linear dependency between these two elements. The regression line intersects the origin, indicating that these elements were strongly coupled (Fig 17 – C). In contrast, the Co vs Fe elemental plot for interval J57e shows a much more complex relation between the data. Consequently, the data can either be fitted with two separate regression lines or with a parabolic curve.

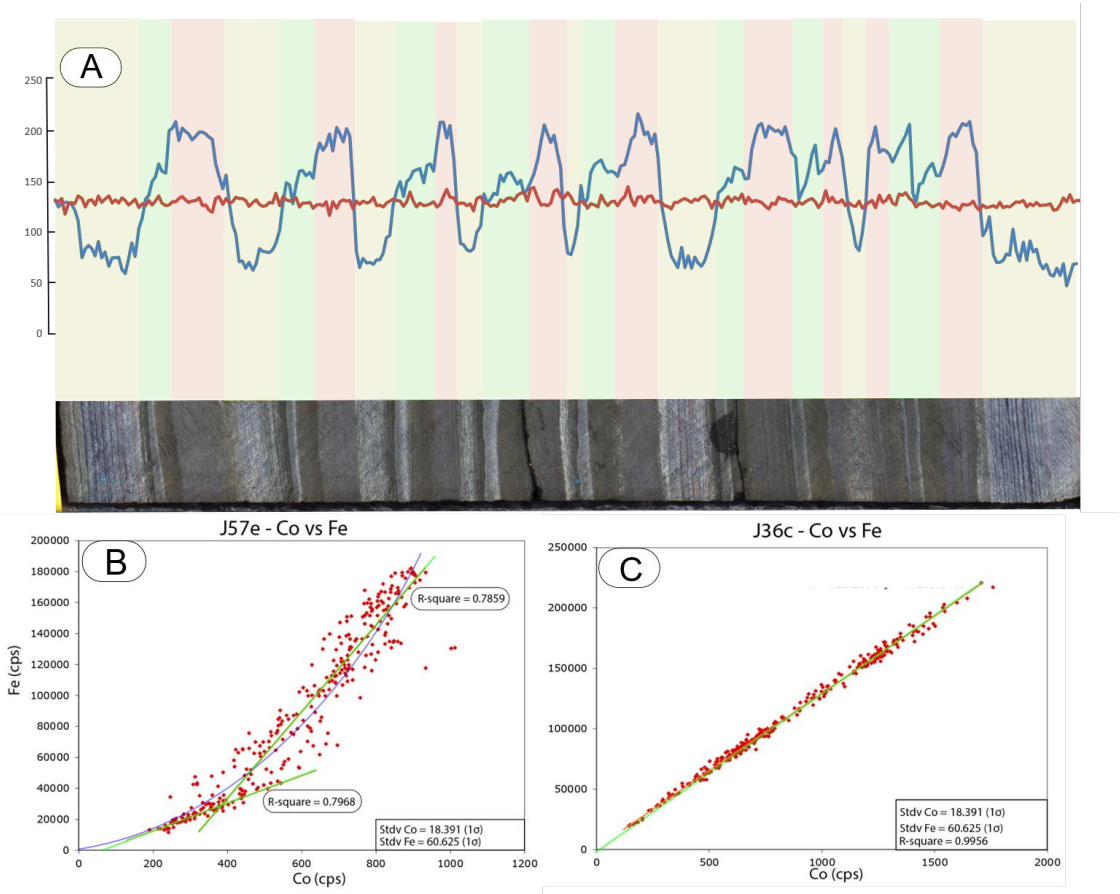


***Fig 17 – A)*** *Semiquantitative Fe/Co ratio for J36c (red) and J57e (blue) plotted against interval J57e. We did not plot the Fe/Co ratio against the length of J36c since the ratio remained constant irrespective of the BIF facies. Therefore, the Fe/Co ratio is unrelated to the displayed core interval in the figure and the highlighted BIF facies. In contrast, the Fe/Co ratio for interval J57e corresponds to the displayed core interval in the figure. The Fe/Co for interval J57e is lowest in the shaly chert BIF facies (highlighted in yellow) and highest in the shaly oxide BIF facies (highlighted in red). The shaly carbonate BIF facies (highlighted in green) of interval J57e have intermediate values that fall in between these two extremes.* ***B)*** *Co vs Fe in J57e can be fitted with two separate regression lines (green) or a parabolic curve (blue). Furthermore, the data spread is relatively large compared to interval J36c.* ***C)*** *Co and Fe are perfectly coupled in J36c as suggested form the regression line.*

# 6 Discussion

## 6.1 Did the original organic carbon flux vary over the Knox cyclothem?

### 6.1.1 Evidence for early diagenetic redox cycling in the BIF sediments

It is important to find evidence that supports a diagenetic reworking of the BIF sediment before evaluating if the organic carbon flux varied over the Knox cyclothem. This is because early diagenetic redox cycling in BIFs has not been universally accepted, which on its turn reflects the issue that BIF minerals could have precipitated directly from the ocean water column and/or were formed during the onset of metamorphism (Tosca et al., 2019; Kaufman et al., 1990; Li et al., 2013a). This is why we first discuss the petrographic and isotopic evidence that supports an early diagenetic reworking of the sediments. We argue that the carbonates are an important mineral that could help to solve this problem. We observed two important types of carbonates in our thin sections. These were the (sub)spherical carbonate of the *brown* (biotite) carbonate silicate mesobands and the *black* microbanded oxide and the coarse carbonates of the *brown* (biotite) carbonate silicate mesoband, the *white* (hematite) carbonate mesoband, and the *beige* microbanded chert. Firstly, our petrographic observations indicate that the (sub)spherical carbonate have morphologies that cannot be explained by a metamorphic reworking of the sediment. Recent experimental studies that evaluated the equilibrium precipitation of siderite from ocean water showed similar morphological features and crystal sizes with respect to the carbonate that we encounter in the *brown* (biotite) carbonate silicate mesobands (Jiang and Tosca, 2019). This is complemented by deep marine sediments recovered from the Guatemala basin in the Pacific Ocean which demonstrated that early diagenetic carbonates (e.g. rhodochrosite) had similar morphologies to our (sub)spherical carbonates (Kuleshov & Maynard, 2017). Furthermore, the (sub)spherical carbonate pre-dated the formation of stylolites, which consequently suggests that a large part of the (sub)spherical carbonates were already present in the BIF sediment prior to sediment compaction and did not form during metamorphism. In contrast, our petrographic observations and isotope data suggested that the coarse carbonates post-dated the formation of the stylolites and formed as a result of continuous diagenetic recrystallization of the (sub)spherical carbonates.
This interpretation is supported by 1) the presence of recrystallization fronts (i.e. bulge and lobe textures) in the *white* hematite carbonate mesobands. 2) The observation that the coarse carbonates envelop the stylolite-like features, which hint at a stress-induced dissolution-precipitation reaction of the (sub)spherical carbonates during sediment compaction. 3) The presence of a sharp and discontinuous contact that characterizes the top of the *white* carbonate mesobands and which also supports diagenetic dissolution reactions during sediment compaction. 4) The presence of relict (sub)spherical carbonate cores in larger coarse carbonate crystals, which suggests that the coarse carbonate grew at the expense of the (sub)spherical carbonate. 5) The presence of numerous inclusions of chert, stilpnomelane needles, and *dusty* hematite/Fe-silicates in the cores of some of the coarse carbonate crystals. 5) The XRF data that shows that the *white* (hematite) carbonate mesobands are systematically enriched in Ca, Mg and Sr. Possibly, Ca, Mg and Sr were mobilized during diagenetic recrystallization and preferably incorporated into the coarse carbonates, which explains why Ca and Sr are so strongly coupled and why the Ca, Mg and Sr are systematically elevated in the mesobands that show the strongest textural evidence for recrystallization. And 6) the combined $\delta^{13}C_{carb}$ and $\delta^{18}O_{carb}$ isotope data that suggests that the coarse carbonates were exposed to diagenetic recrystallization, dolomitization and/or thermal dissolution-reprecipitation reactions (red arrow in Fig 20). These reactions typically result in a loss of $\delta^{18}O_{carb}$ while not affecting the $\delta^{13}C_{carb}$ signature (Veizer 1989; Veizer 1989; Veizer 1990), which explains why the coarse

carbonates (e.g. the coarse carbonates of the *beige* microbanded chert) show a wide range of $\delta^{18}O_{carb}$ signatures. The relation between the coarse carbonates and the stylolites suggest that the recrystallization of the carbonates took place during sediment compaction. Furthermore, our petrographic observations clearly suggest that the coarse carbonates pre-dated the growth of late-diagenetic to metamorphic riebeckite and euhedral magnetite. Therefore, we argue that the coarse carbonates are not related to metamorphism either and formed during the diagenetic reworking of the sediment.

Although the carbonates in our BIF intervals were evidently not metamorphic, this does not clarify if the (sub)spherical carbonates precipitated directly from the ocean water column or if they formed during early diagenesis as precipitates from the interstitial pore-water. Our petrographic observations combined with our isotope analyses suggest that the (sub)spherical carbonates precipitated *mostly* from interstitial pore-water during early diagenesis. This is because: 1) the *brown* (biotite) carbonate silicate mesobands are characterized by an absence of internal microbanding, which suggests a dynamic diagenetic reworking of the sediment that disturbed the original sedimentary features. 2) Most of the (sub)spherical carbonates contain numerous inclusions of *dusty* hematite/Fe-silicates and stilpnomelane needles. The *dusty* hematite/Fe-silicates inclusions could have been incorporated within the carbonate crystals as nano-crystalline particles, which could have occurred both in the water column and during sedimentary reworking. In contrast, the silpnomelane needles were unlikely to have precipitated directly from the water column because of their distinctive crystal habit and relatively large crystal size. Rather, the stilpnomelane needles may have provided in-situ nucleation sites on which diagenetic carbonate could precipitate from interstitial porewater fluids. However, an alternative to this is that the stilpnomelane needles grew at the expense of the *dusty* Fe-silicates (e.g. greenalite, clay) within carbonate crystals, which should be further tested through high-resolution petrographic work. 3) The (sub)spherical carbonates that we encountered in the *black* microbanded oxide are texturally related to skeletal hematite aggregates and point toward a reaction in which hematite (or its precursor) were consumed and siderite and/or quartz were produced. Finally, 4) the highly depleted $\delta^{13}C_{carb}$ (< -5.7 ‰) and $\delta^{18}O_{carb}$ (<20.5‰) values of the carbonates in our interval differ substantially from that of shallow-water Archean limestones and dolomites that precipitated in direct chemical equilibrium of the ocean water (Veizer et al., 1989). These different isotope signatures cannot be explained by a contrasting fractionation factor between calcite and siderite/ankerite during recrystallization ($\Delta^{13}C_{carb} < 1$ ‰) nor by equilibrium precipitation of siderite from isotopically homogenous ocean, which would carry a signature of $\delta^{13}C_{carb} \approx 0$‰ and $\delta^{18}O_{carb} \approx 25$‰ (Heimann et al., 2010). Therefore, we argue that the highly depleted $\delta^{13}C_{carb}$ and $\delta^{18}O_{carb}$ signatures of the BIF carbonates point toward a predominant diagenetic origin of the BIF carbonates. However, some of the (sub)spherical carbonates appeared exceptionally rounded and had cores of *dusty* hematite/Fe-silicates, which could be compatible with a direct precipitation from the ocean water column. This is why it is still possibly that a small percentage of the carbonates precipitated from direct equilibrium of the ocean water column as well (see section see section of why the organic matter fluctuated over the Knox cyclothem). Overall, the combined petrographic and isotopic evidence favors a scenario in which most (sub)spherical carbonates precipitated in-situ from interstitial pore-water during the diagenetic reworking of the original BIF sediment. Therefore, we agree with (Lantink et al., 2019 – in prep) in the sense that Joffre was exposed to early diagenetic redox cycling. Such diagenetic redox cycling asserted a strong influence on the mineralogical textures and isotope signatures of the carbonates in the BIF sediment and hence on the expression of the Knox cyclothem.

### 6.1.2 What was the role of organic matter during diagenetic redox cycling in BIF?

The low concentration of Wt% $C_{org}$ (~0.02 Wt%) that we measured in both BIF intervals with respect to time equivalent Archean rocks suggests that the organic carbon was removed or remineralized within the BIF sediment or was not deposited in the first place. It is well-known that organic matter acts as an important electron donor during diagenetic redox cycling in modern environments. Therefore, the organic matter in BIF may have driven redox cycling during which the BIF intervals experienced a near-quantitative loss of the original organic matter that was deposited alongside the ferrihydrite in the pre-diagenetic BIF sediment.

We argue that both the C/N ratio and carbonate isotope chemistry provide strong evidence that the degradation of organic matter was indeed happening during the diagenetic reworking of the BIF sediment. Firstly, the average C/N ratio of J36c is 5.1, which is close to the Redfield ratio of 6.6 (Raven, 2013). This in itself is unusual since it suggests a minimal degradation of the organic matter that was deposited in BIFs, while it is well-known that the Hamersley basin experienced significant metamorphic reworking. Microbial degradation of organic matter and especially metamorphically induced carbonization reactions typically result in preferred loss of nitrogen with respect to organic carbon, which results in elevated C/N ratios, a feature seen in many of the time equivalent sediments of the Hamersley basin (Busigny et al., 2013). One straightforward explanation for the low C/N ratio is through the absorption of organic carbon onto clay particles in the water column. It has been shown that such surface bound carbon is extremely resistant to microbial and thermal alteration for up to millions of years and is therefore characterized by low C/N ratios (Estes et al., 2019). However, this surface bound carbon still needed to survive the conversion of the initial clay particles to stilpnomelane (i.e. the dominant phyllosilicate that we encountered in our intervals) without being affected by this process itself, which seem rather unlikely. Furthermore, it was recently shown that most organic carbon in BIFs is associated with apatite and carbonates and not with Fe-silicate/clay particles (Dodd et al., 2020).

An alternative interpretation may therefore be that diagenetic and/or metamorphic reduction of the organic carbon resulted in an increased $NH_4^+$ concentration in the pore-fluids, which was subsequently incorporated within the crystal lattice of clay minerals. Importantly, $NH_4^+$ is more tightly bound within the clay lattice as opposed to adsorbed organic carbon, which would make the $NH_4^+$ much more resistant to a conversion of clay to stilpnomelane and to subsequent metamorphism. Importantly, this would mean that the C/N ratio was not an original signature reflecting the primary origin of the organic material, but rather a diagenetic relict that reflected the degradation of organic matter in the presence of clay minerals. Supporting evidence for this interpretation comes from the Al vs N plot (Fig 18), which shows a strong correlation between these elements, implying that the bulk of the nitrogen resided as $NH_4^+$ in Fe-silicates (Fig 20). Interestingly, this evidence is much weaker for the Al vs $C_{org}$ plot (Fig 18), which fits with the idea that surface bound organic material was not the major phase in which nitrogen resided.

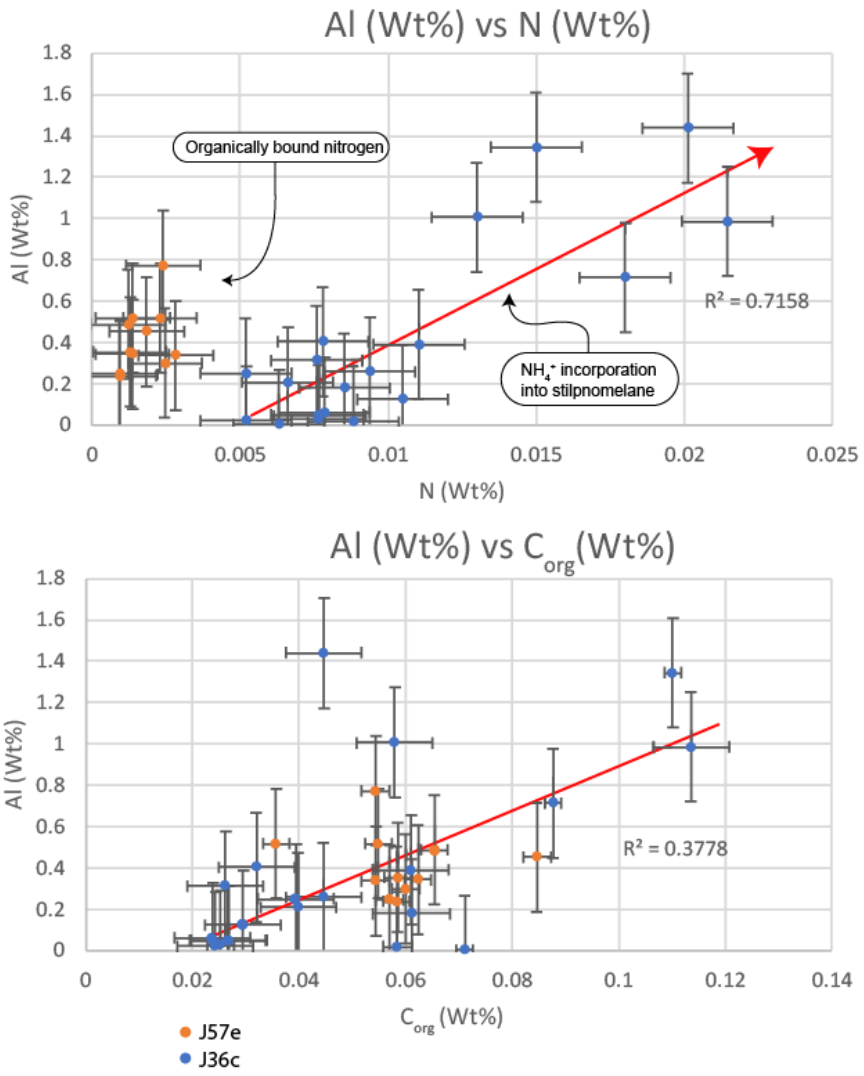


***Fig 18 –*** *The Al vs N elemental plot for interval J36c (blue) and interval J57e (orange) and the Al vs $C_{org}$ elemental plot for interval J36c (blue) and interval J57e (orange). The data of interval J36c shows a statistical relevant correlation between Al and N ($R^2$ = 0.7158), which suggests that most nitrogen resided in stilpnomelane as $NH_4^+$. Since the regression line does not go through the origin, it is unlikely that all nitrogen resided in phyllosilicates and a small amount of nitrogen was likely still associated with the matured organic carbon. The data of interval J57e do not show a similar correlation between Al and N. The Al vs $C_{org}$ show a statistically weak correlation for the data of J36c and J57, which implies that little or none of the organic carbon was surface bound.*

We further argue that the correlation between the $\delta^{13}C_{carb}$ signature and the Wt% $C_{org}$ of interval J57e is consistent with a diagenetic remineralization of organic matter as well and thus with the degradation of organic carbon (Fig 19). This is because an increase in the loss of organic matter coincides with a more pronounced diagenetic imprint on the carbonate isotope record, which implies that organic matter influenced the precipitation of the diagenetic carbonates. The diagenetic production of carbonates was most likely facilitated through dissimilatory iron reduction (DIR) in the absence of oxygen, nitrite/nitrate, and Mn-oxides. The metabolic pathway of DIR couples the oxidation of organic matter to the reduction of ferrihydrites (or other Fe-oxide phases). Experimental work has demonstrated that siderite characterized by highly depleted $\delta^{13}C_{carb}$ signatures and complementary diagenetic magnetite could be produced through DIR (Halama et al., 2016; Reddy et al., 2016; Posth et al., 2013; Schad et al., 2019). There are several DIR-related reaction pathways that could explain the wide range of $\delta^{18}O_{carb}$ and $\delta^{13}C_{carb}$ signatures that we found in our BIF samples:

1) $4Fe(OH)_3 + [CH_2O] + 3HCO_3^- \rightarrow 4FeCO_3 + 3OH^- + 7H_2O$

2) $4Fe(OH)_3 + [CH_2O] + 2HCO_3^- \rightarrow 3FeCO_3 + Fe^{2+} + 4OH^- + 6H_2O$

3) $4Fe(OH)_3 + [CH_2O] + HCO_3^- \rightarrow 2FeCO_3 + 2Fe^{2+} + 5OH^- + 5H_2O$

4) $4Fe(OH)_3 + [CH_2O] \rightarrow FeCO_3 + 3Fe^{2+} + 6OH^- + 4H_2O$

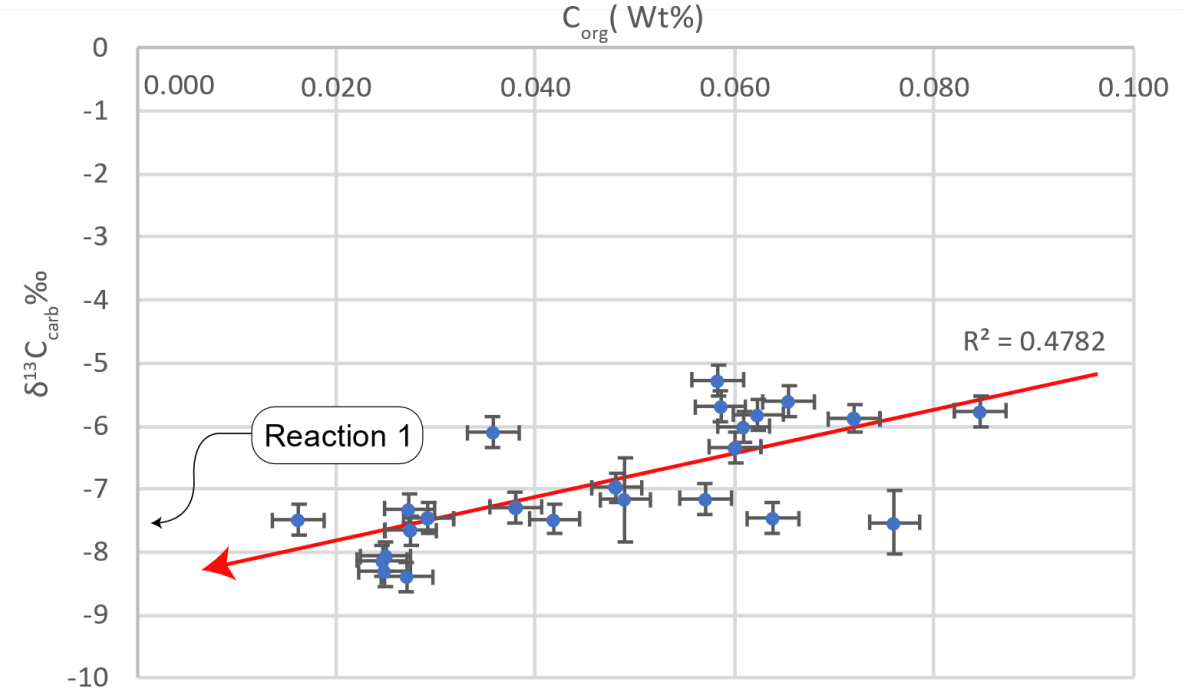


***Fig 19 –*** *The decrease of organic carbon in interval J57e is accompanied with a decrease in the $\delta^{13}C_{carb}$ signature. This relation suggests that the remineralization of organic carbon directly influenced the isotope composition of the carbonates. In the case of a near quantitative oxidation of the $C_{org}$, the reaction would generate carbonates with signatures of -7.5‰ to -8.5‰. This fits with the theoretically predicted signatures of reaction 1.*

As noted by (Heiman et al., 2010) these reactions can explain the millimeter-scale variation of $\delta^{18}O_{carb}$ and $\delta^{13}C_{carb}$ signatures if it is assumed that the $[CH_2O]$ source had a relative constant $\delta^{13}C_{org}$ signature of -28 to -29‰ and a relatively constant $\delta^{18}O_{org}$ signature of ~ -1‰. Furthermore, the $4Fe(OH)_3$ should have had a relatively constant $\delta^{18}O_{org}$ signature of ~ -2‰ and finally the $HCO_3^-$ source should have had a relatively constant $\delta^{13}C_{DIC}$ signature of 0‰ and a relatively constant $\delta^{18}O_{DIC}$ signature of ~26-29‰ (although the exact $\delta^{18}O$ signature of the Archean ocean is still debated). Consequently, it is the contribution of bicarbonate generated through the oxidation of organic matter versus the assimilation of bicarbonate from the ocean water column that determined the final isotope composition of the siderite (Table 2). This is what we see in our results; interval J36c is characterized by significantly more depleted $\delta^{13}C_{carb}$ and $\delta^{18}O_{carb}$ signatures as opposed to interval J57e, which becomes even more apparent if additional data of *classic* BIF samples from the Dales Gorge member are considered (Fig 20) (de Vries, 2019 – BSc thesis). Most of the carbonates in the *classic* chert BIF facies of J36c have signatures that tightly cluster in the field of $\delta^{13}C_{carb} \approx$ -10 ‰ and $\delta^{18}O_{carb} \approx$ 19.5‰, which is exactly the value predicted by reaction 2. The carbonates of the *classic* oxide BIF facies of J36c have signatures

that extend all the way down to $\delta^{13}C_{carb}$ ≈ -15‰ and $\delta^{18}O_{carb}$ ≈ 18.5 to 19.5‰, which supports a mixture of carbonates derived from reaction 2 and reaction 3. In contrast, most of the carbonates in the *shaly* oxide BIF facies of J57e have signatures that cluster in the field of $\delta^{13}C_{carb}$ ≈ -7.5 ‰ and $\delta^{18}O_{carb}$ ≈ 20.5‰, which is exactly the value predicted by reaction 1. The carbonates in the *shaly* chert BIF facies of J57e have similar $\delta^{13}C_{carb}$ signatures but a wider spread in the $\delta^{18}O_{carb}$ signatures which we attributed to diagenetic recrystallization of the subspherical carbonates (see first part discussion). However, these carbonates were likely still generated via reaction 1. Finally, the carbonates that were derived from the *shaly* carbonate facies BIF have $\delta^{18}O_{carb}$ signatures that are compatible with reaction 1. However, the $\delta^{13}C_{carb}$ are heavier than -7.5 ‰, which requires an additional explanation (see section of why the organic matter fluctuated over the Knox cyclothem). The theoretically predicted $\delta^{18}O_{carb}$ and $\delta^{13}C_{carb}$ signatures of the different DIR reactions are indicated with labelled black arrows in Fig 20. Overall, the C/N ratios and the $\delta^{13}C_{carb}$ vs Wt% $C_{org}$ correlation provide strong evidence for a degradation of the organic material in BIFs, while the $^{18}O_{carb}$ and $\delta^{13}C_{carb}$ isotope signatures suggest that DIR was an important mechanism that facilitated the degradation of the organic material by coupling the oxidation of organic matter to the reduction of ferrihydrite. Consequently, this metabolic pathway generated most of the BIF carbonates during early diagenetic redox cycling in the BIF sediment.

| | | | | | | | |
|---|---|---|---|---|---|---|---|
| **Equation 1** | $\mathbf{4Fe(OH)_3}$ | $\mathbf{+ CH_2O}$ | $\mathbf{+ 3HCO_3^- \rightarrow}$ | $\mathbf{+ 4FeCO_3}$ | $\mathbf{+ 3OH^-}$ | $\mathbf{+ 7H_2O}$ | |
| $\delta^{13}C$ (‰) | | *-28.5* | *0* | *-7.1* | | | |
| $\delta^{18}O$ (‰) | *-2* | *-1* | *27* | *20.6* | | *-6.5* | |
| **Equation 2** | $\mathbf{4Fe(OH)_3}$ | $\mathbf{+ CH_2O}$ | $\mathbf{+ 2HCO_3^- \rightarrow}$ | $\mathbf{+ 3FeCO_3}$ | $\mathbf{+ 4OH^-}$ | $\mathbf{+ 6H_2O}$ | $\mathbf{+ Fe^{2+}}$ |
| $\delta^{13}C$ (‰) | | *-28.5* | *0* | *-9.5* | | | |
| $\delta^{18}O$ (‰) | *-2* | *-1* | *27* | *19.5* | | *-7.5* | |
| **Equation 3** | $\mathbf{4Fe(OH)_3}$ | $\mathbf{+ CH_2O}$ | $\mathbf{+ HCO_3^- \rightarrow}$ | $\mathbf{+ 2FeCO_3}$ | $\mathbf{+ 5OH^-}$ | $\mathbf{+ 5H_2O}$ | $\mathbf{+ 2Fe^{2+}}$ |
| $\delta^{13}C$ (‰) | | *-28.5* | *0* | *-14.3* | | | |
| $\delta^{18}O$ (‰) | *-2* | *-1* | *27* | *18.1* | | *-8.9* | |
| **Equation 4** | $\mathbf{4Fe(OH)_3}$ | $\mathbf{+ CH_2O}$ | $\mathbf{\rightarrow}$ | $\mathbf{+ FeCO_3}$ | $\mathbf{+ 6OH^-}$ | $\mathbf{+ 4H_2O}$ | $\mathbf{+ 3Fe^{2+}}$ |
| $\delta^{13}C$ (‰) | | *-28.5* | *0* | *-28.5* | | | |
| $\delta^{18}O$ (‰) | *-2* | *-1* | *27* | *16.1* | | *-10.9* | |

***Table 2 –*** *The isotope signatures that are associated with the different DIR reactions depending on the contribution of bicarbonate relative to that of organic matter. We assumed an $[CH_2O]$ of -28.5 ‰ based on the average isotope composition of the analysed organic carbon. The rest of the assumptions are based on the work of (Heiman et al., 2010).*

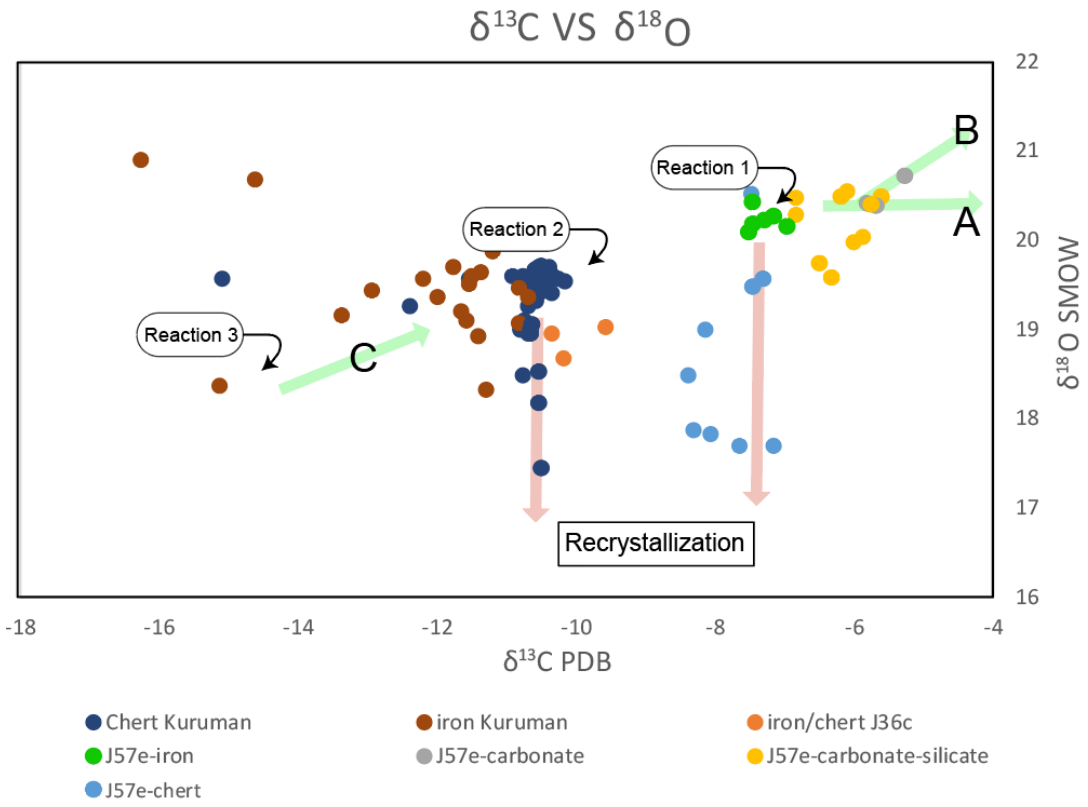


***Fig 20** – $\delta^{13}C_{carb}$ and $\delta^{18}O_{carb}$ signatures of shaly BIF (right side) and classic BIF (left side). Theoretical predicted isotope signatures of the carbonates that were generated through DIR are indicated by reaction textboxes and associated arrows (reactions provided in text). Arrow **A** is compatible with DIR related carbonates that intermixed with dolomites and calcite that precipitated in direct equilibrium with the ocean water column. Arrow **B** is compatible with DIR related carbonates that intermixed with siderite that precipitated in equilibrium with the ocean water column. Finally, arrow **C** is compatible with the intermixing of two DIR related carbonate reservoirs. The chert BIF facies show a large spread in the $\delta^{18}O_{carb}$ signatures but a relatively confined spread in the $\delta^{13}C_{carb}$ signatures. We argue that this is compatible with diagenetic recrystallization. Additional data provided at the courtesy of (de Vries, 2019 – BSc thesis).*

### 6.1.3 How did the organic carbon fluctuate over the Knox cyclothem?

Since the organic-poor mesobands (i.e. the mesobands found in the oxide BIF facies and chert BIF facies) have very low $C_{org}$ contents, we argue that the organic carbon was near quantitatively removed through DIR in the presence of ferrihydrite. In contrast, the carbonate BIF facies show a higher Wt% $C_{org}$ that could reflect an availability of organic matter that (slightly) outweighed the availability of ferrihydrite. Consequently, the ferrihydrite was quantitively removed, but the organic carbon was not. This highlights the possibility that the original organic carbon in the pre-diagenetic BIF sediment fluctuated on a precession-scale and resulted either in a near-quantitative removal the ferrihydrite or of the organic matter in the sediment pile. This interpretation is supported by combined $\delta^{13}C_{org}$ signatures, petrographic observations, and mass-balancing of the original organic carbon in the pre-diagenetic BIF sediment. Firstly, we found fluctuations in the $\delta^{13}C_{org}$ record which corresponded to mineralogically distinct facies and mesobands. The absence of extremely depleted $\delta^{13}C_{org}$ signatures (> -35 ‰) argues against a dominant role of methanotrophy during BIF deposition (Eigenbrode and Freeman, 2006; Czaja et al., 2010). However, this does not mean that methanogenesis and/or methanotrophy was completely absent during BIF deposition; the systematic depletion of $\delta^{13}C_{org}$ in the *white* (hematite) carbonate mesobands could indicate minimal assimilation of highly $^{13}C$ depleted $CH_4$ by methanotrophs that was

intermixed with a dominant source of organic matter derived from autotrophic organisms. Binary mixing models proposed by (Brocks et al., 2003) showed that small contributions of kerogens derived from methanotrophs (~20%) to isotopically heavier *n*-alkanes and lipids derived from pre-dominantly autotrophic organisms (e.g. cyanobacteria) could already result in a combined $\delta^{13}C_{org}$ signature of ~ -35‰, which closely matches the observed $\delta^{13}C_{org}$ signatures of ~ -30‰ in our *white* (hematite) carbonate mesobands. The production of $CH_4$ could have been facilitated by methanogens under anaerobic conditions through the oxidation of $H_2$, acetate, and formate (Konhauser et al., 2005). Alternatively, $CH_4$ could have been produced through the thermogenic decomposition of residual organic matter (Ueno et al., 2006). However, in both cases the initial ferrihydrite in the sediment must have been quantitatively reduced, since ferrihydrite strongly inhibits the activity of methanogenesis and methanotrophy (Achtnich et al., 1995). This is confirmed by our petrographic observations, which indicate that the mesobands that contained the highest amount of Wt% $C_{org}$ also contained negligible amounts of hematite.

Additional evidence for the onset of multiple metabolic pathways in the carbon-rich mesobands comes from the pyrite in the *white* carbonate mesobands of J57e. This could have been formed as byproduct of sulphate reduction coupled to anaerobic methanotrophy, in which case $CH_4$ would have acted as an electron acceptor (Weber et al., 2016). This reaction pathway also explains why the imprint of methanotrophy was small rather than large, since sulphate was likely scarce in the Archean ocean and may have asserted a biolimiting role on this metabolic pathway. However, there are three additional processes that could explain the formation of this pyrite as well: 1) sulphate reduction in the water column unrelated to $CH_4$ respiration, 2) the remineralization of organically bound sulfur within the sediment pile, or 3) a delivery of detrital pyrite from the continents. Although there is little previous work on pyrite in BIFs, some studies suggest that microbial sulphate reduction occurred during the deposition of the Mount McRae Shale which stratigraphically underlies the Joffre Member (Posth et al., 2013; Patridge et al., 2008; Thode & Goodwin, 1983). This could be compatible with sulphate being used as electron donor for $CH_4$ respiration during the diagenetic reworking of the sediment. In contrast, the $\delta^{13}C_{org}$ signature of the organic matter in the *shaly* oxide BIF facies is systematically heavier than that of the other mesobands ($\delta^{13}C_{org} \approx$ -27‰), which could mean that methanogenesis and sulphate reduction were inhibited by the presence of abundant Fe(III) minerals. This resulted in a larger contribution to the original organic carbon from autotrophic and/or DIR-related biomass. Consequently, the *shaly* oxide BIF facies was characterized by a relatively heavier $\delta^{13}C_{org}$ signature and an absence of sulfur isotope fractionation in pyrites (Thode & Goodwin, 1983).

However, we would also like to point out that the variations in the $\delta^{13}C_{org}$ between the mesobands and mineralogically distinct BIF facies are small and that the organic matter of even a single respirational process (e.g. autotrophic photosynthesis) already comprises a mixture of numerous compounds that are all characterized by a wide range of $\delta^{13}C_{org}$ signatures (Brocks et al., 2003). Changes in the relative preservation and degradation of some of these compounds could therefore also result in the observed variance of the $\delta^{13}C_{org}$ signature, without invoking multiple microbial respiration pathways and changes in the redox potential of the sediment. Alternatively, phototrophic organisms may utilize a wide variety of carbon fixation pathways that all result in slightly different but overlapping $\delta^{13}C_{org}$ signatures, which could mean that the observed $\delta^{13}C_{org}$ signature simply reflected changes in the biogenic carbon uptake during photosynthesis. Therefore, our interpretation for the onset of different metabolic pathways depending on the changes in the original organic carbon is compatible with the isotope and petrographic data, but does not provide the only explanation for the variance in the $\delta^{13}C_{org}$ signature. Additional research is needed to confirm that multiple respirational pathways

were utilized during diagenetic redox cycling, for example through detailed analyzes of the $\delta^{13}C$ signature of the *n*-alkanes, kerogen, and cyclic isoprenoids that make up the bulk of the organic matter.

Since the carbonates were generated by the remineralization of organic matter through DIR, a part of the carbonates must contain carbon atoms that were derived from the original carbon in the sediments. Therefore, we argue that mass-balancing of the carbonates through combined $\delta^{13}C_{carb}$ and $\delta^{18}O_{carb}$ signatures and the Wt% Carbonate (calculated through the EA-IRMS) is a useful tool to determine the original organic carbon in the pre-diagenetic BIF sediment varied on the precession-cycle. We did this for a single Knox cyclothem for both intervals. It should be noted that the mass-balancing resulted in a minimum estimate of the initial organic carbonate. This is because 1) partial dissolution and recrystallization of the carbonates may have facilitated a loss of organically derived $CO_2$ from the system, which is a common feature seen in modern environments (Boudreau et al., 1987). And 2) a considerable amount of late magnetite could have been formed through the thermal breakdown of siderite and/or a metamorphic reaction between residual hematite and siderite. These reactions would result in a loss of isotopically light $CO_2$ that was originally incorporated into the carbonates, thereby leading to an underestimation of the Wt% $C_{org\ initial}$. The details considering the mass-balancing procedure are given in Appendix 7.

The Knox cyclothem in interval J57e shows a gradual increase of Wt% $C_{org\ initial}$ over the Knox cyclothem that has a similar pattern to the Wt% Carbonate (Fig 21). Within the Knox cyclothem itself, the *shaly* chert BIF facies shows the relatively lowest Wt% $C_{org\ initial}$, whereas the *shaly* carbonate BIF facies show the relatively highest Wt% $C_{org\ initial}$. This suggests that the *shaly* chert BIF facies experienced less intense diagenetic reworking through DIR as opposed to the *shaly* carbonate BIF facies. The Knox cyclothem in interval J36c shows an abrupt increase in the original Wt% $C_{org\ initial}$ that coincides with the *white* hematite carbonate mesoband, whereas the rest of the mesobands and BIF facies show a relatively low Wt% $C_{org\ initial}$ (Fig 22). Since we were not able to measure the isotope signatures of the *classic* carbonate BIF facies, we utilized two different methods to calculate the Wt% $C_{org\ initial}$ in the mass balancing model (Appendix 7). These different methods result in slightly different estimates of the Wt% $C_{org\ initial}$. However, in both cases the Wt% $C_{org\ initial}$ is still strongly elevated over the other mesobands and mineralogically distinct BIF facies. This suggests that the *white* hematite carbonate mesobands and thus the *classic* carbonate BIF facies of interval J36c were exposed to more intense diagenetic reworking through DIR as opposed to the other BIF facies.

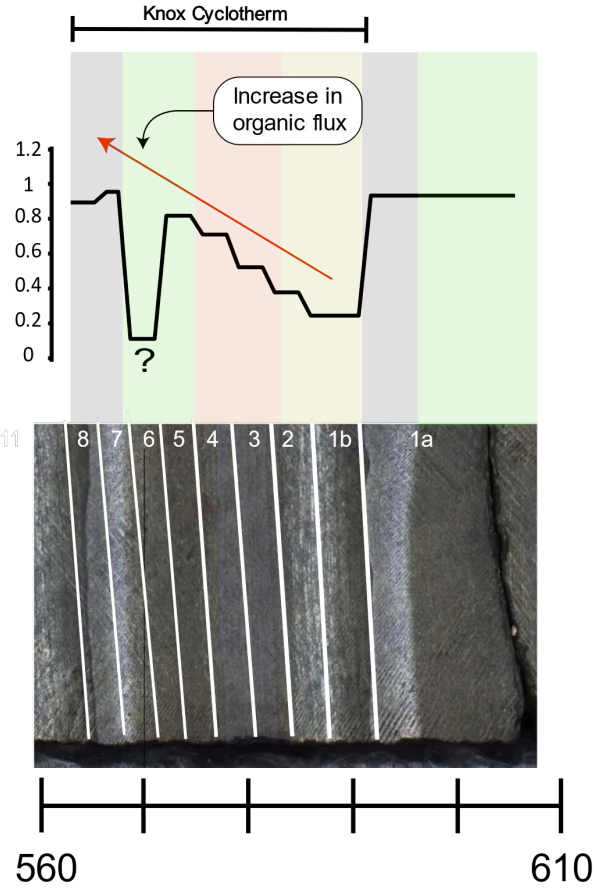


***Fig 21 –*** *Mass balancing model of the Wt% $C_{org\ initial}$ as calculated from the stable carbonate isotopes data and the EA-IRMS data. Different mesobands are highlighted in green (carbonate silicate mesoband), grey (carbonate mesoband), yellow (microbanded chert), and red (microbanded oxide). Also included are the positions of the sample slices. The organic carbon flux increases systematically over the Knox cyclothem (red arrow) and reaches is maximum value in the carbonate mesoband. We were not sure if the slice with the question mark was an outlier or a real diagenetic feature. Finally note that the calculated Wt% $C_{org\ initial}$ is a minimum estimate and may have higher in reality.*

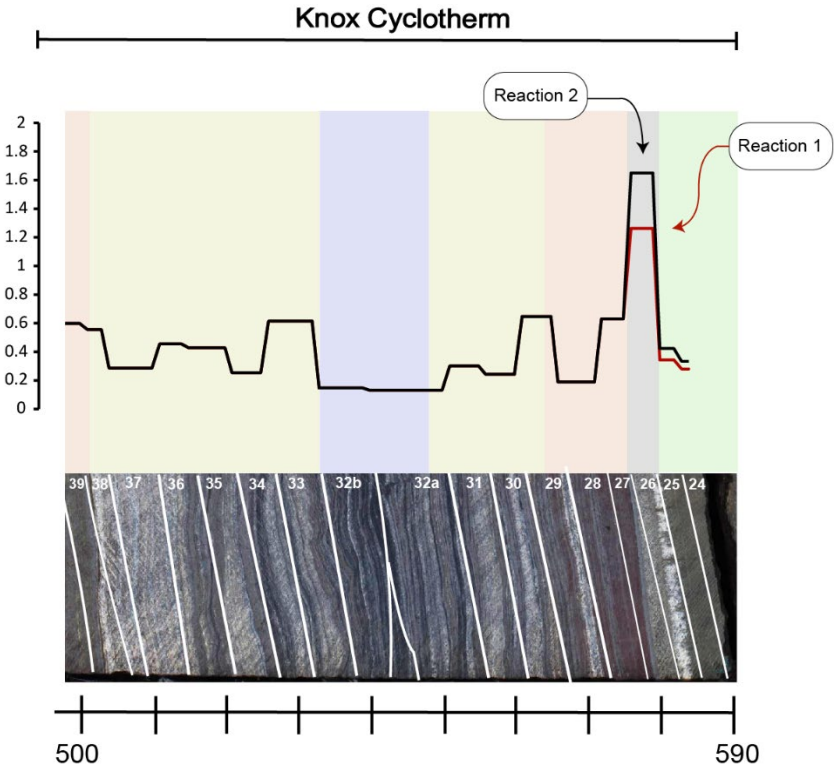


***Fig 22 –*** *Mass balancing model of the Wt% $C_{org\ initial}$ as calculated from the stable carbonate isotopes data and the EA-IRMS data. Since we were not able to measure the isotope composition of the hematite carbonate mesobands, we included two different stoichiometric approaches to calculate the Wt% $C_{org\ initial}$ (see Appendix 7). Different mesobands are highlighted in green (biotite carbonate silicate mesoband), grey (hematite carbonate mesoband), yellow (microbanded chert), and red (hematite/microbanded oxide). Also included are the positions of the sample slices. The organic carbon flux peaks in the hematite carbonate mesobands and retains a background value in the other mesobands.*

Overall, our data support the view that the original organic matter in the pre-diagenetic sediment fluctuated systematically throughout the Knox cyclothem and thus the precession-cycle. The carbonate-rich BIF facies experienced an intense remineralization of the original organic matter coupled to a quantitative removal of the ferrihydrite. In contrast, the oxide BIF facies were characterized by a ferrihydrite concentration that outweighed the original organic carbon in the pre-diagenetic BIF sediment, resulting in a near quantitative oxidation of the organic matter. Finally, the carbon-poor chert BIF facies experienced a relatively low amount of diagenetic reworking because of a limited availability of both organic matter and ferrihydrite. Therefore, the variability in organic carbon in the sediment strongly influenced the subsequent diagenetic redox cycling and the final BIF mineralogy.

## 6.2 Why did the organic matter fluctuate over the Knox cyclothem?

### 6.2.1 Sediment accessibility and redox cycling within the water column

Multiple processes could have controlled the fluctuations of the organic carbon along the Knox cyclothem. For example, the fluctuations in original carbon flux to the sediment may have been controlled by the primary bioproductivity in the water column, whereas the carbon flux could also have been controlled through changes in the intensity of the redox cycling within the water column itself (i.e. stratification of the ocean water column), the latter which could have controlled the amount of carbon that effectively reached the sediment pile. Since most of the original organic carbon was remineralized during diagenesis, it is difficult to find direct evidence that supports either of these scenarios. Therefore, we opted to investigate this problem by comparing the carbonate isotope signatures and the C/N ratios of the *shaly* BIF (interval J57e) to the *classic* BIF (interval J36c), which we complemented with nitrogen isotopes of interval J36c.

First of all, the distinct $\delta^{13}C_{carb}$ and $\delta^{18}O_{carb}$ signatures of the carbonates in the two intervals reflect a different ratio between the remineralized organic carbon versus the bicarbonate derived from the ocean water column during the precipitation of the BIF siderites. Importantly, this ratio was higher for interval J57e (1:4) with respect to interval J36c (1:3), suggesting that the *shaly* BIF was more accessible to the ocean water column to bicarbonate relative to the *classic* BIF. The differences regarding the accessibility between our intervals can be explained by a delayed onset of DIR in *classic* BIF. This delay could reflect a lowered reaction rate for DIR in the absence of abundant high-reactive organic matter in the BIF sediment (Arndt et al., 2013; Seiter et al., 2005). Therefore, we argue that the *shaly* BIF was characterized by a higher original organic carbon flux that kinetically enhanced the microbial degradation of organic matter in the very early stages of sedimentation. Supporting evidence for this comes from the higher carbonate content of the *shaly* BIF with respect to the *classic* BIF, which reflects a more intense diagenetic reworking of the original sediment (Appendix 5). Another argument that supports this interpretation comes from the *shaly* carbonate BIF facies of interval J57e, which have $\delta^{13}C_{carb}$ signatures that are heavier than -7.5‰. Importantly, these signatures are incompatible with an exclusive role of DIR and must reflect a mixture of DIR related carbonates and an additional carbonate fraction that precipitated from chemical equilibrium with the water column. The precipitation of such carbonates was mostly likely related to an increase in alkalinity through an intensification of DIR (Jiang & Tosca, 2019). The additional carbonate fraction must have had an isotope signature of $\delta^{13}C_{carb} \approx 0$‰ and $\delta^{18}O_{carb} \approx$ ~22-25‰ if siderite precipitated from the water column in the scenario of excess $Fe^{2+}$ in the water column, or an isotope signature of $\delta^{13}C_{carb} \approx 0$‰ and $\delta^{18}O_{carb} \approx$ ~18-21‰ if calcite and/or dolomite precipitated from the ocean water column (Heimann et al., 2010). We argue that there is evidence for both types of mixing; most samples of the *shaly* carbonate BIF facies have similar oxygen $\delta^{18}O_{carb}$ signatures (~20.5‰) as the samples of the *shaly* oxide BIF facies, which

suggests that equilibrium calcite/dolomite was intermixed with the DIR-related siderite, resulting in a shift of the $\delta^{13}C_{carb}$ signature along arrow A (Fig 20). The direct precipitation of calcite and/or dolomite could also explain why interval J57e is strongly enriched in Mg, Ca and Sr with respect to interval J36c (~133% more Ca, ~20% more Sr, and ~27% more Mg) (Appendix 5). However, we also found a linear relation between the $\delta^{13}C_{carb}$ and the $\delta^{18}O_{carb}$ signatures for the samples from the *shaly* carbonate BIF facies. We interpreted this as a binary mixing line (Fig 20), in which the siderite generated in equilibrium with seawater ($\delta^{18}O_{carb}$ = ~25.5‰ and $\delta^{13}C_{carb}$ ≈ 0‰ as estimated from the intersect of regression line) intermixed with the siderite generated through DIR. This mixing would have resulted in a shift of the isotope signatures along arrow B (Fig 20). A simple binary mixing calculation suggests that about 20% of the carbonate in the *shaly* carbonate BIF facies must have precipitated from chemical equilibrium with the ocean water to explain a shift of $\delta^{13}C_{carb}$ ≈ -7.5‰ to $\delta^{13}C_{carb}$ ≈ -5‰ (assuming a isotopically homogeneous ocean with $\delta^{13}C_{DIC}$ ≈ 0‰).

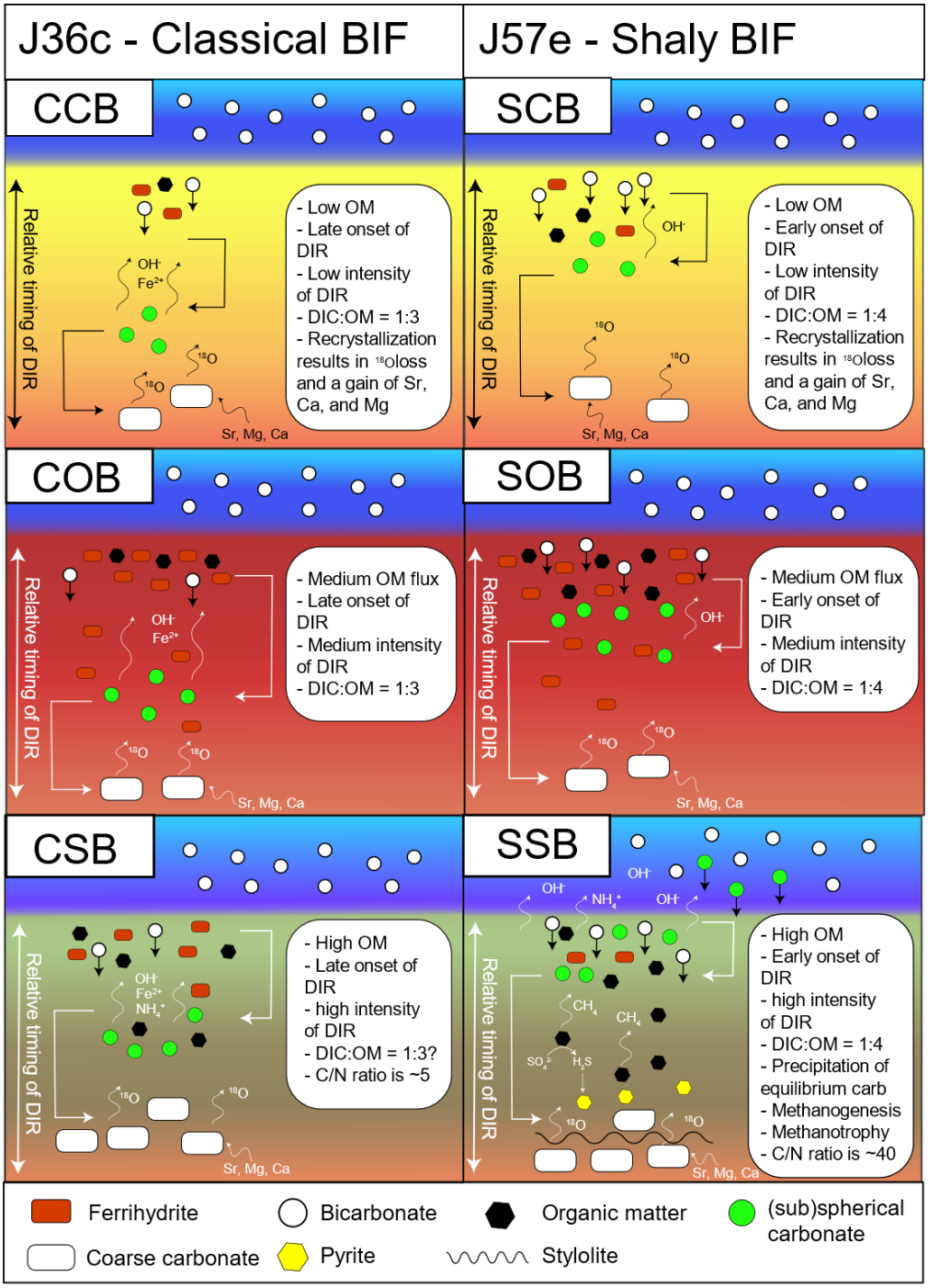


***Fig 23** – The diagenetic reworking of the BIF sediment. The first arrow (right side) indicates the onset of DIR, which was delayed for the classic BIF with respect to the shaly BIF. The second arrow (left side) indicates the onset of the recrystallization of the carbonates, with post-dated DIR but pre-dated metamorphism and facilitated the loss of $^{18}O$ and the gain of Sr, Mg, and Ca for the coarse carbonates. Overall, the shaly BIF was characterized by a more intense diagenetic reworking which in case of the carbonate facies (SSB) resulted in a direct precipitation of carbonate from the ocean water column due to an increase in alkalinity. Furthermore, excess organic matter in this mesoband may have triggered methanogenesis and sulphate reduction, the latter which could have resulted in the generation of diagenetic pyrite. Finally, $NH_4^+$ was more efficiently captured by clay minerals of the classic BIF as opposed to the shaly BIF. Abbreviations: **CCB** is the classic chert BIF facies. **SCB** is the shaly chert BIF facies. **COB** is the classic oxide BIF facies. **SOB** is the shaly oxide BIF facies. **CSB** is the classic siderite BIF facies. And finally, **SSB** is the shaly siderite BIF facies.*

Finally, the higher average C/N ratios of interval J57e (~40) with respect to interval J36c (~5) are more in line with the expected values for organic matter in low-metamorphic Archean rocks (Busigny et al., 2013). This suggests that less $NH_4^+$ was incorporated into the clay minerals in interval J57e with respect to interval J36c, which is supported by the poor correlation between N and Al for interval J57e (Fig 18). We propose three different mechanisms that could explain this difference: 1) a substantial amount of the $NH_4^+$ escaped the pore water fluid in interval J57e before it could be incorporated within the clay minerals, 2) the degradation of organic matter already started within the water column, which consequently resulted in a modest incorporation of $NH_4^+$ into clay particles, and 3) released $NH_4^+$ was rapidly re-assimilated by heterotrophic and/or autotrophic organisms in either the sediment or the water column. Although the $\delta^{18}O_{carb}$ and $\delta^{13}C_{carb}$ signatures and C/N ratios show that the *shaly* BIF was characterized by a more intense redox cycling with respect to the *classic* BIF (Fig 23), we argue that these geochemical proxies by themselves cannot be used to specify if the fluctuations in the organic matter were caused by changes in the primary bioproductivity or by an intensification of redox cycling within the water column itself.

However, we did note that the intensification of DIR in both intervals coincided with an increase in terrigenous material from the continents, as seen from the accumulation of stilpnomelane and HFS elements in the carbon-rich mesobands (Appendix 7) and the petrographic evidence of pyroclastic shards of feldspar and/or quartz in the *classic* carbonate BIF facies of interval J36c. The source of the terrigenous material could therefore have been a mixture of pyroclastic debris and a Fe-rich clay. The latter is supported by the presence of stilpnomelane spherules in the chert BIF facies, which likely formed after flocculates of clay particles (e.g. smectite) that interacted with the dissolved Fe(II) in the ocean water. Analogue to this are the stilpnomelane needles, which appear to be the recrystalized end-product of Fe-clays/ash particles that were originally deposited in microbands. Importantly, a terrigenous source that contained Fe-rich clays would also explain why K and Ti are so strongly coupled, since both elements can be readily incorporated into clay minerals. The combined ICP-OES data and XRF records indicate that an increase of terrigenous material coincides with an increase in (bio-limiting) trace elements (e.g. P, Al, Ba, Be, Ce, K, Mg, S, Sc, Sr, Ti, V, and Y) that were transferred to the sediment pile via the adsorption onto organic matter and/or Fe(III)-oxyhydroxides (Bishop et al., 2019; Konhauser et al., 2018). It follows that the episodic input of Fe-rich clays and pyroclastic debris introduced bio-limiting trace elements into the water column, which triggered changes in the primary bioproductivity in the water column and consequently controlled the variations of the original organic carbon along the Knox cyclothem in the pre-diagenetic BIF sediment. The relation between bio-limiting trace-elements and bioproductivity during BIF deposition has been proposed before (Bekker et al., 2014; Konhauser et al., 2018; Robbins et al., 2019) and is well-recognized in modern environments (Brumsack, 2006). However, we also argue that the relation between terrigenous input and bioproductivity only provides indirect evidence for changes in bioproductivity and does not rule out the possibility that redox cycling of organic matter within the water column itself occurred as well.

### 6.2.2 The role of nitrogen isotopes to track the primary bioproductivity over the Knox cyclothem

To further constrain if bioproductivity was indeed the main driver of the variations of the original organic carbon along the Knox cyclothem in the pre-diagenetic BIF sediment, we investigated the nitrogen isotopes of the *classic* carbonate BIF facies of interval J36c. The nitrogen isotope signatures of our samples were first tested for the influence of diagenesis and metamorphism, since these processes are known to influence with the $\delta^{15}N$ signatures (Stuëken et al., 2015). It was experimentally demonstrated that the $\delta^{15}N$ signature remains virtually unaffected during early diagenetic degradation of organic matter in anoxic to suboxic environments ($\Delta^{15}N$ <1 ‰) (Möbius et al., 2010; Ader et al., 1998). The breakdown of $NH_4^+$ to $NH_3$ at elevated alkalinities (pKa >9.24) and low temperatures (~25 °C) is known to impose a significant isotope fractionation on the $NH_4^+$, which in some specific settings can reach values of up to 50‰ (Stuëken et al., 2015). However, we do not see these extreme $\delta^{15}N$ signatures in our intervals and there is no reason to expect such high alkalinities during the diagenetic

reworking of the sediments. This is because the alkalinity in BIF sediments was partly buffered by carbonate precipitation (Howell et al., 1998). The $\delta^{15}N$ signature of $NH_4^+$ in phyllosilicates can also be elevated during metamorphism by the preferred loss of $^{14}N$ over $^{15}N$ through Rayleigh devolatilization (Mingram & Bräuer, 2001). The positive offsets are most significant for high-grade metamorphic conditions. For example, amphibolite facies metamorphism which was characterized by an intense loss of nitrogen was accompanied by an increase of the $\delta^{15}N$ signature of 4.3 +/- 0.8 ‰, whereas high-greenschist facies metamorphism with less significant loss of nitrogen was accompanied by a more modest increase of the $\delta^{15}N$ signature of 1.9 +/- 0.6 ‰ (Jia, 2006). Since our intervals experienced only mild prehnite-pumpellyite facies metamorphism (>300 °C), it seems unlikely that the measured $\delta^{15}N$ signatures were strongly elevated by loss of nitrogen (<1 ‰). This is further supported by the poor relation between the Wt% N and the related $\delta^{15}N$ signatures (Fig 24). Such a relation is typically well-expressed in high-grade metamorphic rocks (Jia, 2006).

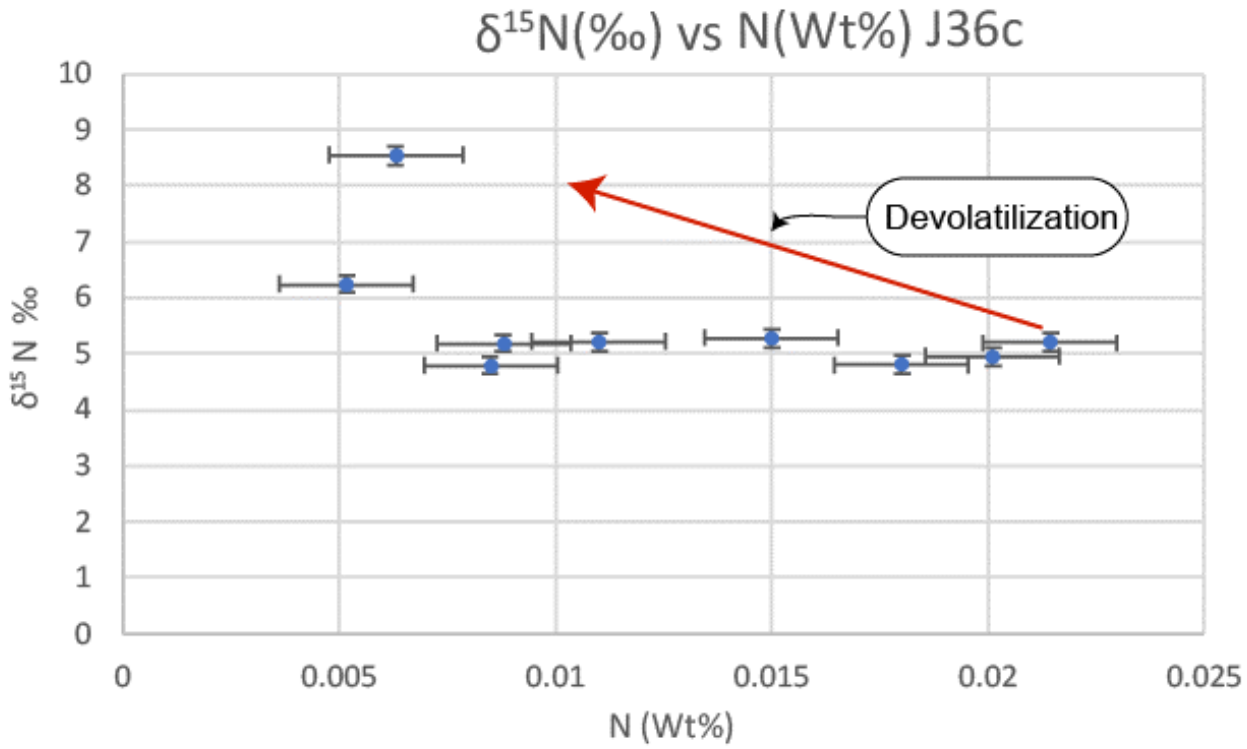


***Fig 24 –*** *The $\delta^{15}N$ vs Wt% N plot suggests that metamorphic induced devolatilization was of minor importance for our samples. That is apart from the one sample that has a $\delta^{15}N$ signature of ~8.5‰. Most of the data plot in a narrow $\delta^{15}N$ range that is characterized by varying amounts of Wt% N.*

It seems therefore that that the isotope signatures reflected primary (biogenic) fractionation processes, a similar conclusion reached by $\delta^{15}N$ studies of the Dales Gorge member (Busigny et al., 2013) and lacustrine sediments of the Fortescue group (Stuëken et al., 2015). The Archean marine nitrogen cycle was much different than the modern nitrogen cycle. Nitrogen was mostly incorporated into the marine system as di-nitrogen ($N_2$) by anaerobic and aerobic autotrophic organisms from an isotopically homogenous atmosphere ($\delta^{15}N \approx 0$ ‰), whereas nitrate ($NO_3^-$) availability was scarce (Godfrey et al., 2009). Fixed nitrogen was bound into the organic matter of aerobic autotrophs as amine groups ($-NH_2$) and the fractionation accompanying this fixation was small (<3 ‰) and depended on the utilized metal cofactor in the nitrogenase enzyme (Busigny et al., 2013; Thomazo & Papineau, 2013; Godfrey & Glass, 2011). The nitrogen bound into the organic matter was released as $NH_4^+$ upon

heterotrophic degradation in the water column or within the sediment. Under anoxic conditions this was characterized by a small fractionation (<1 ‰). Consequently, most of the dissolved $NH_4^+$ in the water column carried a signature of $\delta^{15}N \approx 0$ ‰. This could change dramatically if partial assimilation took place, but this fractionation mechanism is believed to have occurred only under restricted geological circumstances (Thomazo & Papineau, 2013). Importantly, a part of the organic matter that was degraded was released as $NH_4^+$ within the sediment. Such $NH_4^+$ could be incorporated into clay minerals, which explains why many Archean kerogen shows signatures of $\delta^{15}N \approx 0$ ‰ (Ader et al., 2016). Following a similar line of logic, we would expect a nitrogen isotope signature of $\delta^{15}N \approx 0$ ‰ for our intervals as well, given that nitrogen-fixation was the dominant fractionation pathway in the Archean oceans.

However, the samples show consistently elevated $\delta^{15}N$ signatures that do not support this interpretation. Therefore, we argue that there must have been an additional fractionation mechanism that operated alongside this *simple* nitrogen-fixation. There are two relevant pathways that could explain elevated $\delta^{15}N$ signatures for (deep) marine sediments (Busigny et al., 2013). Firstly, partial nitrification of $NH_4^+$ in a fully anoxic water column or a fully anoxic sediment could have resulted in the formation of nitrite ($NO_2^-$), a process characterized by a significant isotope fractionation of 10 – 40‰ since nitrite prefers the incorporation of $^{14}N$ (Casciotti et al., 2003). The residual $NH_4^+$ would consequently be enriched in $^{15}N$. Microbial assimilation of the residual $NH_4^+$ by either autotrophic or heterotrophic organisms could subsequently have transferred this nitrogen to the sediment pile, explaining the observed increase in the $\delta^{15}N$ signatures. In contrast, the produced nitrite would be rapidly lost from the water column by quantitative denitrification due to an access of available reductants (e.g. $Fe^{2+}$, $Mn^{2+}$, $C_{org}$). Importantly, there are two main oxidants that could have facilitated the partial oxidation of $NH_4^+$. Firstly, free oxygen produced by photosynthesisers could have acted as a powerful oxidant. However, since $Fe^{2+}$ and $Mn^{2+}$ were also oxidized in the presence of free oxygen, this would suggest that multiple reductants competed against each other for the available $O_2$, which would likely have resulted in some elemental correlations (e.g. during an increased Fe(II) supply, partial $NH_4^+$ oxidation would decrease). However, we did not find such correlations. A second oxidant that could have facilitated the partial oxidation of $NH_4^+$ was the abundance of Fe(III)-oxyhydroxides that were present in the water column and the sediment. However, we did not find a statistical relevant correlation between the Wt% Fe and the $\delta^{15}N$ values that would support such a reaction pathway. Furthermore, (Stüeken et al., 2016) argued that partial nitrite oxidation would result in a wide range of $\delta^{15}N$ signatures, which is incompatible with the narrow range of $\delta^{15}N$ signatures that we find in our samples (Stüeken et al., 2016). Therefore, we argue that partial nitrification of $NH_4^+$ in a fully anoxic water column was not the dominant fractionation mechanism that can explain the elevated the $\delta^{15}N$ signatures of our samples. A second mechanism to explain the $\delta^{15}N$ signatures would be through the quantitative oxidation of $NH_4^+$ in an oxygenic surface layer of the ocean, followed by partial denitrification and/or annamox. This would be accompanied by a significant isotope fractionation of 10 – 40‰, which would leave the residual nitrate in the oxygenic surface layer enriched in $\delta^{15}N$. The assimilation of this nitrate by autotrophic or heterotrophic organisms could have transferred the elevated $\delta^{15}N$ signatures to the sediment pile (Garvin et al., 2009; Delarue et al., 2018; Godfrey et al., 2009). Indeed, this process has been well documented in modern marine systems and sediments that postdated the GOE (Zerkle et al., 2017; Cheng et al., 2019).

Some workers remain skeptical of the significance of nitrification-denitrification redox cycling in a redox-stratified marine environment prior to the GOE (Mettam et al., 2019). They base this on nitrogen isotope studies of shallow marine sediments characterized by a high bioproductivity and related oxygen production in the upper water column. The $\delta^{15}N$ signatures in these rocks are predominantly <0 ‰, which implies that denitrification-nitrification redox cycling only had a limited effect on the overall nitrogen isotope signatures, and that atmospheric nitrogen-fixation and (partial) assimilation of dissolved $NH_4^+$ were the main contributors to the $\delta^{15}N$

signature of these rocks (Papineau et al., 2009). A similar binary mixing model was proposed by Busigny et al., (2013), who suggested that high productivity in shallow environments was characterized by $\delta^{15}$N signatures close to 0 ‰, whereas distal marine environments were characterized by $\delta^{15}$N signatures of ~8 ‰, which they attributed to a smaller contribution from organic matter derived from autotrophic nitrogen fixers. Instead, the carbon flux was characterized by a larger contribution from the assimilation of $^{15}$N enriched nitrate from a redox-stratified ocean by autotrophic and heterotrophic organisms. Therefore, we argue that the $\delta^{15}$N record is a highly valuable tool for testing changes in the primary bioproductivity in the water column during BIF deposition. Based on the narrow range of elevated $\delta^{15}$N signature and the absence of depleted $\delta^{15}$N signatures (~ 0 ‰) in our samples, we argue for a relatively distal BIF depositional setting and a relatively low bioproductivity in a redox-stratified water column, which agrees with the findings of (Dodd et al., 2019; Busigny et al., 2013). We further argue against the high organic carbon flux to the sediment (>4 Wt%) that was proposed by (Konhauser et al., 2017). Such high carbon flux would more likely result in as shift of the $\delta^{15}$N signatures towards ~0 ‰. Finally, the nitrogen isotope record highlights the importance of redox cycling of organic matter within the water column itself, suggesting that changes in bioproductivity were not the only mechanism that influenced the carbon flux towards the BIF sediment pile. Unfortunately, our data were not detailed enough to investigate if the $\delta^{15}$N signature fluctuated between individual mesobands and/or mineralogical facies and if it varied between interval J57e and interval J36c. We argue that collecting additional high-resolution $\delta^{15}$N data would be valuable next step to directly test if the changes in the primary bioproductivity were indeed the main driver behind the fluctuations of the original organic carbon along the Knox cyclothem.

### 6.2.3 How did the Fe(III)-flux fluctuate over the Knox cyclothem?

Although we found strong evidence for a fluctuating concentration of the original organic carbon on the Knox cyclothem, it was also important to investigate how this was related to the flux of Fe(III) to the sediment. This is because the concentration of organic carbon relative to the concentration of ferrihydrite determined the intensity of DIR. We argue that the Mn vs Fe trend could provide a way to track the flux of Fe(III) to the sediment. Firstly, the Mn trend seemed to mirror the carbonate trend, which suggested that most Mn occurred as substitutions within siderite, which was a similar conclusion reached by (Oonk, 2017). There are essentially two ways in which the Mn could have been incorporated into the carbonates: 1) via the direct incorporation of divalent Mn that was present in the pore-water fluid or the ocean water column, or via 2) a diagenetic incorporation of divalent Mn that was generated through dissimilatory manganese reduction (DMR) by reducing Mn(III) and Mn(IV) oxides at the expense of organic carbon. The second scenario would require a flux of oxidized Mn to the sediment pile, which may be expected in a redox-stratified ocean where free oxygen and/or nitrate were present above a redoxcline. Alternatively, it has been proposed that manganese was photo-oxidized by autotrophic organisms in a similar manner as photoferrotrophy (Johnson et al., 2013; Chernev et al., 2020), although direct evidence that supports this reaction pathway has not yet been identified (Konhauser et al., 2017). We suspect that Mn oxidation in the upper ocean water column did occur, but we have strong reasons to believe that the Mn-oxides never reached the sediment pile:

- We did not find petrographic evidence for manganese oxides, although this could be countered by the argument that all Mn-oxides were quantitatively reduced during early diagenesis (Johnson et al., 2013).
- We suspect that highly-reactive Mn(IV) and possibly Mn(III) were quantitatively reduced in the water column through either: 1) microbially regulated oxidation of organic matter which would be thermodynamically favorable over the oxidation of organic matter through DIR, 2) microbially regulated oxidation of $NH_4^+$, although this reaction mechanism was likely of minor importance (Thamdrup &

Dalsgaard, 2000), 3) microbially regulated oxidation of methane (Leu et al., 2020), or 4) abiotically regulated oxidation of Fe(II) in the presence of Mn-oxides. Especially this latter reaction pathway could have been relevant in a ferruginous Archean ocean. Indeed, abiotic reduction of Mn-oxides was recently identified as a potential redox mechanism that was active during the deposition of BIFs in South Africa (i.e. based on combined $\delta^{98}$Mo and $\delta^{56}$Fe signatures) (Kurzweil et al., 2016). Furthermore, the abiotic reduction of manganese oxides has been recorded in modern ferruginous lakes and has been demonstrated to facilitate an intense redox cycling of Mn along the redoxcline (Jones et al., 2011).

- Mn-oxides are preferably reduced in the presence of organic carbon over Fe-oxides in the water column, but also during diagenetic reworking of the sediment. Therefore, if DMR occurred in the *shaly* oxide BIF facies of interval 57e, the microbially generated $Mn^{2+}$ would have been higher relative to the microbially generated $Fe^{2+}$, resulting in an increased incorporation of Mn into carbonates relative to Fe. In contrast, the *shaly* carbonate BIF facies are characterized by more extensive reworking of DIR. Therefore, the $Mn^{2+}$ concentration would have been lower relative to the $Fe^{2+}$, resulting in a decreased incorporation of Mn relative to the Fe into the carbonates. This would ultimately result in a Mn trend opposite to the Fe and Mn trends observed in J57e, which implies that the observed Mn trend is incompatible with DMR.

It is much more likely that the $Mn^{2+}$ concentration remained near constant below the redoxcline and was systematically incorporated into the siderites generated through DIR via the interaction between seawater and pore-water fluid. Such an open diagenetic system was also favored for the precipitation of carbonates by Mehrnaz et al., (2020). Therefore, the increase of Mn over the Knox cyclothem would simply reflects a more active role of DIR. In contrast, Fe was distributed over a variety of phases (i.e. stilpnomelane, carbonates, riebeckite, pyrite, biotite, magnetite, and hematite), which explains why Mn and Fe are poorly coupled in both intervals (Fig 16). The most important phases in which Fe could have resided are hematite and magnetite, whereas the other phases were relatively iron poor (e.g. stilpnomelane typically contained >10 Wt% of the Fe in the samples and siderite contained >5 Wt% of the Fe in the samples – see Appendix 7). The hematite occurred in three different flavors, which were the skeletal hematite, the dusty hematite, and the tabular hematite. The skeletal hematite and dusty hematite were early BIF minerals that formed after the dehydration of a ferrihydrite precursor. This view is supported by oxygen isotope analyses of hematite microbands, which point at dehydration temperature of a ferrihydrite precursor at temperatures lower than 150 °C (Becker and Clayton, 1976). In addition, (li et al., 2013) used in-situ oxygen isotopes to argue that some of the dusty hematite grains formed at temperatures as low as 25 °C. In contrast, the tabular hematite was a secondary mineral that was generated through late-diagenetic recrystallization of dusty hematite and skeletal hematite via *localized* dissolution precipitation mechanisms (Putnis, 2009). The magnetite microbands appeared to have formed at different stages in time. Some predated the riebeckite growth, while others postdated the riebeckite growth. The intimate association of many magnetite layers with hematite and siderite and the occurrence of carbonate and hematite inclusions in some of the magnetite microbands strongly suggests a late diagenetic reaction in which magnetite formed at the expense of hematite and siderite. Alternatively, DIR could have generated excess Fe(II) that interacted with hematite microbands to form magnetite microbands. We tentatively argue that both processes were of importance, since the magnetite formation texturally appeared to have been a continuous process. This is supported by T – $\Delta\delta^{18}O_{\mathrm{qz-mag}}$ data of (Li et al., 2013), who argued that some of the magnetite microbands (i.e. high Si-magnetite) were formed at temperatures of >150 °C and some of the magnetite microbands (i.e. low Si-magnetite) were formed at lower temperatures of ~50-100 °C. There are several reactions that can explain the occurrence of magnetite: 1) the metamorphic reaction between siderite and

hematite could have resulted in the formation of magnetite (reaction 1). Alternatively, 2) the disassociation of siderite could have occurred in the presence of water at elevated temperatures of >200 °C (reaction 2) (Ramussen & Muhling, 2018). And finally, 3) the reduction of hematite with organic matter at elevated temperatures could have resulted in the formation of magnetite (reaction 3). We were not able to identify which of these mechanisms was dominant.

1) $FeCO_3 + Fe_2O_3 \rightarrow Fe_3O_4 + CO_2$
2) $3FeCO_3 + H_2O \rightarrow Fe_3O_4 + 3CO_2 + H_2$
3) $6Fe_2O_3 + C \rightarrow 4Fe_3O_4 + CO_2$

Finally, randomly oriented magnetite euhedra overgrow all other phases in the thin sections, including magnetite microbands and the euhedral riebeckite. Consequently, the euhedral magnetite is likely a completely metamorphic mineral. This idea is supported by measurements of T – $\Delta\delta^{18}O_{\text{qz}-\text{mag}}$ data, which suggest formation temperatures of 170 – 330 °C (Li et al., 2013; Becker & Clayton, 1976). An overview of the relative timing of the main minerals that we encountered in our BIF intervals is shown in Fig 25 and further discussed in Appendix 8.

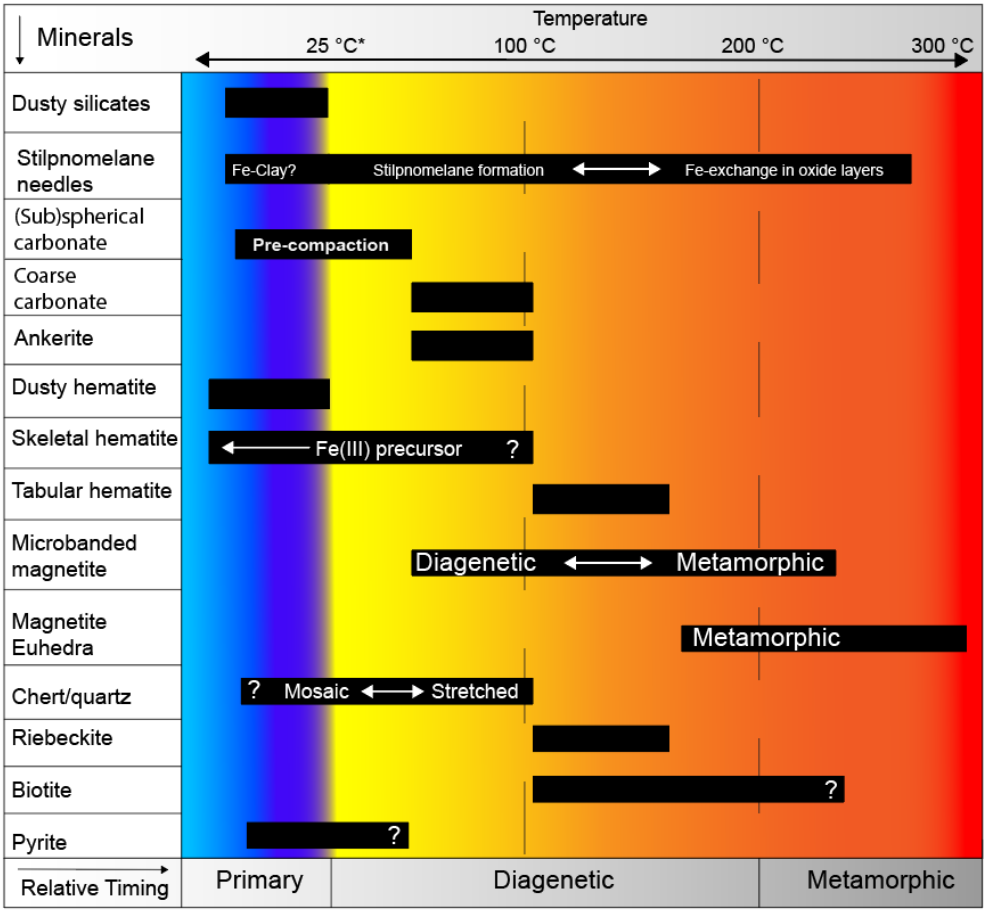


***Fig 25 –*** *Our interpretation of the relative timing of mineral growth during the formation of our intervals based on petrographic observations and published stable oxygen isotope data. Note that most carbonates were early diagenetic. Most hematite was a relatively early diagenetic mineral (with the exception of tabular hematite), whereas most magnetite was a relatively late diagenetic to metamorphic mineral. We decided against including the three different species of riebeckite, since their formation temperatures must have been quite similar.*

So the bulk of the hematite was deposited as primary ferrihydrite since tabular hematite was only a minor phases. In addition, most of the magnetite formed through a reaction in which hematite was involved, with the exception of the euhedral magnetite. Since hematite and magnetite are the major phases in which Fe resides,

we argue that the Fe trend in the XRF record thus reflects the initial flux of ferrihydrite to the sediment pile. In interval J57e, the systematic decline of Fe along the Knox cyclothem from the *shaly* oxide BIF facies towards the *shaly* chert BIF facies implies that iron was abruptly but episodically introduced into the water column during the deposition of interval J57e and was gradually removed from solution by direct or indirect microbial oxidation. Consequently, the *shaly* oxide BIF facies would coincide with the highest Fe(III) flux towards the sediment, whereas the *shaly* chert BIF facies would coincide with the lowest Fe(III) flux towards the sediment. In contrast, interval J36c does not display the same out-of-sync zigzag pattern of Fe and Mn along the Knox cyclothem. This suggests that the Fe concentration in the ocean water column was not replenished on the precession-scale and was not quantitively oxidized by microbial activity in the upper water column. However, based on the relatively low Fe concentration found in the *classic* chert BIF facies, we argue that changes in the relative Fe(III)-flux still occurred.

### 6.2.4 What was the source of Fe(II) and was Fe(III) mobilized after BIF deposition?

We decided to use the Fe/Co ratio to further investigate how and why the flux of the Fe(III) to the sediment varied during the deposition of both *shaly* BIF and *classic* BIF. Firstly, the Fe/Co ratio is semi-quantitative and does not signify an absolute value, since this would imply an unrealistically high Co concentration (~3000 ppm). However, the Fe/Co ratio can still be used to evaluate the relative changes between mineralogically distinct BIF facies for both intervals (Appendix 5). The constant Fe/Co ratio for interval J36c suggests that the Fe and Co were strongly coupled and were probably sampled from a similar source (Swanner et al., 2014). High-temperature hydrothermal solutions are known to efficiently leach Co from oceanic basalts, much more so than similar transition metals like Cu and Ni. Furthermore, Co-chloride complexes are relatively stable under low temperatures, which suggests that they can be transported over large distances, especially considering a ferruginous ocean (Metz et al., 2000). Based on the strong hydrothermal imprint on the Joffre Member (Haugaard et al., 2016), we argue that the Co and Fe for interval J36c were likely derived from a high-temperature hydrothermal system.

The Co flux to the sediment could have been facilitated by several mechanisms. Firstly, Co could have been carried to the sediment via a flux of Mn(III) and Mn(IV) oxides. This is because Co(II) is oxidized under similar conditions as Mn(II), which means that it can be readily incorporated into the crystal lattice of Mn-oxides (Takahashi et al., 2007). However, we argue that such a flux of Mn-oxides to the sediment pile was unlikely to have occurred (see section Mn trends). Alternatively, Co(III) and Co(II) could have been adsorbed onto the surfaces of Fe(III)-oxyhydroxides, which have been argued to effectively scavenge Co(II) under ferruginous anoxic settings (Swanner et al., 2014). Importantly, in this scenario dissolved silica and organic matter may have competed for surface binding sites, which could influence the Fe/Co ratio during the deposition of the different BIF facies (Konhauser et al. 2009). However, based on the similar Fe/Co ratio throughout the entire interval, we argue that such surface-site inhibition did not affect the affinity of Fe(III)-oxyhydroxides to scavenge Co from the ocean water column. Therefore, the Co flux towards the sediment was strictly regulated by the formation of Fe(III)-oxyhydroxides, which also explains why Co and Fe are so strongly coupled (Fig 17).

The constant Fe/Co trends in J36c confirm the earlier proposition that *classic* BIF was less accessible to the water column. This is because the surface bound Co would be readily released during the reduction of Fe(III)-oxyhydroxides (Swanner et al., 2014). The Fe(II) generated through DIR was partly incorporated in siderite. In contrast, Co only tends to form its own carbonate phases (i.e. $CoCO_3$) under very high Eh-pH conditions (Swanner et al., 2014) and Co substitution into carbonates is relatively limited for BIFs (Oonk, 2017). Rather, the

released Co was predominantly re-adsorbed onto supplementary Fe(III)-oxyhydroxides, magnetite, and/or Fe-silicates in the direct vicinity of the generated siderite. Therefore, Co and Fe were incorporated preferably into different phases during diagenetic reworking of the sediment. It follows that hat the mobilization of both Co and Fe was limited to a mm-scale resolution to maintain a constant Fe/Co trend. This agrees with earlier findings for limited Ni and Zn mobility in *classic* BIFs (Robbins et al., 2015).

In contrast, the fluctuating Fe/Co ratio of interval J57e suggests that Fe and Co behaved quite differently between the *shaly* oxide BIF facies and the *shaly* chert BIF facies. This is unlikely to have reflected changes in the competition for surface binding sites by silica since the total Si in both intervals is near constant (i.e. J57e is only 3% more enriched in Si as opposed to J36c – see Appendix 5), which implies that silica adsorption by Fe(III)-oxyhydroxides was also of a same order of magnitude. Alternatively, the competition for binding sites was a result of an increase of adsorbed organic matter onto the ferrihydrite, which would result in a higher Fe/Co ratio (Sader et al., 2010). We do see a higher Fe/Co ratio in the *shaly* oxide BIF facies and *shaly* carbonate BIF facies as opposed to the *shaly* chert BIF facies, which were believed to have had a higher original organic carbon flux as opposed to the *shaly* chert BIF facies (see mass-balancing model). However, the *shaly* carbonate BIF facies were expected to have the highest organic carbon flux (see section mass balancing) and this is not reflected in the Fe/Co ratio. Therefore, the inhibition of surface-sites by organic carbon on ferrihydrite was also unlikely to significantly influence the Fe/Co ratio. There are three alternatives to explain the fluctuations in the Fe/Co ratio between the *shaly* oxide BIF facies and the *shaly* chert BIF facies: 1) the difference in the Fe/Co ratio reflects changes in the Fe(II) concentration of the water column relative to the Co(II) concentration. However, for this to work, the sources of Fe and Co must have been partly decoupled, which can be explained through mixing hydrothermal derived Fe and Co with an additional iron source (i.e. the two regression lines of Fig 17). This additional iron source could have been continental, since continental iron is characterized by a higher Fe/Co ratio as opposed to hydrothermal effluents, especially in the Archean oceans (Swanner et al., 2014). A continental iron source would also explain why the *shaly* oxide BIF facies in J57e are always temporarily associated with terrigenous-rich *shaly* carbonate BIF facies. Alternatively, the 2) the fluctuations in the Fe/Co ratio reflect an interaction of dissolved Fe(II) from the ocean water column with the original BIF sediment. This is because the formation of early magnetite through the incorporation of Fe(II) from the water column could elevate the Fe/Co ratio without the need for an additional Fe-source. This process could also explain why the *shaly* oxide BIF facies show the highest Fe/Co ratios, since these facies are characterized by the highest magnetite content. However, this scenario requires that most of the magnetite formed during early diagenesis, since the accessibility with respect to the ocean water column had to be high. In contrast, most magnetite appears to be a late diagenetic to metamorphic feature. Finally, 3) the gradual decline of the Fe/Co ratio could indicate a loss of Fe(II) relative to Co(II) from the system. The Fe loss was possible facilitated by the late diagenetic dissolution/recrystallization of the by DIR generated siderite, whereas Co remained preferably adsorbed onto the surfaces of remaining magnetite/hematite oxides and Fe-silicates, hence increasing the Fe/Co ratio. This interpretation would explain why a decrease of the Fe/Co ratio was accompanied by an increase in petrographic textures related to recrystallization and why the Fe/Co ratio is lowest for the most recrystallized carbonates of the *shaly* chert BIF facies. Since this would have been a gradual process it would fit with the parabolic curve of Fig 17. Of course, there is also the possibility that all processes operated simultaneously and asserted different degrees of control on the overall Fe/Co ratio. Therefore, additional in-situ analyses of the Fe/Co ratio of magnetite and siderite are needed to distinguish what mechanism was dominant in this respect.

## 6.3 A renewed climate-regulated BIF deposition model

We combined the fluctuations of the organic matter and Fe(III) flux in a conceptual BIF model that explains the formation of the mineralogically distinct facies that define the Knox cyclothem. We argue that the deposition of the chert BIF facies (Fig 26 – A) was a continuous background process that was relatively similar for both intervals. The Fe(III) flux to the sediment pile was low and the terrestrial input was limited (i.e. with the exception of the thin silicate mesobands). Consequently, the bioproductivity in the water column was low, resulting in a reduced carbon flux to the sediment and minimal diagenetic reworking. Furthermore, intense Mn-cycling along the redoxcline prevented a flux of Mn-oxides to the sediment pile. In contrast, we argue that the deposition of the oxide facies was facilitated through the biogenic oxidation of iron in the upper water column (Fig 26 – B). In the *shaly* BIF, ferrous iron was episodically introduced through a hydrothermal (?) and/or a continental (?) source. In the *classic* BIF, ferrous iron was not episodically introduced into the water column, but the Fe(III) flux to the sediment was still higher with respect to the chert BIF facies. Although the bioproductivity during the deposition of the oxide BIF facies may have been higher with respect to that of the chert BIF facies, the abundance of ferrihydrite relative to the organic carbon in the BIF precursor sediment still resulted in a quantitative removal of the organic matter through DIR in both the *shaly* and the *classic* BIF. During this reworking, the *shaly* BIF was more accessible with respect to the water column as opposed to the *classic* BIF, presumably through a larger contribution of the original organic carbon from the water column and an earlier kinetic onset and intensification of the diagenetic redox cycling. Finally, the carbonate BIF facies highlight an expansion of the primary bioproductivity through an increase in terrigenous material (Fig 26 – C). The high organic matter flux to the sediment relative to the Fe(III) flux resulted in a quantitative removal of the ferrihydrite and the precipitation of abundant carbonates. In the shaly BIF the excess organic matter may even have triggered additional redox cycling such as methanogenesis and sulphate reduction. Furthermore, a strong increase of DIR related alkalinity controlled the precipitation of additional carbonates from chemical equilibrium with the seawater. Finally, nitrification and denitrification may have been active in the water column as well, resulting in isotopically heavy nitrogen isotope signatures in the organic rich facies of the Joffre Member. We argue that changes in the primary bioproductivity (and possibly the intensity of redox-cycling in the water column) must have been (indirectly) regulated through a climate sensitive system that operated on the precession scale and that could have controlled the availability of bio-limiting trace elements in the water column. An interesting but speculative climate mechanism that could have facilitated this is the monsoon-related delivery of terrigenous material and/or continentally derived Fe(II) to the distal parts of the ocean where BIF was actively deposited (Lantink et a., 2019). Monsoonal intensity is controlled by seasonal contrast and thus precession forcing. This is because it strictly relies on the asymmetric heating of the continents and the oceans (Trenberth et al., 2000; Zhu et al., 2005; Bosmans et al, 2014). At the same time, the monsoon intensity asserts a strong influence on regional precipitation by increasing or decreasing the continental runoff and the availability of bio-essential nutrients with respect to precession minimum and precession maximum (Sarathchandraprasad & Banakar, 2018). The link between monsoonal derived trace elements and fluctuations in bioproductivity has also been convincingly demonstrated in modern environments and could have been important during the deposition of the Joffre Member (Cruz et al., 2007; Lazareth et al., 2003; Ziegler et al. 2010). Alternatively, bioproductivity could have been stimulated through monsoonal upwelling of ferruginous and nutrient-rich waters (Warren et al., 1984; Emeis et al., 1995; Bak & Nieuwland, 1997) or the monsoonal regulated delivery of continental dust and/or pyroclastic material to the distal parts of the ocean (Larrasoaña et al., 2003). The latter idea fits with the interpretation of (Haugaard et al., 2016), who argued that the terrigenous material in the Joffre Member was primarily derived from a volcaniclastic source. Finally, monsoonal winds may have influenced the

surface water temperature, which could have further increased or decreased bioproductivity in the water column, although this was likely complemented by the availability of bio-limiting trace elments (Zheng et al., 2004; Konhauser et al., 2008; Schad et al., 2019).

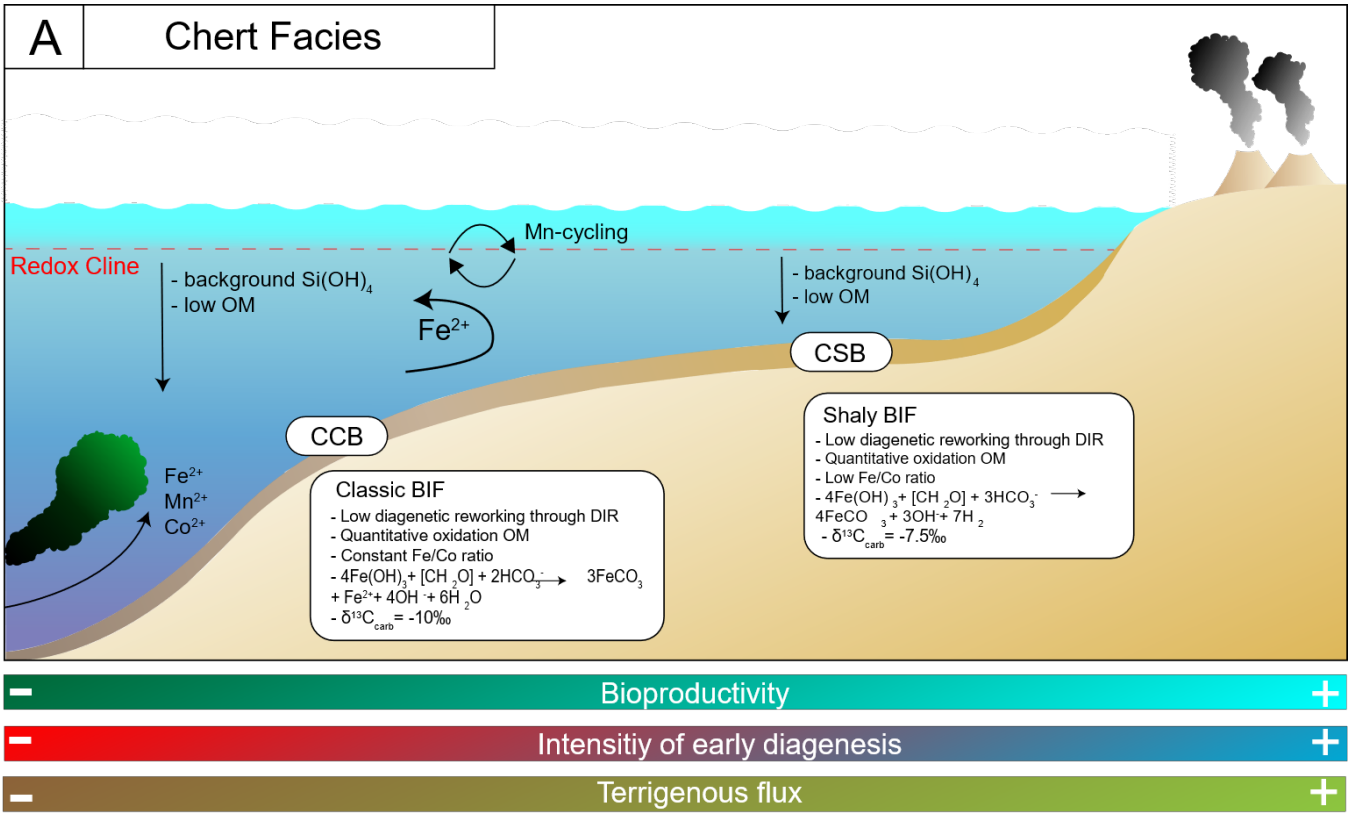

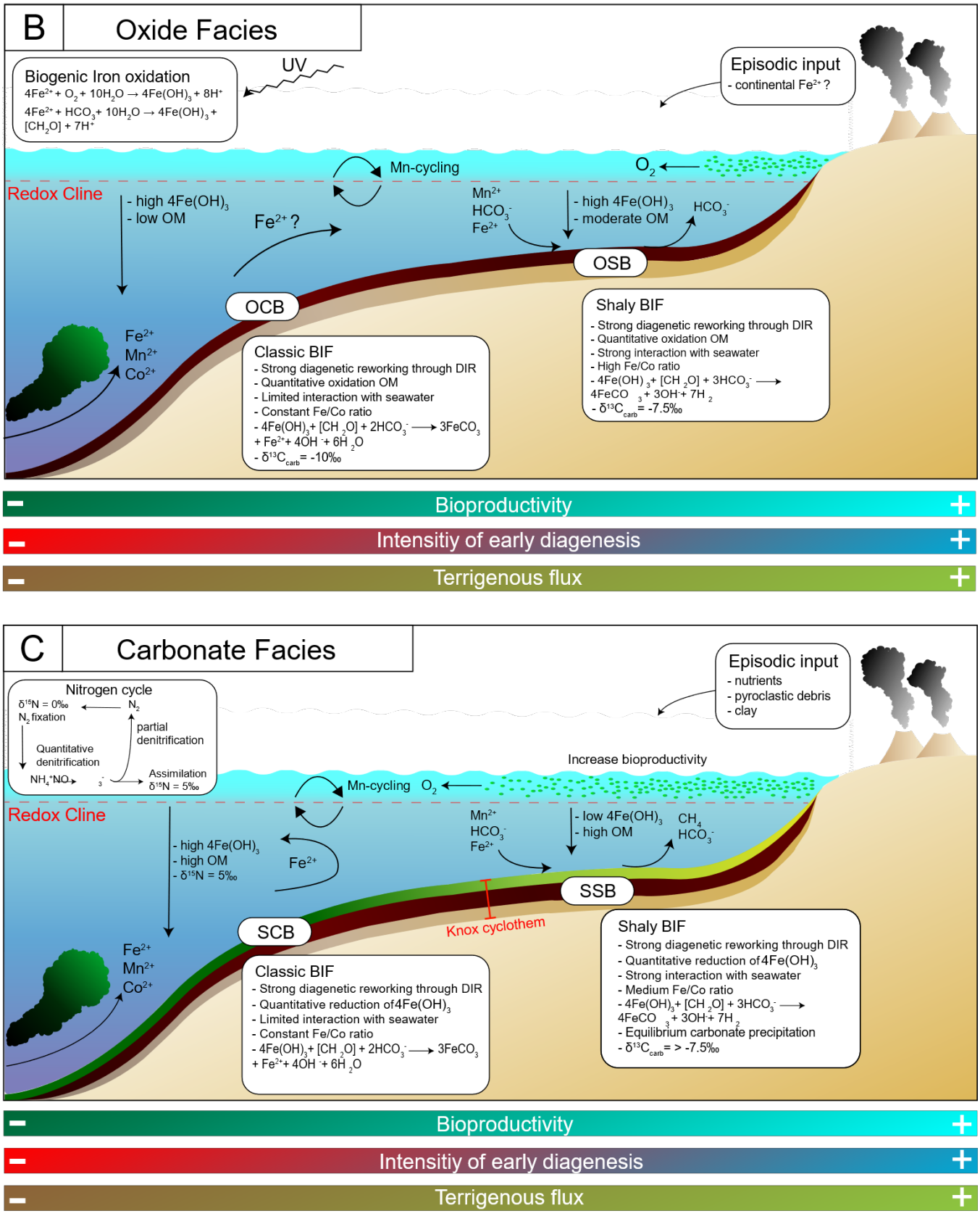


***Fig 26–*** *Conceptual model of the formation of different mesobands during the deposition of our intervals. The right-side of the figures is representative for shaly BIF (interval J57e) and the left-side of the figure is representative for classic BIF (interval J36c). The bars beneath the figures indicate the relative change in the bioproductivity, the intensity of early diagenesis, and the terrigenous flux of the intervals. Abbreviations:* ***CCB*** *is the classic chert BIF facies.* ***SCB*** *is the shaly chert BIF facies.* ***COB*** *is the classic oxide BIF facies.* ***SOB*** *is the shaly oxide BIF facies.* ***CSB*** *is the classic siderite BIF facies. And finally,* ***SSB*** *is the shaly siderite BIF facies*

# 7 Conclusion

The petrographic observations combined with the trends in the Wt% Carbonate and the highly depleted $\delta^{13}C_{carb}$ and $^{18}O_{carb}$ signatures of the carbonates suggest that microbially-regulated dissimilatory iron reduction (DIR) had a leading role in the early diagenetic redox cycling of the BIF sediment. The redox cycling and its relative intensity were regulated by the availability of the organic matter, which varied strongly and systematically throughout the precession-scale Knox cyclothem. In the scenario that excess organic carbon was present relative to the Fe(III)-oxyhydroxides, supplementary sulphate reduction and methanogenesis could have been active. Within the *shaly* BIF the intensification of the redox cycling may even have triggered the precipitation of additional carbonate from direct chemical equilibrium with the ocean water column. Therefore, the availability of organic carbon in the original BIF sediment was a master variable that directly controlled the formation of the mineralogically distinct mesobands along the precession-scale Knox cyclothem in the Joffre Member. Importantly, the intensity of the redox cycling increased during periods of a higher organic carbon flux to the sediment and decreased during periods of a lower organic carbon flux to the sediment. These fluctuations likely reflected changes in the bioproductivity in the water column, although the role of redox cycling within the water column itself should be further tested to substantiate this idea. The fluctuations in the bioproductivity were presumably controlled through the episodical introduction of bio-limiting trace elements and nutrients into the ocean. Such episodical input of terrigenous material was driven by a climate sensitive system that responded to changes in total seasonal insolation and thus precession forcing (e.g. precession-driven changes in monsoonal runoff and dust delivery and/or upwelling events). Finally, the accessibility of the BIF sediments with respect to oceanwater column during diagenetic redox cycling was larger for the *shaly* BIF when compared to the *classic* BIF. This hints at a larger flux of the original organic carbon to the sediment and a consequently kinetically faster and more intense diagenetic reworking of the sediment. The differences between the *shaly* and *classic* BIFs fit in a wider context of a BIF depositional model and suggest that the role of bioproductivity relative to the Fe(III)-flux may have been undervalued. Consequently, future research should aim to clarify this discrepancy, preferably through obtaining a high-resolution $\delta^{15}N_{total}$ record along the Knox cyclothem. Overall, our findings demonstrate that climate strongly influenced the deposition of BIFs on a precession scale. Therefore, the Joffre Member and possibly other Superior-type BIFs have the potential to track changes in the redox-state of the Archean oceans, which makes BIFs valuable tools to investigate climate change on the early Earth.

# 8 Acknowledgement

I would first like to express my gratitude to the NWO for indirectly sponsoring this master thesis project. Without the financial support I would not have been able to finish this project. Furthermore, I would like to thank the geological survey of Western Australia for their wiliness to provide us with the necessary core intervals and the NIOZ for helping us obtain the high-resolution XRF data of the Joffre core. I wish to express my deepest gratitude to Margriet Lantink, Prof. Dr. Paul Mason, and Dr. Frits Hilgen for their excellent guidance during the making of this thesis and their willingness to participate into continuous intellectual debate. It was a real pleasure working with you. Furthermore, my sincere thanks go out to all the lab personal that endured my endless questions and who were instrumental in getting this thesis to completion. I specifically want to express my gratitude to Natasja Welters, Coen Mulder and Arnold van Dijk for their patience and excellent guidance during the lab work. Of course, I want to thank my fellow master students as well. Our endless bickering at the coffee machine helped me enjoy this thesis project to the fullest and kept me lighthearted at even the most challenging moments. Last but not least, I would like to thank my family and friends for their constant source of inspiration and positivity.

# 9 References


Achtnich, C., Bak, F., & Conrad, R. (1995). Competition for electron donors among nitrate reducers, ferric iron reducers, sulfate reducers, and methanogens in anoxic paddy soil. *Biology and Fertility of Soils, 19*(1), 65-72.

Ader, M., Thomazo, C., Sansjofre, P., Busigny, V., Papineau, D., Laffont, R., . . . Halverson, G. (2016). Interpretation of the nitrogen isotopic composition of Precambrian sedimentary rocks: Assumptions and perspectives. *Chemical Geology, 429*, 93-110.

Alibert, C., & McCulloch, M. (1993). Rare earth element and neodymium isotopic compositions of the banded iron-formations and associated shales from Hamersley, Western Australia. *Geochimica et Cosmochimica Acta, 57*(1), 187-204.

Arndt, N., Nelson, D., Compston, W., Trendall, A., & Thorne, A. (1991). The age of the Fortescue Group, Hamersley Basin, Western Australia, from ion microprobe zircon U-Pb results. *Australian Journal of Earth Sciences, 38*(3), 261-281.

Arndt, S., Jørgensen, B., LaRowe, D., Middelburg, J., Pancost, R., & Regnier, P. (2013). Quantifying the degradation of organic matter in marine sediments: a review and synthesis. *Earth-Science Reviews, 123*, 53-86.

Bak, R., & Nieuwland, G. (1997). Seasonal variation in bacterial and flagellate communities of deep-sea sediments in a monsoonal upwelling system. *Deep Sea Research Part II: Topical Studies in Oceanography, 44*(6-7), 1281-1292.

Bekker, A., Planavsky, N., Rasmussen, B., Krapez, B., Hofmann, A., Slack, J., . . . Konhauser, K. (2014). Iron formations: Their origins and implications for ancient seawater chemistry. *Treatise on geochemistry,* 12, 561-628.

Beukes, N., Klein, C., Kaufman, A., & Hayes, J. (1990). Carbonate petrography, kerogen distribution, and carbon and oxygen isotope variations in an early Proterozoic transition from limestone to iron-formation deposition, Transvaal Supergroup, South Africa. *Economic geology and the bulletin of the Society of Economic Geologists, 85*(4), 663-690.

Bishop, B., Flynn, S., Warchola, T., Alam, M., Robbins, L., Liu, Y., . . . Konhauser, K. (2019). Adsorption of biologically critical trace elements to the marine cyanobacterium Synechococcus sp. PCC 7002: Implications for marine trace metal cycling. *Chemical Geology, 525*, 28-36.

Bosmans, J., Drijfhout, S., Tuenter, E., Hilgen, F., & Lourens, L. (2015). Response of the North African summer monsoon to precession and obliquity forcings in the EC-Earth GCM. *Climate Dynamics, 44*(1-2), 279-297.

Boudreau, B. (1987). A steady-state diagenetic model for dissolved carbonate species and pH in the porewaters of oxic and suboxic sediments. *Geochimica et Cosmochimica Acta, 51*(7), 1985-1996.

Brocks, J., Love, G., Snape, C., Logan, G., Summons, R., & Buick, R. (2003). Release of bound aromatic hydrocarbons from late Archean and Mesoproterozoic kerogens via hydropyrolysis. *Geochimica et Cosmochimica Acta, 67*(8), 1521-1530.

Brumsack, H.-J. (2006). The trace metal content of recent organic carbon-rich sediments: implications for Cretaceous black shale formation. *Palaeogeography, Palaeoclimatology, Palaeoecology, 232*(2-4), 344-361.

Bryce, C., Blackwell, N., Schmidt, C., Otte, J., Huang, Y.-M., Kleindienst, S., . . . Peng, C. (2018). Microbial anaerobic Fe (II) oxidation–Ecology, mechanisms and environmental implications. *Environmental microbiology, 20*(10), 3462-3483.

Busigny, V., Lebeau, O., Ader, M., Krapez, & Bekker, A. (2013). Nitrogen cycle in the Late Archean ferruginous ocean. *Chemical Geology, 362*, 115-130.

Cairns-Smith, A. (1978). Precambrian solution photochemistry, inverse segregation, and banded iron formations. *Nature, 276*(5690), 807.

Casciotti, K., Sigman, D., & Ward, B. (2003). Linking diversity and stable isotope fractionation in ammonia-oxidizing bacteria. *Geomicrobiology Journal, 20*(4), 335-353.

Cheng, C., Busigny, V., Ader, M., Thomazo, C., Chaduteau, C., & Philippot, P. (2019). Nitrogen isotope evidence for stepwise oxygenation of the ocean during the Great Oxidation Event. *Geochimica et Cosmochimica Acta, 261*, 224-247.

Chernev, P., Fischer, S., Hoffmann, J., Oliver, N., Burnap, R., Zaharieva, I., . . . Dau, H. (2020). Light-driven formation of high-valent manganese oxide by photosystem II supports evolutionary role in early bioenergetics. *bioRxiv*.

Cloud, P. (1965). Significance of the Gunflint (Precambrian) Microflora: Photosynthetic oxygen may have had important local effects before becoming a major atmospheric gas. Science, 148(3666), 27-35.

Cook, P. (1976). Sedimentary phosphate deposits. Au, U, Fe, Mn, Hg, Sb, W, and P deposits. 505-535.

Craddock, P., & Dauphas, N. (2011). Iron and carbon isotope evidence for microbial iron respiration throughout the Archean. Earth and Planetary Science Letters, 303(1-2), 121-132.

Czaja, A., Johnson, C., Beard, B., Eigenbrode, J., Freeman, K., & Yamaguchi, K. (2010). Iron and carbon isotope evidence for ecosystem and environmental diversity in theâˆ¼ 2.7 to 2.5 Ga Hamersley Province, Western Australia. Earth and Planetary Science Letters, 292(1-2), 170-180.

Dauphas, N., Zuilen, M., Wadhwa, M., Davis, A., Marty, B., & Janney, P. (2004). Clues from Fe isotope variations on the origin of early Archean BIFs from Greenland. Science, 306(5704), 2077-2080.

Delarue, F., Robert, F., Sugitani, K., Tartese, R., Duhamel, R., & Derenne, S. (2018). Nitrogen isotope signatures of microfossils suggest aerobic metabolism 3.0 Gyr ago. Geochem Perspect Lett, 7, 32-36.

Dodd, M., Papineau, D., Pirajno, F., Wan, Y., & Karhu, J. (2019). Minimal biomass deposition in banded iron formations inferred from organic matter and clay relationships. Nature communications, 10(1), 1-13.

Egglseder, M., Cruden, A., Tomkins, A., Wilson, S., & Langendam, A. (2018). Colloidal origin of microbands in banded iron formations. Geochemical Perspectives Letters, 6, 43-49.

Eigenbrode, J., & Freeman, K. (2006). Late Archean rise of aerobic microbial ecosystems. Proceedings of the National Academy of Sciences, 103(43), 15759-15764.

Estes, E., Pockalny, R., D'Hondt, S., Inagaki, F., Morono, Y., Murray, R., . . . Xiao, N. (2019). Persistent organic matter in oxic subseafloor sediment. Nature Geoscience, 12(2), 126-131.

Garvin, J., Buick, R., Anbar, A., Arnold, G., & Kaufman, A. (2009). Isotopic evidence for an aerobic nitrogen cycle in the latest Archean. *Science, 323*(5917), 1045-1048.

Gill, & T. (1999). *Annual Report for Silvergrass Peak E47/845 for the period 5/3/98 to 4/3/99.* Department of Minerals and Energy Western Australia.

Godfrey, L., & Glass, J. (2011). The geochemical record of the ancient nitrogen cycle, nitrogen isotopes, and metal cofactors. *Methods in enzymology,* 486, 483-506.

Haddouzi, A. (2019). Official title uknown - About precession cyclicity in the Dales Gorge BIF of Western Australia. *Master thesis project*.

Halama, M., Swanner, E., Konhauser, K., & Kappler, A. (2016). Evaluation of siderite and magnetite formation in BIFs by pressure-temperature experiments of Fe (III) minerals and microbial biomass. *Earth and Planetary Science Letters, 450*, 243-253.

Haugaard, R., Pecoits, E., Lalonde, S., Rouxel, O., & Konhauser, K. (2016). The Joffre banded iron formation, Hamersley Group, Western Australia: Assessing the palaeoenvironment through detailed petrology and chemostratigraphy. *Precambrian Research, 273*, 12-37.

Heck, P., Huberty, J., Kita, N., Ushikubo, T., Kozdon, R., & Valley, J. (2011). SIMS analyses of silicon and oxygen isotope ratios for quartz from Archean and Paleoproterozoic banded iron formations. *Geochimica et Cosmochimica Acta, 75*(20), 5879-5891.

Heimann, A., Johnson, C., Beard, B., Valley, J., Roden, E., Spicuzza, M., & Beukes, N. (2010). Fe, C, and O isotope compositions of banded iron formation carbonates demonstrate a major role for dissimilatory iron reduction in ~2.5 Ga marine environments. *Earth and Planetary Science Letters, 294*(1), 8-18.

Hoof, A., Os, B., Rademakers, J., Langereis, C., & Lange, G. (1993). A paleomagnetic and geochemical record of the upper Cochiti reversal and two subsequent precessional cycles from Southern Sicily (Italy). *Earth and Planetary Science Letters, 117*(1-2), 235-250.

Howell, J., Donahoe, R., Roden, E., & Ferris, F. (1998). Effects of microbial iron oxide reduction on pH and alkalinity in anaerobic bicarbonate-buffered media: implications for metal mobility. *Mineralogical Magazine A, 62*, 657-658.

Jacobsen, S., & Pimentel-Klose, M. (1988). Nd isotopic variations in Precambrian banded iron formations. *Geophysical Research Letters, 15*(4), 393-396.

James, H. (1954, 3). Sedimentary facies of iron-formation. *Economic Geology, 49*(3), 235-293.

Jia, Y. (2006). Nitrogen isotope fractionations during progressive metamorphism: A case study from the Paleozoic Cooma metasedimentary complex, southeastern Australia. *Geochimica et Cosmochimica Acta, 70*(20), 5201-5214.

Jiang, C., & Tosca, N. (2019). Fe (II)-carbonate precipitation kinetics and the chemistry of anoxic ferruginous seawater. *Earth and Planetary Science Letters, 506*, 231-242.

Johnson, C., Beard, B., Klein, C., Beukes, N., & Roden, E. (2008). Iron isotopes constrain biologic and abiologic processes in banded iron formation genesis. *Geochimica et Cosmochimica Acta, 72*(1), 151-169.

Johnson, C., Ludois, J., Beard, B., Beukes, N., & Heimann, A. (2013). Iron formation carbonates: Paleoceanographic proxy or recorder of microbial diagenesis? *Geology, 41*(11), 1147-1150.

Johnson, J., Webb, S., Thomas, K., Ono, S., Kirschvink, J., & Fischer, W. (2013). Manganese-oxidizing photosynthesis before the rise of cyanobacteria. *Proceedings of the National Academy of Sciences, 110*(28), 11238-11243.

Jones, C., Crowe, S., Sturm, A., Leslie, K., MacLean, L., Katsev, S., . . . Middelburg, J. (2011). Biogeochemistry of manganese in ferruginous Lake Matano, Indonesia. *Biogeosciences, 8*(10).

Jr, F., Burns, S., Jercinovic, M., Karmann, I., Sharp, W., & Vuille, M. (2007). Evidence of rainfall variations in Southern Brazil from trace element ratios (Mg/Ca and Sr/Ca) in a Late Pleistocene stalagmite. *Geochimica et Cosmochimica Acta, 71*(9), 2250-2263.

Kaufman, A., Hayes, J., & Klein, C. (1990). Primary and diagenetic controls of isotopic compositions of iron-formation carbonates. *Geochimica et Cosmochimica Acta, 54*(12), 3461-3473.

Klein, C. (1992). Time distribution, stratigraphy, and sedimentologic setting, and geochemistry of Precambrian iron-formation. *Proterozoic Biosphere*.

Klein, C. (2005). Some Precambrian banded iron-formations (BIFs) from around the world: Their age, geologic setting, mineralogy, metamorphism, geochemistry, and origins. *American Mineralogist, 90*(10), 1473-1499.

Koeksoy, E., Halama, M., Konhauser, K., & Kappler, A. (2016). Using modern ferruginous habitats to interpret Precambrian banded iron formation deposition. *International Journal of Astrobiology, 15*(3), 205-217.

Konhauser, K., Amskold, L., Lalonde, S., Posth, N., Kappler, A., & Anbar, A. (2007). Decoupling photochemical Fe (II) oxidation from shallow-water BIF deposition. *Earth and Planetary Science Letters, 258*(1-2), 87-100.

Konhauser, K., Newman, D., & Kappler, A. (2005). The potential significance of microbial Fe (III) reduction during deposition of Precambrian banded iron formations. Geobiology, 3(3), 167-177.

Konhauser, K., Pecoits, E., Lalonde, S., Papineau, D., Nisbet, E., Barley, M., . . . Kamber, B. (2009). Oceanic nickel depletion and a methanogen famine before the Great Oxidation Event. Nature, 458(7239), 750-753.

Konhauser, K., Planavsky, N., Hardisty, D., Robbins, L., Warchola, T., Haugaard, R., . . . Johnson, C. (2017). Iron formations: A global record of Neoarchaean to Palaeoproterozoic environmental history. Earth-Science Reviews, 172, 140-177.

Konhauser, K., Posth, N., Hegler, F., & Kappler, A. (2008). Alternating Si and Fe deposition caused by temperature fluctuations in Precambrian oceans. Nature Geoscience, 1(10), 703-708.

Konhauser, K., Robbins, L., Alessi, D., Flynn, S., Gingras, M., Martinez, R., . . . Crowe, S. (2018). Phytoplankton contributions to the trace-element composition of Precambrian banded iron formations. Bulletin, 130(5-6), 941-951.

Kuleshov, V., & Maynard, J. (2017). Manganese carbonates in modern sediments. Isotope Geochemistry: The Origin and Formation of Manganese Rocks and Ores: Amsterdam, Elsevier, 5-62.

Kuntz, L., Laakso, T., Schrag, D., & Crowe, S. (2015). Modeling the carbon cycle in Lake Matano. Geobiology, 13(5), 454-461.

Lantink, M., Davies, J., Mason, P., Schaltegger, U., & Hilgen, F. (2019). Climate control on banded iron formations linked to orbital eccentricity. Nature geoscience, 12(5), 369-374.

Lantink, M. (2020a). In preparation. Official title uknown. About precession cyclicity in the Joffre Member of Western Australia .

Lantink, M. (2020b). In preparation. Official title unknown. About transport modelling of the precession-cycles in the Joffre Member.

Larrasoaña, J., Roberts, A., Rohling, E., Winklhofer, M., & Wehausen, R. (2003). Three million years of monsoon variability over the northern Sahara. Climate Dynamics, 21(7-8), 689-698.

Lazareth, C., Putten, E., André, L., & Dehairs, F. (2003). High-resolution trace element profiles in shells of the mangrove bivalve Isognomon ephippium: a record of environmental spatio-temporal variations? Estuarine, Coastal and Shelf Science, 57(5-6), 1103-1114.

Leu, A., Cai, C., McIlroy, S., Southam, G., Orphan, V., Yuan, Z., . . . Tyson, G. (2020). Anaerobic methane oxidation coupled to manganese reduction by members of the Methanoperedenaceae. *The ISME Journal, 14*(4), 1030-1041.

Li, W., Beard, B., & Johnson, C. (2015). Biologically recycled continental iron is a major component in banded iron formations. *Proceedings of the National Academy of Sciences, 112*(27), 8193-8198.

Li, W., Huberty, J., Beard, B., Kita, N., Valley, J., & Johnson, C. (2013). Contrasting behavior of oxygen and iron isotopes in banded iron formations revealed by in situ isotopic analysis. *Earth and Planetary Science Letters, 384*, 132-143.

Li, Y. L. (2014). Micro-and nanobands in late Archean and Palaeoproterozoic banded-iron formations as possible mineral records of annual and diurnal depositions. *Earth and Planetary Science Letters, 391*, 160-170.

Li, Y. L., Konhauser, K., Kappler, A., & Hao, X. L. (2013). Experimental low-grade alteration of biogenic magnetite indicates microbial involvement in generation of banded iron formations. *Earth and Planetary Science Letters, 361*, 229-237.

Martin, W., Bryant, D., & Beatty, J. (2017). A physiological perspective on the origin and evolution of photosynthesis. *FEMS microbiology reviews, 42*(2), 205-231.

Mehrnaz, S., Tsikos, H., Rafuza, S., Oonk, P., Mhlanga, X., Niekerk, D., Mason, P., & Harris, C. (2020). In preperation. BIFs, GIFs and WHIFFs: insights into the processes and controls for the absolute abundance and distribution of manganese in Precambrian Iron Formations.

Mettam, C., Zerkle, A., Claire, M., Prave, A., Poulton, S., & Junium, C. (2019). Anaerobic nitrogen cycling on a Neoarchaean ocean margin. *Earth and Planetary Science Letters, 527*, 115800.

Mingram, B., & Bräuer, K. (2001). Ammonium concentration and nitrogen isotope composition in metasedimentary rocks from different tectonometamorphic units of the European Variscan Belt. *Geochimica et Cosmochimica Acta, 65*(2), 273-287.

Möbius, J., Lahajnar, N., & Emeis, K. C. (2010). Diagenetic control of nitrogen isotope ratios in Holocene sapropels and recent sediments from the Eastern Mediterranean Sea. *Biogeosciences Discussions, 7*(1).

Morris, R. (1993). Genetic modelling for banded iron-formation of the Hamersley Group, Pilbara Craton, Western Australia. *Precambrian Research, 60*(1-4), 243-286.

Morris, R., & Horwitz, R. (1983). The origin of the iron-formation-rich Hamersley Group of Western Australia - deposition on a platform. *Precambrian Research, 21*(3-4), 273-297.

Morris, R., & Wolff, K. (1985). Genesis of iron ore in banded iron-formation by supergene and supergene-metamorphic processes—a conceptual model. *Handbook of strata-bound and stratiform ore deposits, 13*, 73-235.

Nisbet, E., & Fowler, C. (1999). Archaean metabolic evolution of microbial mats. *Proceedings of the Royal Society of London.Series B: Biological Sciences, 266*(1436), 2375-2382.

Oonk, P. (2017). Fraction-specific geochemistry across the Asbestos Hills BIF of the Transvaal Supergroup, South Africa: implications for the origin of BIF and the history of atmospheric oxygen. *Unpublished doctoral dissertation.*

Ozawa, A., Ueda, A., Fantong, W., Anazawa, K., Yoshida, Y., Kusakabe, M., . . . Hell, J. (2017). Rate of siderite precipitation in Lake Nyos, Cameroon. *Geological Society, London, Special Publications, 437*(1), 213-222.

Partridge, M., Golding, S., Baublys, K., & Young, E. (2008). Pyrite paragenesis and multiple sulfur isotope distribution in late Archean and early Paleoproterozoic Hamersley Basin sediments. *Earth and Planetary Science Letters, 272*(1-2), 41-49.

Percak-Dennett, E., Beard, B., Xu, H., Konishi, H., Johnson, C., & Roden, E. (2011). Iron isotope fractionation during microbial dissimilatory iron oxide reduction in simulated Archaean seawater. *Geobiology, 9*(3), 205-220.

Pickard, A. (2002). SHRIMP U-Pb zircon ages of tuffaceous mudrocks in the Brockman Iron Formation of the Hamersley Range, Western Australia. *Australian Journal of Earth Sciences, 49*(3), 491-507.

Pickard, A. (2002). SHRIMP U–Pb zircon ages of tuffaceous mudrocks in the Brockman Iron Formation of the Hamersley Range, Western Australia. *Australian Journal of Earth Sciences, 49*(3), 491-507.

Pickard, A., Barley, M., & Krapež, B. (2004). Deep-marine depositional setting of banded iron formation: Sedimentological evidence from interbedded clastic sedimentary rocks in the early Palaeoproterozoic Dales Gorge Member of Western Australia. *Sedimentary Geology, 170*(1-2), 37-62.

Posth, N., Koehler, I., Swanner, E., Schröder, C., Wellmann, E., Binder, B., . . . Nowak, M. (2013). Simulating Precambrian banded iron formation diagenesis. *Chemical Geology, 362*, 66-73.

Posth, N., Konhauser, K., & Kappler, A. (2013). Microbiological processes in banded iron formation deposition. *Sedimentology, 60*(7), 1733-1754.

Powell, C., Oliver, N., Li, Z.-X., Martin, D., & Ronaszeki, J. (1999). Synorogenic hydrothermal origin for giant Hamersley iron oxide ore bodies. *Geology, 27*(2), 175-178.

Prell, W. (1984). Variation of monsoonal upwelling: a response to changing solar radiation. *Climate processes and climate sensitivity, 29*, 48-57.

Putnis, A. (2009). Mineral replacement reactions. *Reviews in mineralogy and geochemistry, 70*(1), 87-124.

Rasmussen, B., & Muhling, J. (2018). Making magnetite late again: evidence for widespread magnetite growth

by thermal decomposition of siderite in Hamersley banded iron formations. *Precambrian Research, 306*, 64-93.

Rasmussen, B., Krapež, B., & Meier, D. (2014). Replacement origin for hematite in 2.5 Ga banded iron formation: Evidence for postdepositional oxidation of iron-bearing minerals. *Bulletin, 126*(3-4), 438-446.

Rasmussen, B., Meier, D., Krapež, B., & Muhling, J. (2013). Iron silicate microgranules as precursor sediments to 2.5-billion-year-old banded iron formations. *Geology, 41*(4), 435-438.

Raven, J. (2013). The evolution of autotrophy in relation to phosphorus requirement. *Journal of experimental botany, 64*(13), 4023-4046.

Reddy, T., Zheng, X., Roden, E., Beard, B., & Johnson, C. (2016). Silicon isotope fractionation during microbial reduction of Fe (III)-Si gels under Archean seawater conditions and implications for iron formation genesis. *Geochimica et Cosmochimica Acta, 190*, 85-99.

Reichart, G., den Dulk, M., Visser, H., van der Weijden, C., & Zachariasse, W. (1997). A 225 kyr record of dust supply, paleoproductivity and the oxygen minimum zone from the Murray Ridge (northern Arabian Sea). *Palaeogeography, Palaeoclimatology, Palaeoecology, 134*(1-4), 149-169.

Reichart, G.-J., Lourens, L., & Zachariasse, W. (1998). Temporal variability in the northern Arabian Sea oxygen minimum zone (OMZ) during the last 225,000 years. *Paleoceanography, 13*(6), 607-621.

Rengasamy, P. (1976). Substitution of iron and titanium in kaolinites. *Clays and Clay Minerals, 24*(5), 265-266.

Robbins, L., Konhauser, K., Warchola, T., Homann, M., Thoby, M., Foster, I., . . . Lalonde, S. (2019). A comparison of bulk versus laser ablation trace element analyses in banded iron formations: Insights into the mechanisms leading to compositional variability. *Chemical Geology, 506*, 197-224.

Robbins, L., Swanner, E., Lalonde, S., Eickhoff, M., Paranich, M., Reinhard, C., . . . Konhauser, K. (2015). Limited Zn and Ni mobility during simulated iron formation diagenesis. *Chemical Geology, 402*, 30-39.

Rodrigues, P., Hinnov, L., & Franco, D. (2019). A new appraisal of depositional cyclicity in the Neoarchean-Paleoproterozoic Dales Gorge Member (Brockman Iron Formation, Hamersley Basin, Australia). *Precambrian Research, 328*, 27-47.

Rosière, C., & Jr Chemale, F. (2017). Brazilian iron formations and their geological setting. *Revista Brasileira de Geociências, 30*(2), 274-278.

Sader, J., Hattori, K., Hamilton, S., & Brauneder, K. (2011). Metal binding to dissolved organic matter and adsorption to ferrihydrite in shallow peat groundwaters: Application to diamond exploration in the James Bay Lowlands, Canada. *Applied Geochemistry, 26*(9-10), 1649-1664.

Sarathchandraprasad, T., & Banakar, V. (2018). Last 42 ky sediment chemistry of oxygen deficient coastal region of the Bay of Bengal: implications for terrigenous input and monsoon variability.

Schad, M., Halama, M., Bishop, B., Konhauser, K., & Kappler, A. (2019). Temperature fluctuations in the Archean ocean as trigger for varve-like deposition of iron and silica minerals in banded iron formations. *Geochimica et Cosmochimica Acta, 265*, 386-412.

Schaltegger, U., Schmitt, A., & Horstwood, M. (2015). U–Th–Pb zircon geochronology by ID-TIMS, SIMS, and laser ablation ICP-MS: recipes, interpretations, and opportunities. *Chemical Geology, 402*, 89-110.

Schuurman, & Tian. (2019). Carbon isotope variations in 2.5-Ga Kuruman BIF (South Africa): confirmation of Milankovitch forcing and implications for depositional mechanisms*. Master thesis project*.

Sessions, A., Doughty, D., Welander, P., Summons, R., & Newman, D. (2009). The continuing puzzle of the great oxidation event. *Current biology, 19*(14), 567-574.

Simonson, B., Schubel, K., & Hassler, S. (1993). Carbonate sedimentology of the early Precambrian Hamersley Group of western Australia. *Precambrian Research, 60*(1-4), 287-335.

Smith, R., Perdrix, J., & Parks, T. (1982). Burial metamorphism in the Hamersley basin, Western Australia. *Journal of Petrology, 23*(1), 75-102.

Stefurak, E., Lowe, D., Zentner, D., & Fischer, W. (2015). Sedimentology and geochemistry of Archean silica granules. *Bulletin, 127*(7-8), 1090-1107.

Steinhoefel, G., Horn, I., & von Blanckenburg, F. (2009). Micro-scale tracing of Fe and Si isotope signatures in banded iron formation using femtosecond laser ablation. *Geochimica et Cosmochimica Acta, 73*(18), 5343-5360.

Steinhoefel, G., von Blanckenburg, F., Horn, I., Konhauser, K., Beukes, N., & Gutzmer, J. (2010). Deciphering formation processes of banded iron formations from the Transvaal and the Hamersley successions by combined Si and Fe isotope analysis using UV femtosecond laser ablation. *Geochimica et Cosmochimica Acta, 74*(9), 2677-2696.

Stüeken, E., Buick, R., & Schauer, A. (2015). Nitrogen isotope evidence for alkaline lakes on late Archean continents. *Earth and Planetary Science Letters, 411*, 1-10.

Swanner, E., Planavsky, N., Lalonde, S., Robbins, L., Bekker, A., Rouxel, O., . . . Konhauser, K. (2014). Cobalt and marine redox evolution. *Earth and Planetary Science Letters, 390*, 253-263.

Takahashi, Y., Manceau, A., Geoffroy, N., Marcus, M., & Usui, A. (2007). Chemical and structural control of the partitioning of Co, Ce, and Pb in marine ferromanganese oxides. *Geochimica et Cosmochimica Acta, 71*(4), 984-1008.

Taner, M., & Chemam, M. (2015). Algoma-type banded iron formation (BIF), Abitibi Greenstone belt, Quebec, Canada. *Ore Geology Reviews, 70*, 31-46.

Thamdrup, B., & Dalsgaard, T. (2000). The fate of ammonium in anoxic manganese oxide-rich marine sediment. *Geochimica et Cosmochimica Acta, 64*(24), 4157-4164.

Thode, H., & Goodwin, A. (1983). Further sulfur and carbon isotope studies of late Archean iron-formations of the Canadian shield and the rise of sulfate reducing bacteria. In H. Thode, & A. Goodwin. Elsevier.

Thomazo, C., & Papineau, D. (2013). Biogeochemical cycling of nitrogen on the early Earth. *Elements, 9*(5), 345-351.

Tosca, N., Guggenheim, S., & Pufahl, P. (2016). An authigenic origin for Precambrian greenalite: Implications for iron formation and the chemistry of ancient seawater. *Bulletin, 128*(3-4), 511-530.

Tosca, N., Jiang, C., Rasmussen, B., & Muhling, J. (2019). Products of the iron cycle on the early Earth. *Free Radical Biology and Medicine, 140*, 138-153.

Trenberth, K., Stepaniak, D., & Caron, J. (2000). The global monsoon as seen through the divergent atmospheric circulation. *Journal of Climate, 13*(22), 3969-3993.

Trendall, A. (1969). The Joffre Member in the gorges south of Wittenoom. *Geological Survey Western Australia Annual Report, 1968*, 53-57.

Trendall, A. (1970). The iron formations of the Hamersley Group, Western Australia, with special reference to the associated crocidolite. *Western Australia Geological Survey Bulletin, 119*, 353.

Trendall, A. (1972). Revolution in earth history: Presidential address delivered in Brisbane on 25 May 1971. *Journal of the Geological Society of Australia, 19*(3), 287-311.

Trendall, A. (1973). Varve cycles in the Weeli Wolli Formation of the Precambrian Hamersley Group, Western Australia. *Economic Geology, 68*(7), 1089-1097.

Trendall, A. (2002). The significance of iron-formation in the Precambrian stratigraphic record. *Precambrian sedimentary environments: A modern approach to ancient depositional systems*, 33-66.

Trendall, A., Compston, W., Nelson, D., Laeter, J., & Bennett, V. (2004, 10). SHRIMP zircon ages constraining the depositional chronology of the Hamersley Group, Western Australia. *Australian Journal of Earth Sciences, 51*(5), 621-644.

Ueno, Y., Yamada, K., Yoshida, N., Maruyama, S., & Isozaki, Y. (2006). Evidence from fluid inclusions for microbial methanogenesis in the early Archaean era. *Nature, 440*(7083), 516-519.

Vaz, R. (2020). Carbon isotope stratigraphy for the 2.5-billion-year-old Dales Gorge Member, Australia: Correlation potential and Paleoclimatic significance. *Master thesis project*

Veizer, J., Clayton, R., Hlnton, R., Brunn, V., Mason, T., Buck, S., & Hoefs, J. (1990). Geochemistry of Precambrian carbonates: 3-shelf seas and non-marine environments of the Archean. *Geochimica et Cosmochimica Acta, 54*(10), 2717-2729.

Veizer, J., Hoefs, J., Lowe, D., & Thurston, P. (1989). Geochemistry of Precambrian carbonates: II. Archean greenstone belts and Archean sea water. *Geochimica et Cosmochimica Acta, 53*(4), 859-871.

Veizer, J., Hoefs, J., Ridler, R., Jensen, L., & Lowe, D. (1989). Geochemistry of Precambrian carbonates: I. Archean hydrothermal systems. *Geochimica et Cosmochimica Acta, 53*(4), 845-857.

de Vries, L. (2019). A geochemical analysis of the Kuruman Banded Iron Formation (South Africa): evidence for climatic precession and implications for the depositional environment. *Bachlor thesis project.*

Wang, Y., Xu, H., Merino, E., & Konishi, H. (2009). Generation of banded iron formations by internal dynamics and leaching of oceanic crust. *Nature Geoscience, 2*(11), 781.

Weber, H., Thamdrup, B., & Habicht, K. (2016). High sulfur isotope fractionation associated with anaerobic oxidation of methane in a low-sulfate, iron-rich environment. *Frontiers in Earth Science, 4*, 61.

Whitehouse, M., & Fedo, C. (2007). Microscale heterogeneity of Fe isotopes in> 3.71 Ga banded iron formation from the Isua Greenstone Belt, southwest Greenland. *Geology, 35*(8), 719-722.

Widdel, F., Schnell, S., Heising, S., Ehrenreich, A., Assmus, B., & Schink, B. (1993). Ferrous iron oxidation by anoxygenic phototrophic bacteria. *Nature, 362*(6423), 834.

Wu, L., Beard, B., Roden, E., & Johnson, C. (2011). Stable iron isotope fractionation between aqueous Fe (II) and hydrous ferric oxide. *Environmental science & technology, 45*(5), 1847-1852.

Wu, L., Percak-Dennett, E., Beard, B., Roden, E., & Johnson, C. (2012). Stable iron isotope fractionation between aqueous Fe (II) and model Archean ocean Fe–Si coprecipitates and implications for iron isotope variations in the ancient rock record. *Geochimica et Cosmochimica Acta, 84*, 14-28.

Zahnle, K., & Walker, J. (1986, 4). Lunar nodal tide and distance to the Moon during the Precambrian. *Nature, 320*(6063), 600-602.

Zerkle, A., Poulton, S., Newton, R., Mettam, C., Claire, M., Bekker, A., & Junium, C. (2017). Onset of the aerobic nitrogen cycle during the Great Oxidation Event. *Nature, 542*(7642), 465-467.

Zhang, C., Horita, J., Cole, D., Zhou, J., Lovley, D., & Phelps, T. (2001, 7). Temperature-dependent oxygen and carbon isotope fractionations of biogenic siderite. *Geochimica et Cosmochimica Acta, 65*(14), 2257-2271.

Zheng, H., Powell, C., Rea, D., Wang, J., & Wang, P. (2004). Late Miocene and mid-Pliocene enhancement of the East Asian monsoon as viewed from the land and sea. *Global and Planetary Change, 41*(3-4), 147-155.

Zhu, C., Lee, W.-S., Kang, H., & Park, C.-K. (2005). A proper monsoon index for seasonal and interannual variations of the East Asian monsoon. *Geophysical Research Letters, 32*(2).

Ziegler, M., Lourens, L., Tuenter, E., Hilgen, F., Reichart, G.-J., & Weber, N. (2010). Precession phasing offset between Indian summer monsoon and Arabian Sea productivity linked to changes in Atlantic overturning circulation. *Paleoceanography, 25*(3).